Electrochemical and x-rays studies on various Tin-Based-Oxides as potential negative electrodes for Li-ion batteries

University of St Andrews

School of Chemistry

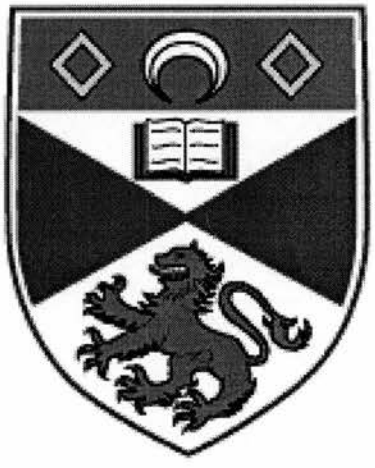

A thesis presented for the degree of
Doctor of Philosophy

by

Frédérique Belliard

DECLARATION

I, Frédérique Belliard, hereby certify that this thesis, which is approximately 40000 words length, has been written by me, that is the record of work carried out by me and that it has not been submitted in any previous applications for a higher degree.

Date 12/11/01 Signature of Candidate

I was admitted as a research student in October 1998 and as a candidate for the degree of Doctor of Philosophy in October 1999; the higher study for which this is a record was carried out in the University of St Andrews between 1998 and 2001.

Date 12/11/01 Signature of Candidate

I hereby certify that the candidate has fulfilled the conditions of the Resolution and Regulations appropriate for the degree of Doctor of Philosophy in the University of St Andrews and that the candidate is qualified to submit this thesis in application for that degree.

Date 12/11/01 Signature of Supervisor

In submitting this thesis to the University of St Andrews I understand that I am giving permission for it to be made available for use in accordance with the regulations of the University Library for the time being in force, subject to any copyright vested in the work not being affected thereby. I also understand that the title and abstract will be published, and that a copy of the work may be made and supplied to any bona fide library or research worker.

Date 12/11/01 Signature of Candidate

ACKNOWLEDGEMENTS

I would like to thank Prof. John Irvine for giving me the opportunity to do a PhD, for his supervision, guidance and support over the past 3 years. I would like to thank all the members of the JTSI group. Special thanks to "Paulo" (Dr. P.A. Connor) for helping throughout my project. Thanks should also go to the technical staff especially Colin Smith for fixing my bike and Bobby Cathcart for providing Scottish humour.

I would like to thank as well Dr. I. Harvey at the Daresbury SRS for assistance with EXAFS experiments.

Many thanks to all friends and acquaintances for making the duration of my PhD enjoyable. Thanks to my flatmate Zaharenia for making lots of Greek coffee.

Je voudrais remercier ma mère Inès et mon frère Arnaud pour leur amour et support sans limite. Je voudrais aussi les remercier pour cette phrase d'encouragement "PLISS FOSS" envoyée par email toutes les semaines. Je ne voudrais pas oublier ma grand-mère et le reste de la famille en Martinique.

Merci à toute ma famille en France, Marie-France, Yvette, Laurent, Marie-Clothilde et tous les autres. Une pensée très spéciale pour ma grande famille au Sénégal et à la génération 1970 Arona et Rama. Un grand merci à mon "Doudou" Claus pour son amour.

"Un a un seigneur je les vois et les aime ceux que vous m'avez donné comme soutien. Un a un, aussi, je les compte les membres de cette chère famille qu'ont rassemblés peu a peu autour de moi les affinités de mon coeur, de la recherche scientifique et de la pensée."

Pierre de Teilhard de Chardon

Abstract

A two step mechanism was proposed for tin oxides materials on Li insertion. In the first step Li reacts irreversibly with tin oxide to form Sn metal and amorphous matrix Li_2O. Then in the second step more Li reacts with Sn metal to form reversibly Li-Sn alloys. The interactions between the matrix Li_2O and the metal are not well understood. Thus the aim of this project was the study of the mechanism occurring upon cycling by x-rays studies and then to determine how the changes in short-range order affect the electrochemical performance.

ZnO:SnO_2 mixtures, Zn_2SnO_4, ZnO and Li_2SnO_3 were investigated as negative electrodes for Li-ion cells. EXAFS and XRD successfully followed the changes occurring in the active material during cycling. The cycling performance of each material was studied and compared to SnO_2.

The reduction of ZnO into metallic Zn occurs at 0.6 V, thereafter Li inserts reversibly Zn metal to form different Li-Zn alloys. EXAFS and XRD data confirmed the reduction of ZnO and the reversible alloying of Zn metal with Li. In addition EXAFS has revealed the re-oxidation of Zn metal during the initial charge that can be seen electrochemically. Due to this additional phenomenon, ZnO does not follow the mechanism proposed for SnO_2. ZnO cycles poorly due to the high crystallinity of Zn metal and therefore is not a promising negative electrode.

Electrochemical tests on the $ZnO:SnO_2$ mixtures showed that SnO_2 and ZnO are reduced successively into metallic Sn and Zn respectively. EXAFS and XRD confirmed this observation. Most of the Li inserts reversibly into Zn and Sn metal after the reduction of ZnO. Sn EXAFS showed that the reduction of SnO_2 in the mixture leads to amorphous Sn metal. The $ZnO:SnO_2$ mixture cycles very badly whatever is the ratio. ZnO content controls the electrochemical performance of each $ZnO:SnO_2$ mixture. The poor cycling performance is due to the high degree of crystallinity of Zn and Sn metals.

Zn_2SnO_4 is electrochemically reduced by Li at an unexpected potential, 0.5 V that is lower than the reduction potential of SnO_2 and close to the ZnO potential. In Zn_2SnO_4, Zn^{2+} and Sn^{4+} are reduced simultaneously while in the $ZnO:SnO_2$ (2:1) mixture each cation is reduced separately. The reduction of Zn_2SnO_4 was verified by EXAFS and XRD. After the reduction of Zn_2SnO_4 various Li-Zn and Li-Sn alloys are reversibly formed. Zn_2SnO_4 exhibits very good cycling compared to the $ZnO:SnO_2$ (2:1) mixture. No crystalline Sn or Zn metals were observed when Zn_2SnO_4 was cycled within the optimal window voltage (0.2-0.8 V).

The reduction of Li_2SnO_3 into Sn metal is observed at 0.18 V, reduction potential that is very close to Li. Then Li is inserted reversibly into Sn metal to form Li-Sn alloys. The reduction and the reversible alloying of Sn metal with Li occur at the same potential. Li_2SnO_3 forms one extra of Li_2O compared to SnO_2 that is believed to compensate the volume changes occurring during the reversible alloy formation. XRD proved that SnO_2 is reduced into more crystalline Sn than is found for Li_2SnO_3. However the cyclability of Li_2SnO_3 is still lower than SnO_2 even though they have the same theoretical capacity.

None of the materials investigated follow exactly the mechanism suggested for tin oxide materials. EXAFS and XRD measurements have proved that the cycling performance of each metal oxide is intimately related to the crystallinity of the metal obtained after reduction. The crystallinity of the metal depends on the cycling voltage range and on the starting material. The improvement of the cycling performance is not automatic with small particle size.

Zn_2SnO_4 displays the best cycling performance and is therefore very promising negative electrodes for Li-ion battery although ZnO cycles poorly. At the 25^{th} cycle ZnO has lost more than 80 % of its initial reversible capacity whereas Zn_2SnO_4 has more than 85 % of its initial reversible capacity left.

1 Introduction

1.1 General batteries

1.1.1 Introduction

Batteries are widely employed in the modern world in a huge number of appliances. The use of small batteries has expanded very quickly for applications such as watches, heart pacemakers, and compact disc players. As the number of electronic devices grows, in response to consumer demand battery research tries to keep up with these developments. These new devices are portable electronics (laptops, notebook computers, and cameras…).

A battery is a device where electricity generated by electrochemical reactions is stored as chemical energy. The discharge process is a spontaneous electrochemical reaction that leads to the release of energy. The charge process occurs when an inverse current is applied and the chemical energy is stored at the electrode.

Two categories of batteries (often called cells) can be distinguished: primary batteries and secondary batteries. Primary batteries are used once in a single discharge and disposed of when all the reactants have been consumed. On the other hand secondary batteries might be recharged several times and used again. During the charging process

the spontaneous electrochemical reaction occurring during discharge is reversed. This is possible by passing a current through the cell in the opposite direction to the discharge process.

The 19th century was very productive and decisive regarding battery development. Alessandro Volta (Italy) described the first battery in 1800 by stacking alternatively layers of zinc, paper soaked in salt water and silver. The next significant step in battery expansion was the Daniell cell (London, 1836) consisting of copper plates, zinc plates, copper sulphates and zinc sulphates. This cell was used commercially by telegraphic systems. Leclanché (France, 1866) invented a primary battery which is still the base of all aqueous electrolyte primary cells. Since, aqueous electrolyte cells have been considerably improved. Despite these advances primary lithium battery applications might expand for three reasons. The precursors used in aqueous batteries are poisonous, the recycling process is a difficult task and moreover primary lithium batteries display twice as much capacity.

Nowadays most current research is focused on secondary batteries because they present many novel and attractive applications. Three kinds of secondary batteries can be distinguished, lead-acid, alkaline and rechargeable Li-ion battery systems. The lead-acid system is thermodynamically unstable so the direct consequence is the self-discharge during storage. Secondary alkaline cells include nickel-cadmium and nickel-metal hydride batteries; they show better capacity and energy density than lead-acid cells. Nevertheless, nickel-cadmium cells exhibit one drawback, the toxicity of cadmium. In

contrast, Li-ion batteries are environmentally friendly although more expensive. In addition to the fact of being non-poisonous, Li-ion batteries[1-2] display the highest capacity and energy density in secondary batteries (Figure 1.1).

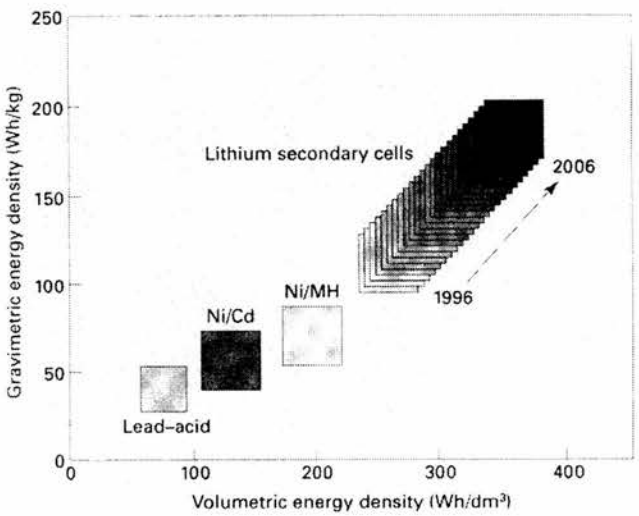

Figure 1.1 Comparison of gravimetric and volumetric energy density of lithium secondary cells with aqueous electrolyte-based systems (taken from reference 1)

1.1.2 **Battery terminology**

The capacity is the current supplied by the battery during a pre-determined time and is usually expressed in ampere-hours. The C-rate corresponds to the time needed to discharge or charge a battery. Current density expressed in mA/cm^2 defines the flowing current provided per unit electrode area. The cycle life or cyclability is the number of cycles totalled until the battery fails to meet selected performance criteria. The energy density is the energy stored in a cell and is expressed in Wh/dm^3 or Wh/kg.

1.2 Aqueous batteries

1.2.1 Primary aqueous electrolyte batteries

Aqueous electrolyte batteries are probably the commonest batteries produced and best known in the world. These batteries find a widespread usage due to a combination of factors including the low cost and the ease of manufacture. All these aqueous electrolyte batteries are based on the classical Leclanché cell that was invented in 1866.

A Leclanché cell is a carbon-zinc battery with zinc chloride and ammonium chloride dissolved in water as electrolyte. This battery can be described as followed:

$$Zn(s)|ZnCl_2(aq),NH_4Cl(aq)|MnO_2(s),C(s)$$

Anode *Electrolyte* *Cathode*

The cathode is composed of carbon and refined manganese oxide; nowadays acetylene black is preferred to the graphite originally employed by Leclanché. The carbon provides a good electronic conductivity of the cathode. Zinc metal is the anode material and the electrolyte is an aqueous solution of zinc chloride saturated with ammonium chloride. The temperature range of operation (10 - 40 °C) and the short self-life (up to 2 years) limit the use of Lcclanché batteries. Nevertheless the main problem with these batteries is the electrolyte leakage that occurs after heavy discharge.

In the zinc-chloride cells, which are one variant of the Leclanché batteries, the ammonium chloride is replaced by zinc chloride. This resolves the cell leakage problem

that follows heavy discharge. They exhibit slightly better performance and work better at lower temperatures compared to the classic Leclanché cell.

Another variant of the Leclanché battery is the alkaline manganese battery. In this case the electrolyte is a concentrated aqueous solution of potassium hydroxide. Alkaline manganese batteries outperform the classic Leclanché cell and zinc-chloride batteries due to the high conductivity of the electrolyte. Zinc powder or granules are preferred over zinc metal. Alkaline cells are more resistant to leakage and have longer shelf-life (up to 4 years).

There are some other primary aqueous batteries that can be found on the market such as zinc-mercuric oxide, cadmium-mercuric oxide and zinc-silver oxide. These various systems exhibit high volumetric capacity and good discharge characteristics under heavy loads. Nevertheless primary lithium batteries may displace these batteries because they are composed of poisonous components.

1.2.2 **Secondary aqueous batteries**

1.2.2.a **Lead-acid batteries**

Lead-acid batteries offer several advantages such as low cost, excellent reversibility and easy manufacture. Porous lead is used as negative electrode, lead oxide as positive electrode and sulphuric acid as electrolyte. The electrochemical process occurring inside the battery can be described as followed:

$$Pb\ (s) + PbO_2\ (s) + 2H_2SO_4\ (S) \underset{\text{charge}}{\overset{\text{discharge}}{\rightleftharpoons}} 2PbSO_4\ (S) + 2H_2O\ (l)$$

The electrolyte H_2SO_4 is consumed during discharge and is regenerated on charge thus its density varies. This variation of density upon cycling is really useful to determine the actual stage of the battery.

The porosity of PbO_2 is an important factor in order to accommodate the increase of volume during the passage of PbO_2 to $PbSO_4$, and optimum current densities can be achieved, as the contact area between the solid and the electrolyte is larger. During the discharge of the battery, insoluble $PbSO_4$ is formed which exhibits poor electrical conductivity and furthermore $PbSO_4$ is deposited on both electrodes. Therefore, the capacity decreases because of the electrode passivation and only 5-10 % of the theoretical capacity is reached for large current densities. The formation of insoluble $PbSO_4$ leads to the increase of the internal resistance of the battery and reduces the conductivity of the electrolyte because H_2SO_4 has been consumed.

Formation of hydrogen and oxygen occur in lead-acid cell, which might cause the self-discharge of the battery. The reactions involving oxygen and hydrogen are dependent of temperature, electrolyte concentration and impurity content. In order to compensate the self-discharge, the battery should be stored in the charge state. A lead-acid cell that has not been charged for a long time or has been used at too high temperatures provokes the formation of large crystals of $PbSO_4$. This phenomenon is known as sulphation and causes severe passivation.

Standard lead-acid batteries might also lose water due to the electrolysis reaction leading to oxygen and hydrogen formation. The presence of impurities such as Sb, As, Co, Mn, Ni, Pt, Te, even at low content affects the loss of water by decreasing the voltage where the electrolysis occurs.

1.2.2.b **Alkaline batteries**

Alkaline cells are more expensive than lead-acid batteries, so consequently occupy a smaller part on the market of secondary batteries. Nevertheless, they outperform lead-acid batteries in several domains such as low temperature performance, cycle life, stability and reliability. Based on their high performances for numerous applications they progressively become attractive.

Invented at the end of the 19th century by Jungner (Sweden) and Edison (USA), alkaline batteries were based on nickel (III) oxide as cathode, potassium hydroxide as electrolyte and cadmium (or iron) as anode. The overall electrochemical reaction occurring in the cell is described as follows:

$$M + 2NiOOH + 2H_2O \underset{\text{charge}}{\overset{\text{discharge}}{\rightleftharpoons}} M(OH)_2 + 2Ni(OH)_2$$

M = Cd, Fe, Zn

Cadmium nickel hydroxide cells commonly called nickel-cadmium cells are really successful amongst the alkaline batteries. The success of nickel-cadmium batteries is based on their long cycle life, excellent reliability, low temperature performance and low maintenance. However, these batteries are more expensive and furthermore environmental concerns are growing because of the toxicity of cadmium.

In comparison to lead-acid batteries, nickel-iron cells display inferior low temperature performance, higher corrosion and self-discharge, and need frequent maintenance. The nickel-zinc battery exhibits slightly better performance than nickel-iron, nickel-cadmium and lead-acid batteries and moreover zinc is cheaper and less toxic than cadmium.

As recycling nickel-cadmium cells is not an easy task, new rechargeable alkaline batteries such as nickel-metal hydride and alkaline manganese cells have appeared.

Generally alkaline manganese batteries are considered as primary cells. But it has been possible to recharge safely these cells by avoiding the formation of internal gas pressure by adding catalysts to facilitate the recombination of hydrogen gas. New separators were also developed to prevent short-circuit due to zinc dendrite formation, and the cut-off was reduced to form only manganese (III) on discharge. These cells are cheaper than nickel-cadmium and moreover exhibit low self-discharge rates.

The last advanced rechargeable alkaline battery is the nickel-metal-hydride battery. Similar to nickel-cadmium batteries nickel oxide and potassium hydroxide remain respectively the cathode and the electrolyte. The hydrogen stored under a metal hydride is the anode. The whole reaction can be described as follows:

$$MH_x + 2NiOOH \underset{\text{charge}}{\overset{\text{discharge}}{\rightleftharpoons}} MH_{(x-1)} + Ni(OH)_2$$

The metal hydride is a complex alloy of partially substituted nickel and either rare earth elements or other metal (Zr, Ti). Nickel-metal-hydride cells exhibit higher capacity than nickel-cadmium cells, however they have higher self-discharge rate and lower performance at elevated temperatures. This new generation of alkaline batteries is quite expensive but remains an excellent challenger to lithium-ion batteries.

1.3 Lithium batteries

1.3.1 Primary lithium batteries

Lithium metal is the lightest metal (6.94 g/mol) and its electrochemical potential of reduction is –3.045 V. Therefore, the possibility of having a 3 V battery by using lithium metal as anode is offered when the cathode is well chosen. These two properties plus the high theoretical specific capacity (3860 mAh/g) of lithium make this metal a promising anode material. In the oxidation process of lithium, only one electron is involved while two electrons are involved in the oxidation of zinc or cadmium. Therefore, in volumetric terms (Wh/dm^3) lithium cells are not better than aqueous cells, however primary lithium batteries exhibit about twice the specific energy of aqueous systems (Figure 1.1).

As lithium is highly reactive with water, non-aqueous electrolytes are required in the battery. Lithium seems to be stable in a wide range of non-aqueous electrolytes, due to the passivation phenomenon, which is the formation of a surface layer on top of the metal. The passive layer prevents further corrosion of the surface. In the meantime the passivation allows the discharge of the battery and minimises its self-discharge. Primary lithium battery systems can be used within a very large range of temperature between – 40 °C and 60 °C.

Primary lithium batteries can be divided into three categories depending on the cathode material: solid cathode reagents (MnO_2, $(CF_x)_n$...) where the cathode is essentially insoluble in the electrolyte, soluble cathode reagent (SO_2...) and liquid cathode reagent ($SOCl_2$...) where the active material is formed in the liquid at operating temperature.

The electrolyte is an important factor to consider in the battery. The electrolyte requires good ionic conductivity, which increases with concentration. Further requirements are chemical and electrochemical stability. Inorganic salts dissolved in aprotic organic solvents were tested as the most convenient electrolytes. However organic solvents are not stable in the presence of Li metal but display different degrees of kinetic stability[3]. This is due to the Solid Electrolyte Interphase (SEI) formation[4], which prevents further corrosion of the Li metal and conducts Li ions. Electrolytes were studied extensively to attempt to solve Li metal instability towards organic solvents, but despite the solutions proposed[5] cells with Li metal still exhibit limited cycle life and furthermore safety is still an important concern.

Ethers, acrylic and cyclic esters such as ethylene carbonate (EC), propylene carbonate (PC) were found to be the most convenient solvents. Mixed solvents are sometimes preferred to optimise the performance of the electrolyte. For example, EC-DMC was chosen to stabilise the layer formed from the passivation phenomenon on Li metal. Mixed solvents can also be used as well as a modifier of the surface layer of lithium metal. Solvent selection depends on the voltage range of stability and on the voltage required for the charging process.

A high solubility of the salt is needed to obtain an efficient conductivity. Thus polar solvents are used to ease the dissolution of lithium salts. $LiPF_6$, $LiBF_4$, $LiClO_4$, and $LiCF_3SO_3$ are the most frequently salts used in lithium batteries. Melting and boiling points, density and viscosity of the electrolyte should be examined, as these properties might limit the operating temperature range of the battery. Moreover chemical compatibility with the cathode material is as well a significant property to take into account in lithium battery systems. Side reactions often occurring between the electrolyte and the electrode should be considered. High purity, low water content and potential range determine the solvent stability in lithium batteries in the presence of lithium metal.

1.3.2 **Rechargeable Li-ion batteries**

1.3.2.a **Definition**

The principal characteristic of the Li-ion battery is that no metallic lithium is present at any stage of the cell. Lithium-ion cells work by transporting Li ions between the negative electrode and the positive electrode. During charging, lithium ions are extracted from the cathode and inserted into the anode host whereas during discharging lithium ions are intercalated into the cathode[1] (Figure 1.2*)*.

The first commercial Li-ion cell was introduced by Sony (Japan) in 1991; carbon and $LiCoO_2$ were the negative electrode and positive electrode respectively. Since then

many manufacturers have grown and many developments have been made. Carbon (graphite and coke) is still almost the only anode used commercially, however other materials such as alloys and metal oxides are currently under investigations to improve the cycle life and capacity of the battery. Tin-based-oxide compounds remain promising negative electrodes now due to their high initial capacity. In the case of the positive electrode material apart from $LiCoO_2$[6] two novel large families have emerged, $LiNiO_2$ and $LiMn_2O_4$[5-7]

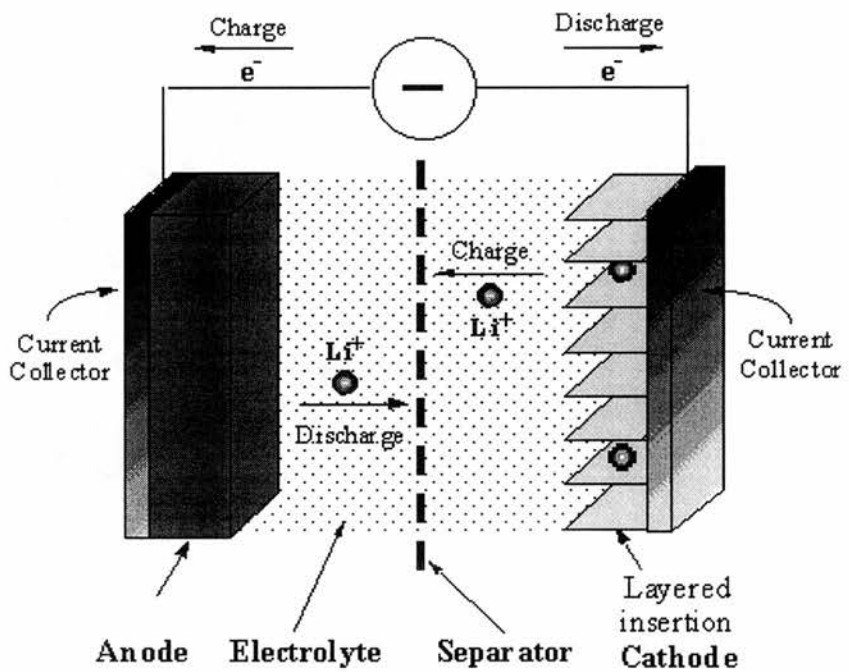

Figure 1.2: Schematic illustration of the discharge and charge processes in rechargeable lithium-ion battery

Li-ion cells are very attractive because of the combination of several factors. Their energy density is twice higher than that of nickel based batteries (Figure 1.1), which is

very useful for applications that need a lot of power such as portable systems (cellular phones, laptops…). These batteries have a high average operating voltage (~3.6V), long cycle life (over 500 cycles), low self discharge rate and moreover Li-ion cells are relatively safe and non-poisonous[6-8-9].

1.3.2.b **The negative electrode**

1.3.2.b.1 Lithium metal

Although not strictly Li-ion, Li metal is described as negative electrode. Lithium is the lightest of all metals, has the greatest electrochemical potential and provides the largest energy. Rechargeable batteries using lithium metal as an anode are capable of providing both high voltage and excellent capacity, resulting in an incredible energy density[10]. Unfortunately, the development of rechargeable batteries employing Li as a negative electrode can cause safety problems. Li is so electronegative that it is thermodynamically unstable towards a large number of reducible materials. Li reacts with most electrolytes and consequently passivation occurs on the surface. A successful discharge is possible if the passivating layer has a sufficient conductivity to act as a SEI[4] layer. The passivation phenomenon ensures primary Li cells a long shelf-life but it provokes severe damages in a secondary cell.

On charging the deposited Li tends to form dendrites. Evidence on the morphology of the dendrites were given by *in-situ* SEM[11-12-13-14] and a schematic representation of the phenomenon occurring during cycling is shown in Figure 1.3. Problems arise on the

following discharge when the fresh plated lithium becomes isolated so the discharge efficiency decreases[15]. As a result upon cycling a significant amount of the Li electrode is corroded. Thus excess of Li in the battery is necessary to compensate this loss. Furthermore dendrites can grow through the separator and cause short-circuits that can occasionally lead to a thermal runaway[16]. The reason is that dendrites are extremely reactive because of the low melting point of Li (180 °C). This means that a shorted dendrite can melt, and molten lithium is violently reactive and is no longer protected by a passivating layer[17]. Overall Li corrosion and dendrite formation create several problems leading to poor cycling efficiency of the battery.

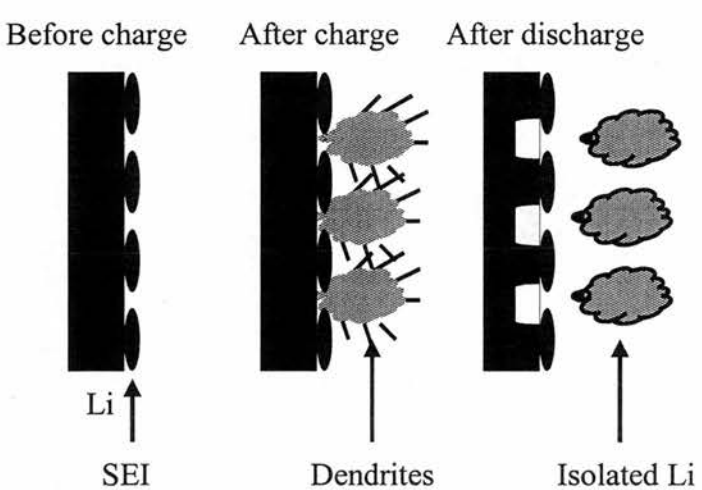

Figure 1.3: Schema of dendrite formation

Despite the hazards associated with Li, it is still considered as a potential negative electrode since it was found that the dendrite formation depends principally on the nature of the electrolyte. Intensive research on electrolytes was carried out in order to control dendrite formation. Employing polymer electrolytes and more inert solvents

were suggested and ether mixtures appear to be one of the most favourable solvents for secondary Li batteries[18]. The use of 2-MeTHF/$LiAsF_6$ based solutions seems to be very promising, as Li cycling efficiency increases and its morphology becomes smoother[19]. The use of organic additives in polymer electrolyte also improved the Li electrode performance[20]. Despite the diverse approaches that show some improvement in the cycle life of a secondary battery using Li as anode, safety remains an important issue. Therefore the new challenge was to replace Li metal and many materials such as Li alloys, Tin-based compounds and carbon were investigated.

1.3.2.b.2 Alloys

Li alloys were naturally one of the first solution suggested to replace metallic lithium in secondary batteries. The possible electrochemical formation of Li alloys in liquid organic electrolytes containing Li salts was demonstrated by Dey[21] in 1971. Lithium is able to alloy with most metals (Mg, Ca, Al, Si, Ge, Sn, Pb, As, Sb, Bi, Zn and Pt...) at room temperature except hard metals (Cu, Ti, Ni, Mo, Nb). Early works on Li alloys were however focused on high temperature cells around 400 °C that operate in molten electrolytes. The replacement of Li by various Li alloys, such as Li-Al[22-23-24], Li-Sn[25-26] alloys in these batteries was crucial because Li metal melts at 180 °C. The mechanism occurring during the alloy formation can be described as below:

$$Li_xM \underset{\text{charge}}{\overset{\text{discharge}}{\rightleftharpoons}} xLi^+ + xe^- + M$$

The alloying of metal is a reversible process and according to the equation above no capacity loss should be observed, which makes Li alloys very promising negative electrodes for secondary batteries.

The thermodynamic potential for formation of the Li alloys is approximately between 0.2 and 1 V, and consequently the operating potential of the battery is lower compared to a battery using Li metal. Low potential means that the specific charge of the different Li-alloys is less than the specific charge of Li metal[27-28], however, their charge densities are relatively close to Li metal[29]. Experimentally[6] the cycling efficiency of Li is less than 99 %. Thus in order to have a reasonable cycle life excess of Li has to be employed to compensate the corroded and isolated Li that appear during cycling. As a result, the charge densities and the specific charges of the diverse Li alloys become closer to that of metallic Li and should exhibit similar or even better electrochemical performance. Nevertheless Li alloys with insertion potentials close to metallic Li potential could cause similar safety problems as Li metal especially during deep discharge.

Despite all these advantages, none of the Li alloys are used in commercial Li-ion batteries due to dimensional problems occurring during the reversible insertion of metallic Li into a metal. Metals face structure and volume changes[29-30] while alloying

with Li metal (Figure 1.4). Volume changes cause mechanical stresses, as a result the electrode suffers from crumbling and cracking, which lead to its degradation due to the loss of the electronic contact between the particle sizes. Finally after a few cycles it has lost most of its initial reversible capacity[29-28-31]. Structure and morphology (grain, size, shape, texture and orientation) of Li-alloys affect the electrode stability, therefore several suggestions were made to minimise the dimensional problems linked to Li alloys.

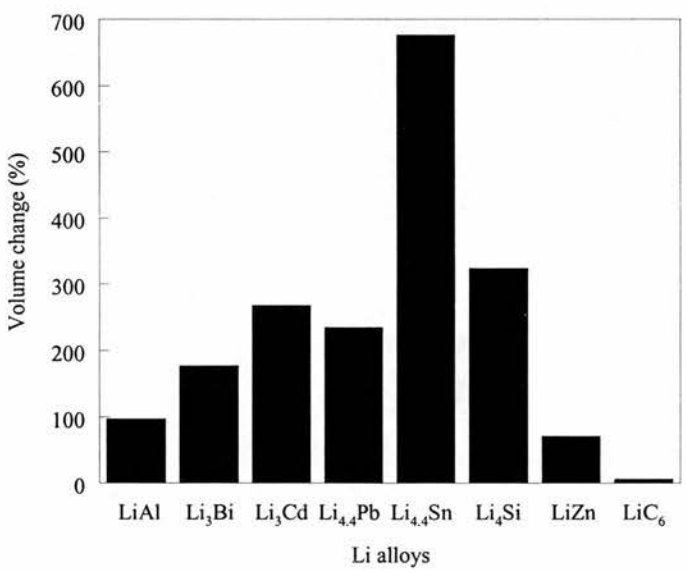

Figure 1.4: Volume changes during alloying of Li with various metals [taken from reference 27]

Investigations mainly on Li-Sn alloys show that metal with large particle size is less resistant to the volume changes occurring during cycling. Based on the studies on TiO_2 (anastase) showing that Li intercalation is improved with small particle size[32], one of the solutions proposed was to use a thin layer having small particle size to minimise the absolute change in the particle size upon cycling. Successfully small particles improve

significantly the cycling performance of the battery because the particles accommodate better the volume expansion[33-29-33-34], thus the whole volume changes can be reduced by two.

The surface area of metal increases with reduction of particle size. Therefore the amount of Li irreversibly consumed for SEI formation should also increase, likewise diminishing the amount of Li available for cycling. Although small particle size alloys outperform large size alloys, their cycling behaviour is still not good enough to be used commercially.

Thus it was thought that the association of an active or inactive matrix and small particle within the electrode would contain the volume expansion but the matrix should ensure the ionic and electronic conductivity through the electrode[35]. Many tin-based phases[36-37-33-28-38-39-40] such as Sn_2Fe:$SnFe_3C$[41], Ni-Sn based alloys[42-43], $Li_xCu_6Sn_5$[44] and Sn/SnSb[29-28] were investigated and all studies confirm the benefit gains from the presence of the matrix, which minimises the volume expansion occurring upon cycling. Although these tin-based alloys show good cyclability, their performance is still not satisfactory. Recently work[45] on nano Sn and $AlSi_{0.1}$ suggest that the matrix should have a low coefficient of elasticity to reduce the stress induced by the volume expansion occurring during the reversible insertion of Li. Furthermore the matrix should exhibit a high elastic deformation to compensate the volume changes of the metal.

1.3.2.b.3 Carbonaceous materials

As described earlier in this section, Li metal causes safety problems such as dendrite formation upon cycling so carbon was chosen as another alternative negative electrode for Li-ion batteries. It was shown that carbon is thermally more stable than Li metal as a negative electrode upon cycling[16]. Various carbonaceous materials can intercalate Li into their layered structure, which make them very attractive for battery applications. However, a range of graphitic materials remains the almost only negative electrode available commercially for Li-ion batteries due to its high reversible capacity and low intercalation potentials below 1 V.

Carbon presents naturally two crystalline forms, cubic diamond and graphite structures. The graphite structure is the one of electrochemical interest (Figure 1.5). The well known layer structure of graphite is hexagonal where carbon layers are stacked with an ABAB type sequence. The rare graphite structure is rhombohedral where the sequence is type ABCABC. Both phases coexist and are interchangeable but the hexagonal form is thermodynamically stable[46]. Two-dimensional graphite with strong carbon-carbon bonds inside the graphenes (plane of the hexagons formed by carbon) and weak Van der Waals bonds between the planes allows insertion between the layers. Neutral (Br_2), cationic (alkaline metal) and anionic (ClO_4^-) species can be inserted into the graphene layers[47].

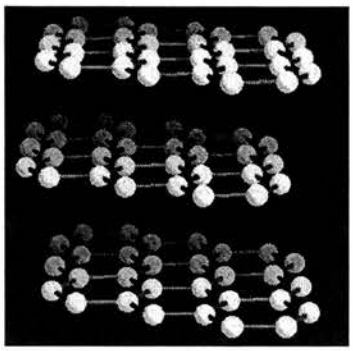

Figure 1.5 Graphite structure

Figure 1.6 shows the schematic representation of the insertion stages of graphite. A stage represents the number of graphene planes periodically dividing into two following inserted layers[47]. During the intercalation process, the graphite layers shift in order to be aligned; consequently, the stacking sequence changes from ABAB to AIAI, where I is the intercalated species[48]. Electrochemical insertion leads to a mixed conductor material because graphite keeps its electronic conductivity; and the ions inserted are still mobile within the graphene plans. The reversible intercalation of Li into graphite occurs between 0.2 and 0.05 V. Theoretically Li is intercalated reversibly into carbon graphite to form Li_xC_6 ($0<x<6$). The theoretical specific capacity of Li_xC_6 is 372 mAh/g.

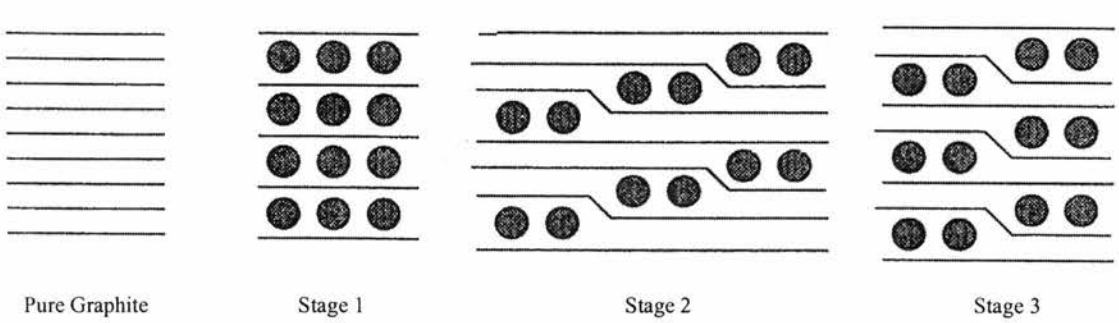

Figure 1.6: Schematic representation of the intercalation process into graphite (taken from reference 47)

In practice the reversible intercalation of Li into carbon depends on several parameters such as degree of graphitization, type of carbon and electrolyte composition[49-50]. When the electrochemical insertion process occurs in a liquid electrolyte, generally Li inserts irreversibly with the solvent molecules and that increases the distance between the graphene planes. As a result, Li intercalation leads to poor reversibility. It has been possible to reduce Li intercalation into the solvent by using cyclic carbonate such as propylene carbonate alone or mixed with ethylene carbonate. Under these conditions a compact film is formed on top of the carbon surface which is Li-ion conductor and electronic insulator (SEI). The SEI formation prevents the co-intercalation of solvent molecule with Li ion within the graphite structure[51]. The reduction of Li insertion with solvent molecules was also achieved by replacing natural graphite by other types of carbon such as synthetic graphite, fibres and petroleum coke.

1.3.2.b.4 Tin metal

Tin metal has two allotropes, white or beta tin which is stable for temperatures above 13.2 °C and the grey or alpha tin which is stable below this temperature. Until now only beta-tin has been tested as negative electrode. Tin metal has all the characteristics to be a good negative electrode regarding the available capacity (Table 1.1). Courtney and Dahn have proposed a mechanism to explain the reaction that occurs during charge and discharge processes[53].

Equation 1.1: $4.4Li + Sn \rightarrow Li_{4.4}Sn$ discharge

Equation 1.2: $Li_{4.4}Sn \leftrightarrow 4.4Li + Sn$ charge

	1st irreversible capacity (mAh/g)		1st reversible capacity (mAh/g)	
	theory	experimental	theory	experimental
Beta-Sn	992	800	992	600

Table 1.1: Theoretical and experimental initial capacities of beta-Sn

Theoretically, cycling beta-tin should not show an irreversible loss during the initial discharge, nevertheless experimentally this loss is about 25 %. At the second discharge, the tin has again lost 25% of the first capacity then, beta-tin cycles very badly[29] essentially due to volume expansion. According to dilatometric expansion studies[28], the major increase in volume occurs during the initial discharge. The volume can rise to 300% during the first alloying, and then the following alloying and de-alloying processes induce smaller volume changes. However this first large volume change is the precursor of the bad cycling of the beta-tin. Mechanical stresses occur during further cycling and the consequence is the loss of electronic contact between particles and cracking of the electrode. Therefore it becomes very difficult to extract the lithium from the bulk tin, so the battery performance decreases after only few cycles.

As the volume expansion appearing in the initial discharge is the dominant problem for the beta-tin cyclability, the use of small particle size appears to be the solution. Reducing the size of tin particle limits the volume expansion[29] down to 100% for the first discharge compared to 300% observed for coarse tin. While cycling, changes in volume are still small and then extracting the lithium from the alloys does not modify significantly the particles size. Cracks in the electrode, stresses and electronic contact loss are retarded and minimised, so tin can reach up to 25 cycles. Despite the improvement of the cyclability of beta-tin by using small size, this cyclability is too low

to satisfy the battery market. Thus the alternative was the introduction of a conductive matrix to restrain the volume changes in order to improve the cycle life of the electrode. Recently it was found that Cu_6Sn_5 is a promising negative electrode as the cycling performance of Cu_6Sn_5 is superior to that of β-Sn[44]. The good performance of Cu_6Sn_5 is attributed to its reversibly reaction with Li. Work on the Sn-Fe system has shown as well cycle life improvement when the ration Fe:Sn increases[37].

1.3.2.b.5 Tin Based Oxide compounds

ß-Sn is a very attractive material to be used as negative electrode due to its high 1st reversible capacity observed, 600 mAh/g. Unfortunately the alloying/de-alloying of ß-Sn with Li causes some volume changes, which leads to the cracking, crumbling of the electrode. Therefore it was suggested that the introduction of a conductive matrix to restrain the volume expansion occurring during the reversible formation of Li-Sn alloys. The morphological change of Li-Sn alloys was successfully stabilised using intermetallic Li insertion compounds e.g. Sn_3Fe_5[37] or a mixed active material composite e.g. $SnSb_{0.14}$[52]. Another alternative is the use of Tin based composite oxides (TCO) as negative electrode[53]. TCO materials are reduced into Sn metal and for Li_2O, then the Li-Sn alloys are formed *in-situ*. If the formation of Li_2O is irreversible, the electrode will behave as a binary Li-Sn alloys after the 1st cycle[54].

Idota *et al.* [55] reported a reversible capacity over 600 mAh/g for amorphous Sn based oxides. Since it was hoped to replace the commercial graphite by these Sn based oxide compounds, as the observed reversible capacity is higher than graphite (372 mAh/g) and

similar to that of ß-Sn. Following this announcement research on Sn based oxides considerably increased[53-56]. From *in-situ* XRD performed on Sn, SnO, SnO_2, $SiSnO_3$ and Li_2SnO_3, Courtney and Dahn suggested a mechanism to explain the processes occurring upon cycling[53]. Initially Li reduces Tin-based Oxides to form small clusters of tin metal dispersed in a Li_2O framework. Further Li atoms are then inserted reversibly into metallic tin to form Li-Sn alloys. Thus a general equation describing the mechanism can be written as follows:

Equation 1.3 $SnO_x + 2xLi^+ + xe^- \rightarrow xLi_2O + Sn$

Equation 1.4 $4.4Li^+ + 4.4e^- + Sn \leftrightarrow Li_{4.4}Sn$

An electrochemical titration of Li into SnO and SnO_2 confirmed their decomposition[53-57-58] into Li_2O and Sn metal. The irreversible loss during the first cycle is associated with the formation of amorphous Li_2O. The alloying (charge) / de-alloying (discharge) of tin supplies the reversible capacity of the material. The reversible capacity is based on the maximum Li-Sn alloy, $Li_{4.4}Sn$. During the first cycle the battery loses approximately 50% of lithium in the irreversible process. Figure 1.7 shows the mechanism of Li insertion occurring during discharge and charge. After the reduction of tin oxide into Sn metal, the matrix Li_2O surrounds the Sn metal. The formation of Li_2O seems to prevent the deterioration of the binary Li-Sn alloys on cycling. However, the reasons for this stabilisation are not well understood.

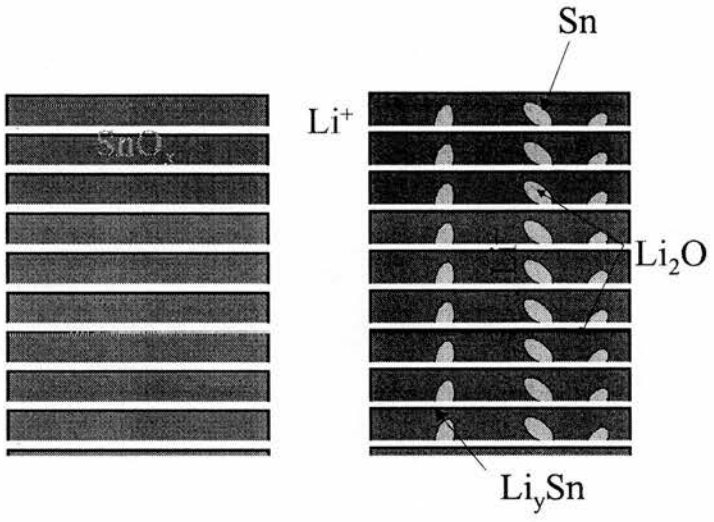

Figure 1.7: Schematic representation of the mechanism of Li insertion

SnO and SnO_2 are very promising negative electrodes for Li-ion cells as they exhibit an experimental 1st reversible capacity over 600 mAh/g as shown in Table 1.2 and therefore were extensively studied[53-59-60-61]. Under optimised conditions both tin oxides display satisfactory cycling performance[62-63-64-65]. SnO_2 is however more studied than SnO but SnO material remains a very useful model in order to understand composite tin oxide glasses mechanism[66]. According to EXAFS[67], ^{7}Li NMR[68] Mössbauer and XRD[69] studies the SnO reduction mechanism is very complex involving mixed valence intermediate compounds. After the reduction of SnO, an altered SnO environment is generated. Thereafter SnO disappears, and Li-Sn alloys and Li_2O are observed at depth discharge, but SnO is reformed on charge.

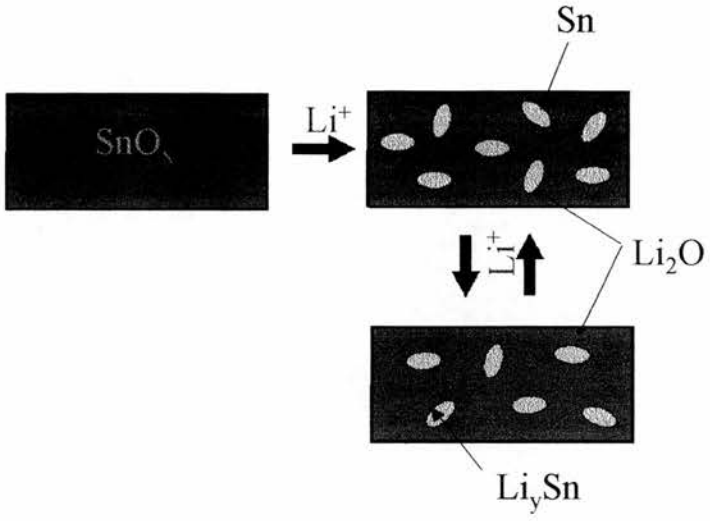

Figure 1.7: Schematic representation of the mechanism of Li insertion

SnO and SnO_2 are very promising negative electrodes for Li-ion cells as they exhibit an experimental 1st reversible capacity over 600 mAh/g as shown in Table 1.2 and therefore were extensively studied[53-59-60-61]. Under optimised conditions both tin oxides display satisfactory cycling performance[62-63-64-65]. SnO_2 is however more studied than SnO but SnO material remains a very useful model in order to understand composite tin oxide glasses mechanism[66]. According to EXAFS[67], ^{7}Li NMR[68] Mössbauer and XRD[69] studies the SnO reduction mechanism is very complex involving mixed valence intermediate compounds. After the reduction of SnO, an altered SnO environment is generated. Thereafter SnO disappears, and Li-Sn alloys and Li_2O are observed at depth discharge, but SnO is reformed on charge.

	1st irreversible capacity (mAh/g)		1st reversible capacity (mAh/g)	
	theory	experimental	theory	experimental
SnO	1270	1200	873	825
SnO_2	1491	1450	781	650

Table 1.2: Theoretical and experimental capacities (taken from reference 53)

There have been several attempts to improve SnO_2 electrochemical performance such as mixing SnO_2 with carbon[70], doping SnO_2 with molybdenum[71], with boron and indium[72] or antimony[73]. The approach was to prevent Sn metal from becoming electrically disconnected upon cycling. The cycling performance was improved with carbon and small amount of Mo (~ 2%). However SnO_2 doped with low content of B exhibit similar electrochemical performance to that of pure SnO_2, and In lowers the electrochemical performance.

1.3.2.b.6 Other negative electrodes

Early work on Li-ion cells demonstrated that MoO_2, WO_2, TiS_2 or TiO_2 could be used as negative electrodes. Unfortunately they exhibit low theoretical reversible capacity and low cell voltages[27-5-74-32]. Apart from tin based oxides various materials were investigated as potential negative electrodes for Li-ion cells. Different metal oxides such as ZnO[64-75-76], Sb_2O_3[64] or PbO[64] were successfully tested as negative electrodes and seem to follow similar mechanism proposed for Tin based oxides[53]. $Li_{1+x}Fe_{1-3x}Ti_{1+2x}O_4$ ($0 \leq x \leq 0.33$) suggested as potential negative electrodes exhibit a reversible capacity over 150mAh/g after 20 cycles although the mechanisms of intercalation are unclear[77]. A

family of vanadium oxides[78], Li_xMVO_4 (M = Cd, Co, Ni, Zn, $1<x\leq 8$) proposed as negative electrodes exhibit an initial reversible capacity over 600 mAh/g and good cyclability. Recently it was found that $Li_{3-x}M_xN$ (M = Co, Ni, Cu) can be used as negative electrodes[79]. $Li_{2.6}Co_{0.6}N$[80] tested against Li displays the highest reversible capacity (760 mAh/g) and the best cycling performance in the $Li_{3-x}Co_xN$ ($0.2<x<0.6$) system. However a Li-ion cell $Li_{1.6}Co_{0.4}N/LiNiO_2$ has showed good cyclability of more than 240 cycles. Recently studies on Cu_xO[81-82], Co_3O_4[81], FeO[81] and NiO[81] reveal that these oxides do not follow the suggested model for tin based oxides. During charge a partial decomposition of Li_2O formed during the initial discharge occurs and then the metal is re-oxidised.

1.3.2.c **The positive electrode**

The first row transition metal oxides appear to be very attractive as positive electrodes for Li-ion batteries due to their low molecular weight and their favourable electrochemical and solid sate properties[6]. The specific capacity of these materials is based on the reversible range Δx of Li content during charge/discharge process.

$$\Delta x\ Li^+ \mid \Delta x\ e^- + Li_xMX - Li_{x+\Delta x}MX\ (X = O, S \text{ or } Se)$$

Several transitions metal chalcogenides such as TiS_3, $NbSe_3$, NbS_2 or TiS_2 were investigated as potential positive electrodes. TiS_2 material[83] has layer structure, which is stable under Li intercalation and has a good electronic conductivity. TiS_2 exhibits a very

good cyclability, over 400 cycles with only 20% loss[5]. MoO_3, WO_3 were proposed as well as positive electrodes. A large number of materials such as chromium oxides, vanadium oxides (e.g. V_2O_5) were investigated as well as positive electrodes. But these materials have potentials against Li below 3 V, which makes them less attractive.

There have been a lot of materials synthesised which exhibits potential higher than 3 V, but three large families of lithium metal transition oxides are extensively under investigations: lithium cobalt oxides, lithium nickel oxides and lithium manganese oxides. The important aspect with these materials is they are the source of Li for rechargeable cells as it can be reversibly extracted from the structure. Li_xCoO_2 ($0<x<1$) has a theoretical capacity of 274 mA/g, however because of structural restrictions the maximum amount of Li reversibly extracted is about 0.5.Therefore the reversible capacity was reported in the range 120-140 mAh/g[84]. Alternative syntheses route were attempted to improve the cyclability of the Li_xCoO_2 electrode. But the general trend suggests that the electrochemical performance of Li_xCoO_2 has little temperature dependence. Co was also partially substituted by several metals such as Ni, Fe, Mn, or Al, however these materials have no practical applications. Furthermore the expensive cost, the toxicity and the poor safety related to Co limit the industrial applications of Li_xCoO_2 compounds.

The lower cost of the Li_xNiO_2 compounds compared to Li_xCoO_2 makes them very attractive positive electrodes. Li_xNiO_2 is more difficult to synthesise as a stoichiometric material, has lower thermal stability. The best electrochemical performance observed

for Li_xNiO_2 compounds is when their composition is close to stoichiometry. The substitution of Ni by Co or Al has shown an improvement of the capacity retention[10].

Lithium manganese oxides compounds are the most investigated materials for positive electrodes because of its low cost, low toxicity and high electronic conductivity, even if the specific reversible capacity is lower to that of Li_xNiO_2 and Li_xCoO_2. The use of $LiMn_2O_4$ as positive electrode was first reported in 1983[85]. The practical reversible capacity of this spinel is about 120 mAh/g which 80 % of the theoretical value. Although very promising, $LiMn_2O_4$ shows a capacity loss of 20 % upon cycling[86]. The capacity fade has been attributed to the Jahn-Teller effect, structural instability at high potentials and Mn^{2+} dissolution in the electrolyte. For improving the reversible capacity, was the doping of the Mn by Ni, Fe, Cr or Co but that was not successful. However the improvement of the cyclability was achieved when Li replaced small amount of Mn[87]. The performance of $LiMn_2O_4$ is intimately linked to the conditions of synthesis. Recently a new generation of Li manganese oxides, Li_xMnO_2[88] appear to be very promising positive electrode. Li_xMnO_2 is very attractive because it has the same structure as $LiCoO_2$ and had proven to have the same electrochemical performance. Plus MnO_2 is more stable than CoO_2 in liquid solvents. Other oxides such as $LiFePO_4$[89], Li_5MnO_4, $LiTi_2O_4$, LiV_2O_4 were successfully tested as positive electrodes. But they exhibit low reversible capacity at low c-rates.

1.3.2.d **The electrolyte**

The electrolyte plays an important role in battery performance as it enables the ionic transport between the electrodes. The electrolyte is a determining factor for the cell working temperature range, stability upon cycling, high rate capability and safety. Two groups of electrolyte for Li-ion cells are currently in use and under investigations. Liquid electrolytes composed of Li salts dissolved into organic solvents and polymer electrolytes, which contain Li salts inserted into a non-aqueous gel or dissolved into a high molecular weight of polymer. Good ionic conductivity, chemical and electrochemical stability towards the electrodes upon cycling, are the requirements for both types of electrolytes.

1.3.2.d.1 **Liquid electrolyte**

Liquid electrolytes are widely used in lithium batteries and were first developed for primary Li cells. Solvents should be aprotic because of the high reactivity of Li metal towards protons, which leads to hydrogen gas formation:

$$2ROH + 2Li \rightarrow 2ROLi + H_2$$

Few solvents such as cyclic alkyl carbonates emerged with the optimum combination of high conductivity, stability, low viscosity, low toxicity and low cost. Mixtures of solvents are often preferred because the combination of properties from each solvent

improves the cell performance. The solvents mainly used nowadays are cyclic or aliphatic carbonates like EC, PC, DMC (dimethyl carbonate), DEC (diethyl carbonate), EMC (ethylmethyl carbonate)[90]. The chosen solvents should also be capable as well of effectively dissolving or dissociating Li salts.

The employed Li salts should exhibit high ionic mobility of Li ions; thermal, chemical and electrochemical stability and compatibility with environment. However, the choice of Li salts is guided by stability, toxicity, safety and of course cost. $LiClO_4$ is avoided in most products for public use as it shows violent decomposition particularly in ether solutions. Other salts[17] like $LiPF_6$ and $LiAsF_6$ were found as substitutes. $LiPF_6$ is accepted although it decomposes to PF_5 and LiF around 30 °C. $LiAsF_6$ on the other hand is regarded as toxic and furthermore its electrochemical and thermal instability lead to AsF_5 and LiF. $LiSO_3CF_3$ (Lithium trifluoromethanesulphonate) is thermally and electrochemically stable but has a tendency to be associated in solution resulting in low conductivity. Other Li salts[1] like $LiN(SO_2CF_3)$ (Lithium bis trifluoromethanesulphonyl imide) and $LiC(SO_2CF_3)$ (Li tris trifluoromethanesulphonyl methide) are under investigation and seem to exhibit improved performance. These new salts display good conductivity and high stability due to their ability to sustain little ion association because of their significant charge delocalisation. In general the best performing liquid electrolytes display conductivity over 10^{-3} S/cm at room temperature.

1.3.2.d.2 Polymer electrolyte

Polymer electrolytes for Li-ion cells were developed because separators containing liquid electrolyte tend to dry progressively upon cycling and may cause non-uniformity in the stack pressure and current path. Polymer electrolytes have similar requirements as liquid electrolytes, but in addition they should also have good mechanical stability and flexibility. Either tape casting or spin coating is used to prepare thin polymer electrolyte films. Li salts used in polymer electrolytes are similar to those used in liquid electrolytes.

The first and the most studied host polymer molecule is polyethylene oxide (PEO). PEO is often associated with salts like $LiClO_4$, $LiSO_3CF_3$, $LiN(SO_2CF_3)$ or $LiBF_4$. Electrolyte formation involves Li ion coordination with oxygen atoms of the PEO polymer chains, thus the chains form a helix around Li ions. Amorphous PEO exhibits high conductivity (~ 10^{-4} S/cm) within the electrolyte but PEO tends to crystallise below 70 °C; consequently the conductivity of PEO-LiX electrolytes decreases[1].

Alternative structures such as copolymers (e.g. MEEP, polybis (methoxyethoxyethoxide)) were investigated to improve the conductivity. The average conductivity of 10^{-5} S/cm is still low compared to liquid electrolyte conductivity and furthermore, copolymers have poor mechanical properties. Further improvements in conductivity were achieved by using plasticisers such as PC or polyethyleneglycols

disregarding the loss of mechanical properties. Sufficient conductivity in polymer electrolytes is obtained when the organic solvents used in liquid electrolytes (EC or PC) are introduced into the polymer matrices (e.g. PAN, polyacronitrile or PVDF, polyvinylidene fluoride). These gel-type electrolytes combine mechanical advantages of the polymer and chemical and electrochemical properties of liquid electrolytes[5]. They exhibit conductivity near 10^{-3} S/cm at room temperature.

1.4 Structure of materials investigated as possible electrodes in this study

1.4.1 SnO_2 (Cassiterite)

Cassiterite crystallises with a tetragonal rutile structure - space group P42/*mn*m. The tin atoms form a body cubic centred lattice. The body centred of tin is co-ordinated to six oxygen atoms that form an octahedral (Figure 1.8). The rutile structure can be as well described as distorted hexagonal packed oxide arrays with half of the octahedral sites occupied by tin atoms[91].

Cell parameters: a = 4.7373, c = 3.1864

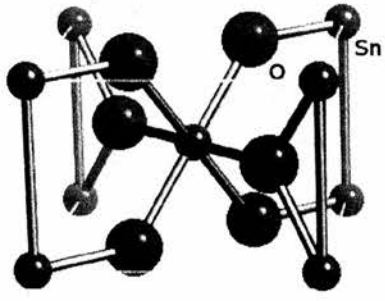

Figure 1.8 Cassiterite structure

1.4.2 **ZnO (Zincite)**

ZnO crystallises into a hexagonal wurtzite structure - space group P63mc and every atom is in tetrahedral co-ordination. The oxygen atoms form a hexagonal close packed arrangement (Figure 1.9).

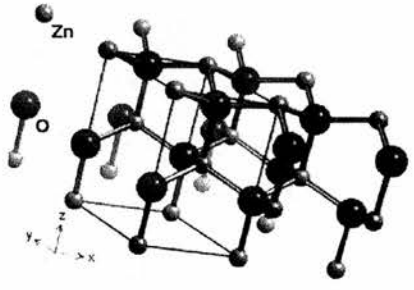

Figure 1.9 Zincite structure

Cell parameters: a = 3.2495 Å, c = 5.2069

1.4.3 **Zn_2SnO_4 (inverse spinel)**

The spinel structure is named after the mineral spinel ($MgAl_2O_4$). The spinel structure is cubic - space group Fd3m with the general formula is AB_2X_4. The X - ions form a cubic close packed network, in which the cations occupy 1/8 of the tetrahedral [4] sites and 1/2 of the octahedral [6] sites. Three cationic distributions of the spinel structure can be distinguished:

	Normal	inverse	random
	$A\ B_2\ O_4$	$B\ AB\ O_4$	$B_\gamma A_{1-\gamma}\ A_\gamma B_{1-\gamma}\ O_4$
Site	[4] [6]	[4] [6]	[4] [6]

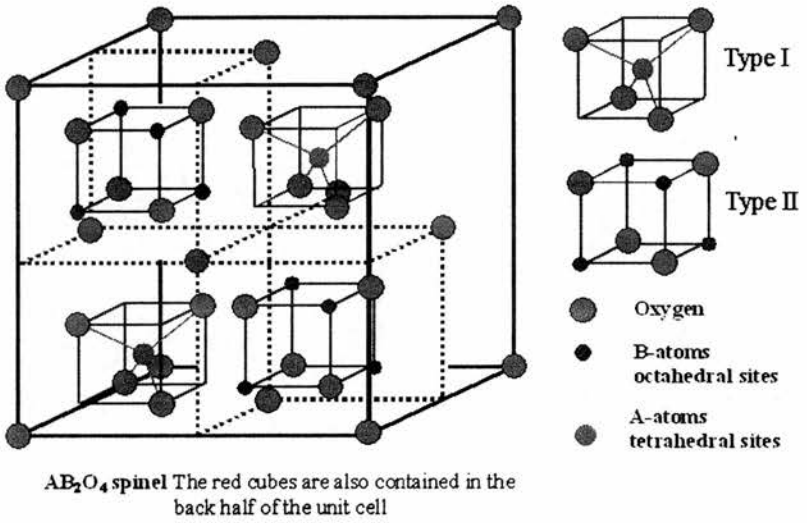

AB_2O_4 spinel The red cubes are also contained in the back half of the unit cell

Figure 1.10: Normal spinel structure

Sometimes the cation distribution may vary randomly with temperature. This variation can be quantified by using the parameter γ (γ is the fraction of atoms A on the octahedral sites).

Two types (I, II) of sub-units that fit into the octants of the face centred cubic array of anions in the unit cell are usually used to describe the spinel. The lattice of both types is cubic (a/2) and each type is alternates in the structure (Figure 1.10).

The cell parameters of the inverse spinel Zn_2SnO_4 are a = 8.70.

1.4.4 Li_2SnO_3

Li_2SnO_3 crystallises in a monoclinic structure - space group C2/c. This crystal structure was first investigated by Lang *et al.* [92-93] and finally solved by Hoppe *et al.* [94] using single crystal data. The lattice parameters (a = 5.2889(2) Å, b = 9.1872(3) Å, c = 10.0260(3) Å and β = 100.348(2)°) were confirmed by Rietveld refinement of neutron diffraction data[95]. The oxygen atoms form a distorted cubic close-packed network with the cations occupying all octahedral sites present. There are two types of metal layers perpendicular to the c axis, one composed of lithium only, the other composed of lithium and tin in a 1:2 ratio. The cations in the mixed metal layers form hexagonal close-packed planes in which the tin atoms occupy the vertices of the hexagons and the lithium atoms the centre of the hexagons (Figure 1.11).

Low temperature 'intermediate structures' of Li_2SnO_3 were reported where changes in the ordering of lithium and tin on the mixed layers lead to a loss of translational order in the c direction[96]. These low temperature 'intermediate structures' are probably metastable[94].

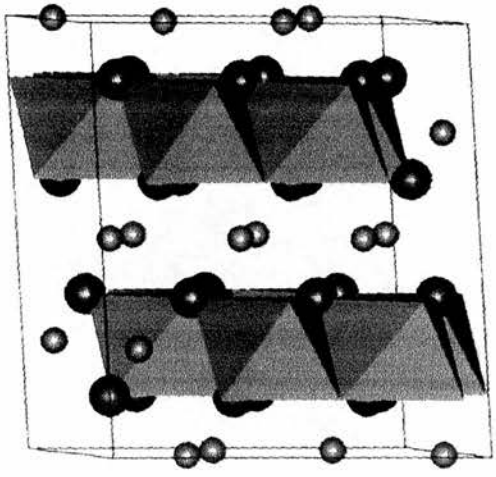

Figure 1.11: Li_2SnO_3 structure

1.5 **Aim of this thesis**

This thesis project has two main directions: the study of the mechanism occurring upon cycling and the analysis of the cycling performance of the materials investigated. The approach is the study of the interactions existing between the matrix and the metal, particularly the changes in short-range order. Li_2SnO_3, Zn_2SnO_4, $ZnO:SnO_2$ mixtures, and ZnO were tested as potential negative electrodes for Li-ion batteries. The electrodes were prepared using the "Bellcore" technology to allow EXAFS and XRD studies. The materials chosen exhibit a theoretical reversible capacity approximately over 500 mAh/g (Figure 1.12). Their reversible capacity is higher than the carbon which is used commercially so they are promising negative electrodes for Li-ion cells. Apart from studying the changes occurring in the active material during discharge and charge, the x-rays studies will allow establishing what does control the cycling performance of a material. Then optimising the cycling performance of the oxides, and finally the oxides

investigated will be compared to SnO_2, which is so far a the most studied tin-based-oxides materials.

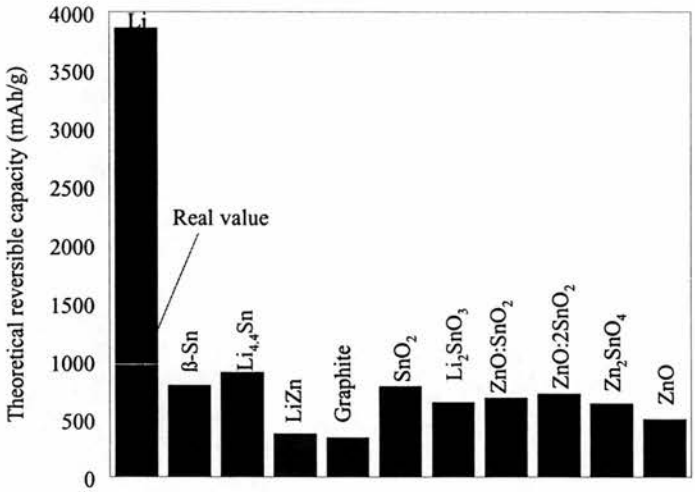

Figure 1.12: Theoretical reversible capacity (mAh/g)

1.6 **References**

1 C. A. Vincent, B. Scrosati, Modern Batteries, 2nd edition

2 R. M. Dell, D. A. J. Rand, Understanding Batteries, RSC 2001

3 G. E. Blomgren, J. Powers Sources 81-82, 112 (1999)

4 E. Peled, J. Electrochem. Soc. 126, 2047 (1979)

5 M. Winter, J. O. Besenhard, M. E. Spahr, P. Novák, Adv. Mat. 10, 725 (1998)

6 K. Brandt, Solid State Ionics 69, 173 (1994)

7 R. Koksbang, J. Barker, H. Shi, M. Y. Saidi, Solid State Ionics 84, 1 (1996)

8 G. Nagasubramanian, R. G. Jungst, J. Power Sources 72, 189 (1998)

9 G. M. Ehrlich, C. Marsh, J. Power Sources 73, 224 (1998)

10 M. Broussely, P. Biensan, B. Simon, Electrochimica Acta 45, 3 (1999)

11 I. Yoshimatsu, T. Hirai, J-I. Yamaki, J. Electrochem. Soc. 135, 2422 (1988)

12 M. Arakawa, S-I. Tobishima, Y. Nemoto, M. Ichimura, J-I. Yamaki, J. Power Sources, 43-44, 27 (1993)

13 F. Orsini, A. du Pasquier, B. Beaudouin, J. M. tarascon, M. Tentin, N. Langenhuizen, E. de Beer, P. Notten, J. Power sources 81-82, 918 (1999)

14 C. Brissot, M. Rosso, J-N. Chazaviel, S. Lascaud, J. Power sources 81-82, 925 (1999)

15 R. Selim, P. Bro, J. Electrochem. Soc. 121, 1457 (1974)

16 U. S. Sacken, E. Nodwell, A. Sundher, J. R. Dahn, Solid State Ionics, 69, 284 (1994)

17 J. R. Owen, Chem. Soc. Rev. 26, 259 (1997)

18 D. Aubarch, A. Zaban, Y. Ein-Eli, I. Weissman, O. Chusid, B. Markovsky, M. Levi, E. Levi, A. Schechter, E. Granot, J. Power Souces 68, 91 (1997)

19 D. Aubarch, A. Zaban, Y. Gofer, Y. Ein-Eli, I. Weissman, O. Chusid, O. Abramson, J. Power Sources 54, 76 (1995)

20 Y. Matsuda, T. Takemitsu, T. Tanigawa, T. Fukushima, J. Power Sources 97-98, 589 (2001)

21 A. N. Dey, J. Electrochem. Soc. 118, 1547 (1971)

22 J. O. Besenhard, J. Electroanal. Chem. 94, 77 (1978)

23 C. J. Wen, B. A. Boukamp, R. A. Huggins, W. Weppner, J. Electrochem. Soc. 126, 2258 (1979)

24 J. O. Besenhard, P. Komenda, A. Paxinos, E. Wudy Solid State Ionics 18-19, 823 (1986)

25 M. S. Foster, C. E. Crouthamel, S. E. Wood, J. Phys. Chem. 70, 3042 (1966)

26 C. J. Wen, R. A. Huggins, J. Electrochem. Soc. 128, 1181(1981)

27 D. Fauteux, R. Koksbang, J. Appl. Electrochem. 23, 1 (1993)

28 M. Winter, J. O. Besenhard, Electrochimica Acta 45, 31 (1999)

29 J. O. Besenhard, J. Yang and M. Winter, J. Power Sources 68, 87 (1997)

30 J. O. Besenhard, M. Hess, P. Komenda, Solid State Ionics 40-41, 525 (1990)

31 L. Y. Beaulieu, K. W. Eberman, R. L. Turner, L. J. Krause, J. R. Dahn, Electrochem. Solid State Lett. 4, A137 (2001)

32 S. Y. Huang, L. Kavan, I. Exnar, M. Grätzel, J. Electrochem. Soc. 142, L142 (1995)

33 J. Yang, M. Winter, J. O. Besenhard, Solid State Ionics 90, 281 (1996)

34 J. Yang, M. Wachtler, M. Winter, J. O. Besenhard, Electrochem. Solid State Lett. 2, 161 (1999)

35 B. A. Boukamp, G. C. Lesh, R. A. Huggins, J. Electrochem. Soc. 128, 725 (1981)

36 O. Mao, R.A. Dunlap, J. R. Dahn, J. Electrochem. Soc. 146 , 405 (1999)

37 O. Mao, J. R. Dahn , J. Electrochemical Soc. 146 , 414 (1999)

38 J. Santos-Pena, T. Brousse, D. M. Schleich, Solid State Ionics 135, 87 (2000)

39 G. X. Wang, L. Sun, D, H. Bradhurst, S. X. Dou, H. K. Liu, J. Alloys and Compounds 299, L12 (2000)

40 K. D. Kepler, J. T. Vaughey, M. M. Thackeray, J. Power Sources 81-82, 383 (1999)

41 O. Mao, J. R. Dahn, J. Electrochemical Soc. 146, 423 (1999)

42 G. M. Ehrilch, C. Durand, X. Chen, T. A. Hugener, F. Spiess, S. L. Suib, J. Electrochem. Soc. 147 (3), 886 (2000)

43 O. Crosnier, T. Brousse, D. M. Scheich, Ionics 5, 311 (1999)

44 K. D. Kepler, J. T. Vaughey, M. M. Thackeray, Electrochem. Solid State Lett. 2, 307 (1999)

45 C. Wang, A. S. Appleby, F. E. Little, J. Power Sources 93, 174 (2001)

46 K. Guerin, A. Fevrier-Bouvier, S, Flandrois, M. Couzi, B. Simon, P. Biensan, J. Electrochem. Soc. 146(10), 3660 (1999)

47 C. Desportes, M. Duclot, P. Fabry, J. Fouletier, A. Hammou, M. Kleitz, E. Siebert, J-L. Souquet, Electrochimie des solides, Collection Grenoble Sciences(1994)

48 P. A. Derosa, P. B. balbuena, J. Electrochem. Soc. 146, 3630 (1999)

49 Q. Liu, T. Zhang, C. Bindra, J. E. Fischer, J. Y. Josefowicz, J. Power Sources 68, 287 (1997)

50 O. Chusid, Y. Ein-Eli, D. Aubarch, J. Power Sources 43-44, 47 (1993)

51 Y. Ein-Eli, B. Markovsky, D. Aubarch, Y. Carmeli, H. Yamin, S. Luski, Electrochim. Acta 39, 2559 (1994)

52 J. Yang, T. Takeda, N. Imanishi, O. Yamamoto, J. Electrochem. Soc. 146, 4009 (1999)

53 I. A. Courtney and J. R. Dahn, J. Electrochem. Soc. 144, 2045, (1997)

54 R. A. Huggins, Solid State Ionics, 113-115, 57 (1998)

55 Y. Idota, T. Kubota, A. Matsufuji, Y. Maekawa, T. Miyiasaka, Science 276, 1395 (1997)

56 W. Liu, X. Huang, Z. Wang, H. Li and L. Chen, J Electrochem. Soc 145, 59 (1998)

57 J. Wolfenstine, J. Sakamoto and C-K. Huang, J. Power Sources 75, 181 (1998)

58 U. Heider, R. Oesten, M. Jungnitz, J. Power sources, 81-82, 119 (1999)

59 J. Zhu, Z. Lu, S. T. Aruna, D. Aubarch, A. Gedanken, Chem. Mater. 12, 2557 (2000)

60 T. Brousse, D. Defives, L. Pasquereau, S.M. Lee, U. Herterich, D. M. Scheich, Solid State Ionic 113-115, 51 (1998)

61 S. C. Nam, C. H. Paik, W. I. Cho, H. S. Chun, K. S. Yun, J. Power Sources 84, 24 (1999)

62 S. C. Nam, Y. H. Kim, W. I. Cho, B. W. Cho, H. S. Chun, K. S. Yun, Electrochem. Solid State Lett. 2, 9 (1999)

63 R. Retoux, T. Brousse, D. M. Schleich, J. Electrochem. Soc. 146, 2472 (1999)

64 H. Li, X. Huang and L. Chen, Solid State Ionics 123, 189 (1999)

65 N. Li, C. R. Martin, B. Scrosati, Electrochem. Solid State Lett. 3, 316 (2000)

66 G. R. Goward, L. F. Nazar, W. P. Power, J. Mater. Chem. 10, 1241 (2000)

67 J. Chouvin, J. Olivier-Fourcade, J. C. Jumas, B. Simon, Ph. Biensan, F. J. Fernández Madrigal, J. L. Tirado, C. Pérez Vicente, J. Electroanal. Chem. 494, 136 (2000)

68 Y. Wang, J. Sakamoto, C. K. Huang, S. Surampudi, S. G. Greenbaum, Solid State Ionics 110, 167 (1998)

69 A. Hightower, P. Delacroix, G. Le Caër, C-K, Huang, B. V. Ratnakumar, C. C. Ahn, B. Fultz, J. Electrochem. Soc. 147 (1), 1 (2000)

70 J. Read, D. Foster, J. Wolfenstine, W. Behl, J. Power Sources 96, 277 (2001)

71 J. Morales, L. Sanchez, J. Electrochem. Soc. 146, 1640 (1999)

72 J. Morales, L. Sanchez, Solid State Ionics 126, 219 (1999)

73 J. Santos-Pena, T. Brousse, L. Sanchez, J. Morales, D. M. Schleich, J. Power Sources 97-98, 232 (2001)

74 S. Morzilli, B. Scrosati, F. Sgarlata, Electrochem. Acta 30, 1271 (1985)

75 F. Belliard, J. T. S. Irvine, J. Power Sources 97-98, 219 (2001)

76 F. Belliard, P. A. Connor, J. T. S. Irvine, Solid State Ionics 135, 163 (2001)

77 A. D. Robertson, H. Tukamoto, J. T. S. Irvine, , J. Electrochem. Soc. 146, 3958 (1999)

78 D. Guyomard, C. Sigala, A. Le Gal La Salle, Y. Piggard, J. Powers Sources 68, 692 (1997)

79 M. Nishijima, T. Kagohashi, Y. Takeda, O. Yamamoto, S. Kondo, Solid State Ionics 83, 107 (1996)

80 T. Shodai, S. Okada, S. Tobishima, J. Yamaki, J. Powers Sources 68, 515 (1997)

81 P. Poizot, S. Laruelle, S. Grugeon, L. Dupont, J. M. Tarascon, Nature 407, 496 (2000)

82 S. Grugeon, S. Laruelle, R. Herrera-Urbina, L. Dupont, P. Poizot, J. M. Tarascon, J. Electrochem. Soc. 148, A 285, (2001)

83 M. S. Whittingham, J. Electrochem. Soc. 123, 315 (1976)

84 R. Koksbang, J. Barker, H. Shi, M. Y. Saidi, Solid State Ionics 84, 1 (1996)

85 M. M. Tackeray, W. I. F. David, P. G. Bruce, J. B. Goodenough, Mater. Res. Bull. 18, 461 (1983)

86 S. Megahed, B. Scrosati, J. Power Sources 51, 79 (1994)

87 P. G. Bruce, Chem. Comm. 1817 (1997)

88 A. R. Armstrong, H. Huang, R. A. Jennings, P. G. Bruce, J. Mater. Chem. 8, 255 (1998)

89 A. Yamad, S. C. Chung, K. Hinokuma, J. Electrochem. Soc. 148, A224 (2001)

90 U. Heider, R. Oesten, M. Jungnitz, J. Powers Sources, 81-82, 119 (1999)

91 http://www.webelements.com/

92 G. Lang, Z. Anorg. Allg. Chem. 276, 77 (1954)

93 G. Lang, Z. Anorg. Allg. Chem. 348, 246 (1966)

94 G. Kreuzburg, F. Stewner, R. Hoppe, Z. anorg. allg. Chem. 379, 242 (1970)

95 J. L. Hodeau, M. Mazeiro, A. Santoro, R. S. Roth, J. Solid State Chem. 45, 170 (1982)

96 V. M. Trömel, J. Hauck, Z. Anorg. Allg. Chem. 373, 8 (1970)

2 Experimental

2.1 Electrochemical testing

2.1.1 Electrode preparation

The porous anode material was based on the "Bellcore"-type plastic electrodes[1] and the preparation on the method[2-3] of Dahn to allow *in-situ* x-ray and EXAFS studies. The carbon and the active material were pre-ground together before addition of binder to obtain a uniform electrode and a better response of the electrode[4]. The slurry was stirred at 50 °C for 4 hours then was spread on a glass plate using a doctor blade with a blade gap of about 0.3 mm. The electrode sheet left to dry in air has a thickness between 50 and 70 μm. 15 mm diameter discs of the sheet were cut and then immersed in ether to remove the PC. This was repeatedly weighed several times until a constant mass was reached. Finally the porous electrode discs were dried under vacuum overnight before transfer into the glove box.

Electrodes were prepared by combining 11.6 % by weight of active material, 1.4 % by weight of Super S carbon, 5.5 % by weight of poly(vinylidene) fluoride (PVDF) and 9.5 % by weight of propylene carbonate (PC) in 72 % by weight of acetone to form a slurry. Super S carbon is used to provide better conductivity through the electrode, PVDF as binder. The PC was introduced in the electrode preparation in order to obtain porous anode. When PC is removed the anode becomes porous. The pores are then filled by the electrolyte and thus the distribution of the electrolyte within the anode is homogeneous.

The percentage of the active material (A) present in the electrode was calculated as per equation 2.1. The PVDF in the electrode is assumed to be relatively inert during electrochemical insertion. Li can be inserted into Super S carbon to a limit extent and capacities have been corrected in accord with the carbon content (see chapter 3 for carbon insertion characteristics). Thus the percentage of A in the electrode is equal to:

$$\text{Equation 2.1} \qquad \frac{\text{mass of A}}{\text{mass of A + mass of PVDF + mass of carbon}} * 100$$

2.1.2 Cell preparation

2.1.2.a Standard cell

A 2325 coin cell manufactured by the National Research Council of Canada was used for all the electrochemical tests. Lithium foil with a diameter of 16 mm, slightly larger than the anode disc, was used as a counter and reference electrode. The Li electrode diameter is slightly bigger than the anode electrode, in order to decrease the overpotential. $LiClO_4$ in EC-DMC was used as electrolyte. The separator, glass microfibre GF/F (Whatman) has a diameter of 17 mm. The diameter of the separator is larger than the diameter of both electrodes to avoid any short-circuits during the crimping process. The internal stack pressure of the cell that is proportional to the stack height should be calculated, so those cells can be prepared with similar conditions. The ideal stack height of the 2325 coin cell that gives the correct stack pressure, is 2.59 mm before crimping. The thickness of the cell parts and the experimental stack height used are summarised in Table 2.1.

	Thickness (mm)
Anode: active material	0.05-0.07
Separator: glass microfibre	0.27
Cathode: lithium	0.3
Spacer: stainless steel	0.864
Spring: stainless steel	1.118
Experimental stack height	**2.602-2.622**

Table 2.1 Thickness of the cell parts

The schematic representation of a standard coin cell is shown in Figure 2.1. Batteries were assembled in an Ar-filled glove box. The anode was placed in the middle of the positive stainless steel coin cell case, and then around 7 drops of electrolyte were placed onto the electrode. The separator was placed on top of this, and then the Li electrode. After this, the spacer and the spring were placed successively on top of the Li electrode. Finally the negative stainless steel coin cell framed with an insulating grommet was positioned above the spring.

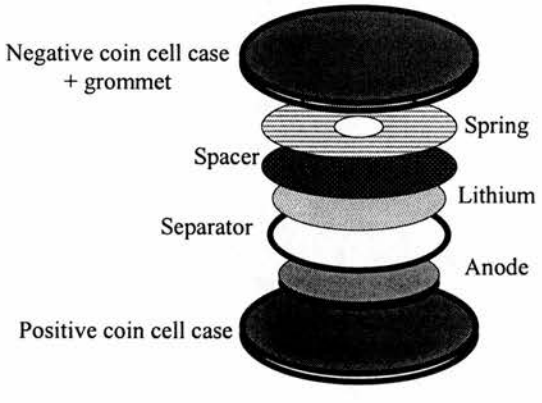

Figure 2.1: Schematic representation of a battery

In the early electrochemical tests, two Celgard 3501 discs, 0.025 mm thick with a diameter of 20.99 mm, were used as separator. To approach the ideal value of the stack height two stainless steel spacers, 0.711 and 0.254 mm thick were used. The experimental stack height was then only about 2.48 mm. The glass fibre separator exhibited presumably improved performance compared to the Celgard separators due to it providing larger stack pressure.

2.1.2.b *In-situ* cell

Special cells were designed to perform *in-situ* measurements based on the standard coin cell described in section 2.1.2.a. The cross sectional representation of the *in-situ* cell showing a x-ray travelling through the cell is shown in Figure 2.2. A 5 mm hole was punched in the middle of both cell cases, and in the centre of a 0.254 mm thick spacer. A 0.25 mm thick polyethylene terephtalate (PET) window was glued onto the inside of the positive cell case, whereas for the negative cell cases a 0.125 mm thick kapton window was used. The PET and kapton windows had a diameter of 10 mm. PET was chosen for the positive case because it is more rigid than the kapton and so gives better stack pressure. Two different glues were used, "Roscoe bond" and "Torr seal epoxy". The "Roscoe bond" glue was attacked by the electrolyte during the assembling of the cell so the "Torr seal epoxy" glue was used instead to attach the PET on the positive case. The "Roscoe bond" glue was only used to glue the kapton onto the negative case. To supply electric conductivity, a 0.0075 mm thick Ni foil or a 0.015 mm thick Zr foil with a diameter of approximately 19 mm was placed on the PET window. The choice of the foil was limited to those unable to form significant

alloys[5,6] with Li and depends on the percentage of x-ray absorption depending of the wavelength.

Despite these modifications, the assembling process was however similar to the standard cell. The contacting foil was placed in the centre of the positive case on the PET window followed by the anode in the middle of the foil. Then approximately 8 drops of electrolyte and two Celgard separators were placed on top. When the glass fibre separator was used about 50 % of the batteries were short-circuited due to the ripping of the separator caused by the PET window during crimping. Thus the Celgard separator was preferred despite its lower performance, because of its greater mechanical resistance to tearing on crimping in the *in-situ* cells. The Li electrode was positioned over the separator followed by a PET spacer to keep the Li flat. A small piece of Ni foil was folded on both sides of the PET spacer to guarantee electric conductivity through the battery. The Ni foil was maintained by inserting it into a small cut made on the PET spacer. The punched spacer and the spring were placed on top of the PET spacer and finally the negative case. The stack height of this cell with all the modifications was about 2.41 mm plus the glue thickness that was estimated between 1 and 2 mm thick. Thus the stack height of the *in-situ* cell is close to the ideal stack height.

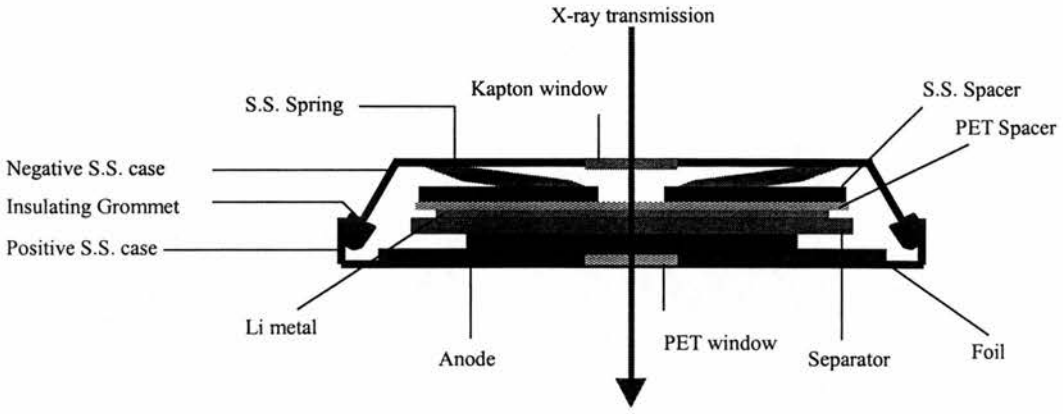

Figure 2.2: Coin cell cross section for *in-situ* measurements

The cell described above was used to collect both EXAFS and XRD data at the Daresbury Laboratory synchrotron radiation source. A similar cell design was used to perform XRD on a STOE powder diffractometer in St Andrews. Two changes were made, a 1.48 mm thick copper grid replaced the foil and so no stainless steel spacer was used. The stack height of these special cells was about 3.33 mm which was 30 % over the theoretical value (2.59 mm).

2.1.3 Electrochemical test conditions

Electrochemical tests were performed on both a Macpile II and a 2200 Maccor battery testing systems under computer control. Two modes, galvanostatic and potentiostatic were used. In both modes, between each sweep the cell was relaxed for 1 hour.

- Galvanostatic mode

In this mode the current applied to the cell is constant and the potential is recorded. Two currents were typically used 0.05 mA and 0.1 mA that correspond to a current density of 0.0283 and 0.0566 mA/cm^2 respectively. Tests were typically made within window voltages between 0.01 and 2 V.

- Potentiostatic mode

In this mode potential is swept at a slow rate and the current is recorded. Tests were usually made at a fixed scan rate, 20 mV/h between 0.01 and 1.8 V. This method is useful in order to understand the processes occurring on cycling as peaks reveal the presence of an electrochemical process.

In the case of *in-situ* cells, currents of 0.1 mA or higher were usually used. At a defined voltage the electrochemical test was stopped, then the battery was relaxed for at least one hour before performing the *in-situ* measurements. The lifetime and the electrochemical performance of these cells are lower than the standard cells

2.1.4 Theoretical capacities and lithium inserted/de-inserted per atom

In chapter 1, a mechanism[2] of Li insertion was suggested for tin-based materials. This mechanism seems to be valid for other oxides[7] such as PbO, ZnO, Sb_2O_3, Fe_2O_3... thus a general equation for metal oxides can be written:

Equation 2.2 $MO_x + 2xLi^+ + 2xe^- \rightarrow xLi_2O + M$ *irreversible capacity*

Equation 2.3 $yLi^+ + M + ye^- \leftrightarrow Li_yM$ *reversible capacity*

The equations above allow the determination of the theoretical number of Li ions inserted/de-inserted per active material unit during the first cycle. The number of Li ions was based on the most Li rich alloy reported for a metal as shown in Table 2.2. Theoretical capacities expressed in mAh/g were calculated from the number of Li ions and the equation below:

1 mole of Li ion = 26810 mAh

All theoretical capacities and Li ions inserted/de-inserted per active material unit during the first cycle are summarised in Table 2.3 for all materials investigated.

Metal	Highest Li alloy	Potential (mV)	References
Sn	$Li_{4.4}Sn$	380	8
Zn	$Li_{1.5}Zn$	5	9

Table 2.2: Highest Li-Sn alloys and Li-Zn alloys

	Li inserted per active material unit	1st irreversible capacity (mAh/g)	Li de-inserted per active material unit	1st reversible capacity (mAh/g)
SnO_2	8.4	1501	4.4	786
Li_2SnO_3	8.4	1233	4.4	643
ZnO	3.5	1155	1.5	496
$ZnO:2SnO_2$	20.3	1416	10.3	718
$ZnO:SnO_2$	11.9	1372	5.9	681
$2ZnO:SnO_2$ & Zn_2SnO_4	15.4	1316	7.4	633

Table 2.3: Theoretical capacities and Li inserted/de-inserted per active material unit

2.1.5 Experimental C-rates

C-rate is the time needed to discharge or charge completely a battery. The C-rate can be calculated from the theoretical capacity (mAh/g) or from the experimental number of Li inserted/de-inserted. However it can be found in the literature the calculation of the C-rate based on one Li inserted or de-inserted[10]. During the electrochemical tests two current density 0.0283 and 0.0566 mA/cm^2 that corresponds to 0.05 and 0.1 mA respectively were used. Consequently the C-rate used is different for each electrode depending on the mass of the active material. The electrode contains a typical average mass of the active material of 7±1 mg. Thus an average of the two C-rates used during testing can be calculated and the values are summarised in Table 2.4. The calculation of the C-rates presented Table 2.4 were based on the capacity expressed in mAh/g.

When applying a current of 0.1 mA the C-rate during charging is between C/35 and C/50 that is approximately 50 times more than the normal C-rates reported for Tin-Based-Oxides materials[11-12-13-14]. These C-rates appear very low compared to the literature because the calculation was based on the capacity and not on 1 Li. Low C-rates were used because at higher C-rate the electrochemical performance of the electrode decreased because of the preparation of the electrode. The "Bellcore" type electrode was chosen to allow in-situ investigations during testing disregarding the reduction of electrochemical performance. In the literature the electrochemical performances of the electrodes using high rates such as C/1 or C/5 remain excellent and better because the electrode preparation is different. These electrodes are either deposited by CDV or coated on a current collector (stainless steel or copper) [11-15].

	Discharge rate 1	**Charge rate 1**	**Discharge rate 2**	**Charge rate 2**
SnO_2	C/210	C/77	C/105	C/39
Li_2SnO_3	C/172	C/90	C/86	C/45
ZnO	C/162	C/69	C/81	C/35
ZnO:SnO_2(1:2)	C/198	C/97	C/99	C/49
ZnO:SnO_2(1:1)	C/192	C/95	C/96	C/48
ZnO:SnO_2(2:1) & Zn_2SnO_4	C/184	C/88	C/92	C/44

Table 2.4: Experimental C-rates of the materials investigated

2.2 **Techniques**

2.2.1 X-ray diffraction

2.2.1.a X-rays generation

X-rays are electromagnetic radiation with wavelengths around 1 Å between the ultraviolet and γ-rays. X-rays are commonly generated when a beam of accelerated electrons hits a target metal plate, e.g. copper. As a result, a core electron from the target metal can be ejected from the atom and another electron drops to the vacant 1s level; the transition energy is fixed. Most of the energy released during the transition is converted into heat and only a small fraction into x-ray radiation.

In the x-ray spectrum, two types of emission are superposed. The first emission results from the conversion of kinetic energy into electromagnetic radiation during the collision between the beam of electrons and the target metal and is called Bremsstrahlung radiation. The second emission spectrum results from the characteristic radiation of the target metal.

Copper, widely used in diffraction experiments emits two characteristic radiations K_α and K_β. They correspond respectively to the $2p \rightarrow 1s$ and $3p \rightarrow 1s$ transitions and are shown as a close doublet in the emission spectrum. $K_{\alpha 1}$ is the most intense peak and hence, is commonly used in x-rays diffraction. Most diffraction experiments require monochromatic x-rays that can be achieved by using either a filter or a single crystal monochromator.

The metal chosen as a filter should generally have an atomic number one or two less than the target metal. Consequently, the energy required to ionise the 1s electrons of the filter is slightly less than the radiation K_α of the target metal thus K_β radiation and most of the Bremsstrahlung radiation is erased. As a result, the x-ray beam emerging from the filter consists of monochromatic K_α radiation where $K_{\alpha1}$ and $K_{\alpha2}$ are still present. As an example, nickel is an excellent filter for copper radiation because it absorbs the CuK_β radiation and produces monochromatic CuK_α radiation for diffraction measurements.

An alternative way of removing undesired wavelengths from the x-rays beam is to use a single crystal and so providing an intense convergent beam. Emerging from the x-ray tube, the beam hits an orientated single crystal monochromator, which diffracts the incident beam at the Bragg angle. Just one wavelength can be diffracted from the crystal at a specific angle following the Bragg's law (see section 2.2.1.b).

In the case of a synchrotron, the electrons are accelerated periodically in a circular accelerator, and the electrons emit radiation as they travel round the curves. The radiation produced is called synchrotron radiation. This loss of energy is proportional to the electron energy and is greater for sharper curves. An advantage of synchrotron radiation is that the Bremsstrahlung radiation can be used as an intense source of x-rays with a lot of wavelengths.

2.2.1.b Bragg's law

Bragg's law is a practical law for description of x-ray diffraction. The idea is to consider the crystal as built from planes and each plane behaves like a semi-transparent mirror. The incident x-ray beam hits each plane of an angle, θ and some of the x-rays are reflected with the same angle θ (Figure 2.3). The main part of the x-rays are transmitted and then subsequently reflected by successive planes, with the same angle θ.

Figure 2.3 shows two parallel x-ray beams, 1 and 2 which hit two adjacent planes within the crystal. The reflected beams 1' and 2', are also parallels. Beam 22' covers an extra distance, BCD, compared to beam 11'. This additional distance is equal to a whole number of wavelengths for allowing the beams 1' and 2' to be in phase.

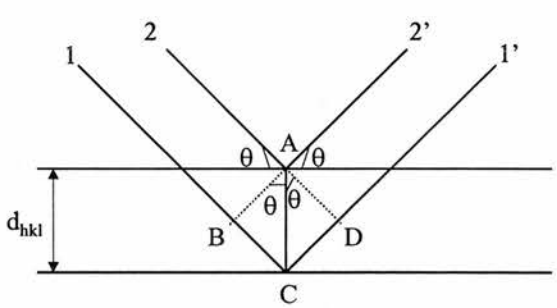

Figure 2.3: Derivation of Bragg's law

First $BC = CD = \sin\theta d_{hkl}$ d_{hkl}: d-spacing, distance between planes

$BCD = 2d_{hkl}\sin\theta$ hkl: Miller indices

Then $BCD = n\lambda$ θ: Bragg angle

As a result $\mathbf{n\lambda = 2d_{hkl}\sin\theta}$ Bragg's law

2.2.1.c Powder diffraction techniques

2.2.1.c.1 Introduction

Powder diffraction techniques are widely used to analyse powder samples and give an indication of crystallinity and allow phase identification. Each crystalline phase exhibits a characteristic powder diffraction pattern, which allows identification. A random arrangement of crystal orientations is obtained when the sample is well prepared as an uneven sample leads to preferred orientations and may induce intensity errors in the diffraction pattern. Preferred orientations affect materials, which crystallise with a non-spherical shape, e.g. cubes that break into smaller pieces on crushing. Then in a powder aggregate of such materials, the crystals tend to sit on their face. Thus the orientation obtained is far from an average orientation.

The powder diffraction technique allows the determination of the angle of diffraction, 2θ, (or the associated d-spacing, d_{hkl}). The x-ray beam strikes a powdered sample and the beam is diffracted according to Bragg's law. The diffracted beam can be detected many ways typically by photographic film (Debye-Scherrer or Guinier focusing methods) or by a movable Geiger-Muller (Figure 2.4).

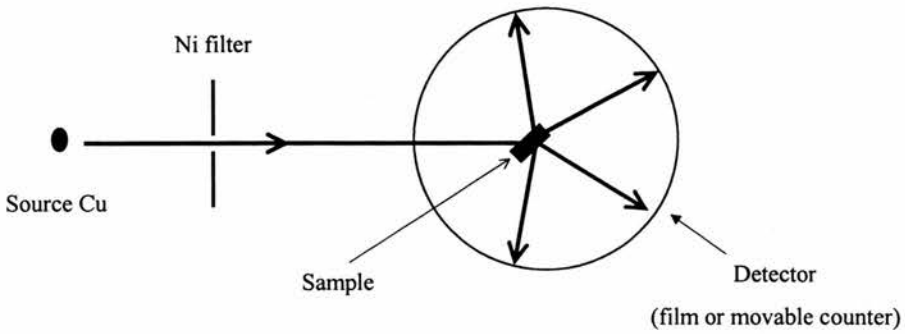

Figure 2.4: Powder technique representation

2.2.1.c.2 Powder diffractometer

In the powder diffractometers used in St Andrews, a Geiger-Muller tube is used as detector to measure the position of the diffracted beams and x-rays intensities are plotted as a function of the reflected angle, 2θ. A higher resolution powder diffraction pattern can be obtained by using a focusing method that provides an intense beam. The principle is to arrange the x-ray source, the sample and the detector in a way that all of them lie on the circumference of a focusing circle as shown in Figure 2.5.

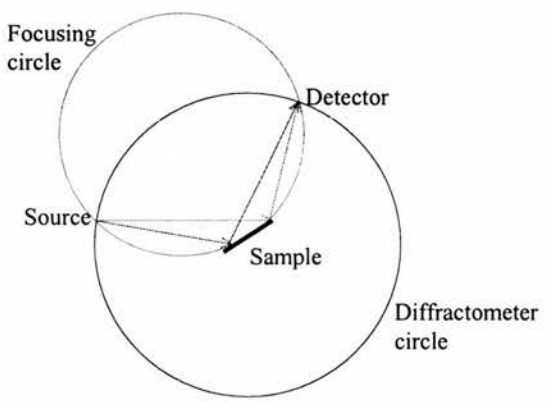

Figure 2.5: Diffractometer with a focusing geometry

The radius of the focusing circle is inversely proportional to the Bragg angle θ and the diameter of the diffractometer circle is constant. In practice having a flat sample is recommended to avoid losing the benefit of the focusing method. To maintain the focusing action, the surface of the sample should remain tangential to the focusing circle. This is achieved only if the detector scans at an angular velocity of 2θ/min while the sample rotates at θ/min in the same direction.

2.2.1.c.3 Practical

Powder x-ray diffraction measurements were performed in reflection mode on a Philips diffractometer and in transmission mode on a STOE (STADIP) diffractometer both with CuK_α radiation. For the Philips diffractometer samples were mounted in an aluminium holder. In the STOE diffractometer the sample rotates to erase preferred orientations. The sample holder used for powder is a 4 cm diameter, 5 mm thick disc. On one side of the sample there is a 2.1 cm diameter hole and on the other side a 1.2 cm diameter hole. The sample is sitting inside the 2.1 cm diameter hole between two 2.1 cm diameter mylar films, which are fixed by two screws. A schematic representation of the holder is shown Figure 2.6. The STOE diffractometer was used to perform *in-situ* and *ex-situ* measurements on the anode materials. In both diffractometers, XRD measurements were performed at 40 kV and 35 mA.

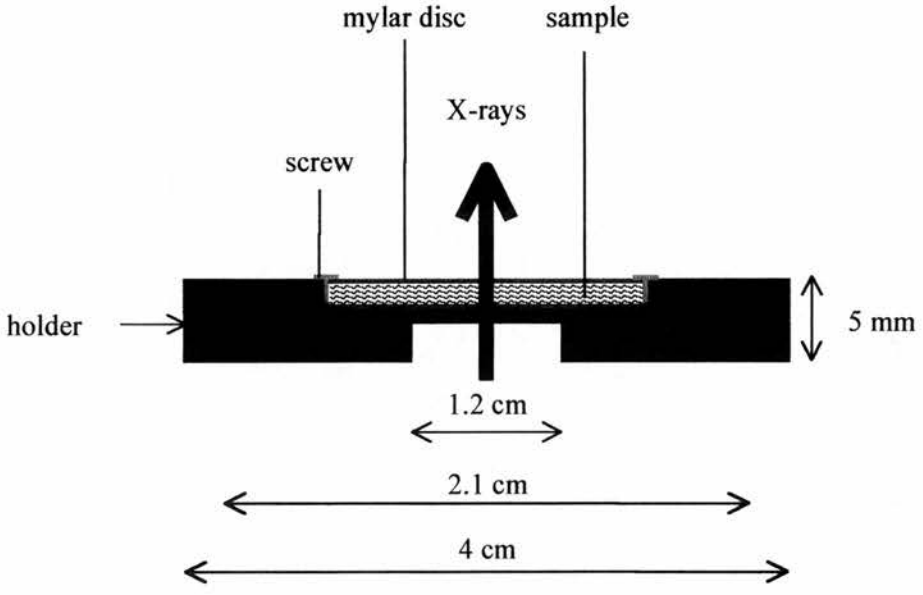

Figure 2.6: STOE diffractometer sample holder

- *In-situ*

A similar holder used to that used to collect XRD on the STOE was used to perform the *in-situ* XRD. The 2.1 cm diameter hole shown in Figure 2.6 was increased to 2.3 cm to fit the battery that was fixed with the two screws. The pattern was collected between 10 and 80° over about eight hours. This long time was necessary because the PET and kapton windows, the PET spacer, the separator and the electrode absorbed most of the x-rays during the measurement.

- *Ex-situ*

The same holder that was used for characterising initial powders (Figure 2.6) was used to perform ex-situ XRD; the only difference is that the sample preparation was made inside the glove box. The battery was dismantled then the anode was washed with dry PC for at least 10 minutes to remove the electrolyte. The anode was then placed between two thin mylar discs normally used for sample powder. The anode

was placed wet between the mylar dics to obtain a reasonable seal. A Cu grid was added to be used as internal standard. XRD was collected between 10 and 70 or 80° for 1.5 hours.

2.2.1.d Crystallite size measurement

The average size of the crystallite affects the peak shape observed in a powder diffraction pattern. Extra broadening of the diffracted x-ray beam may occur in crystals where the average size of the particle is less than about 200 nm. The measurement of the broadening can give an indication of the average value of the particle size. Small particle size leads to broad peaks because diffraction occurs at an angle θ slightly different to the Bragg angle θ.

The particle size broadening is estimated by the Sherrer[16] formula:

$$t = 0.9\lambda / [(B_M^2 - B_S^2)^{½}\cos\theta]$$

Where t is the crystallite size in Å of and λ is the wavelength used by the diffractometer e.g. $\lambda = 1.54056 \times 10^{-10}$ m for CuK_α radiation. B_M and B_S are the FWHM in radians of the sample and a standard respectively. The standard value is usually obtained from a highly crystalline material such as silicon. The calculation was only performed for peaks with significant intensities.

Another technique, a laser system particle analyser (Coulter Counter LS 100) was also used to determine the particle size of the inverse spinel Zn_2SnO_4. The particle size distribution can be determined within an overall range of 0.4-1000μm by this method. Samples are held in suspension in aqueous solution and the particles are forced through a small opening where they are hit by a laser. The scattering angle obtained depends on the particle size. Colin Cameron from the Geosciences department of the University of St. Andrews collected this data.

2.2.2 Extended X-ray Absorption Fine Structure (EXAFS)

2.2.2.a Overview

EXAFS is a very useful and powerful technique for the determination of the local structure about an absorbing atom, especially the bond distances. Kronig[17] discovered EXAFS at the beginning of the 20th century, however it was not until the 1970's, that Stern *et al.* [18, 19, 20] and Lee[21] developed the technique so that it could be used for structure determination. EXAFS[22] is suitable for studying crystalline or amorphous materials, liquids and even gases, because it examines the local structure around particular absorbing element, as it is a short-range technique. In contrast conventional XRD, which is a long-range technique, allow for all elements the determination of the average position. As the EXAFS technique is element specific, impurities other than the absorbing atom will not interfere during the measurement.

EXAFS data can be collected in different modes such as transmission, x-ray fluorescence (XRF), total electron yield (TEY) or optical luminescence (XEOL) as

shown in Figure 2.7. The transmission mode is often favoured because of the simplicity of data analysis and interpretation. For the EXAFS experiment a synchrotron radiation source is commonly used. The synchrotron produces polychromatic x-rays, which are selected (energy band width 1 eV) by diffraction from a double silicon crystal monochromator. At the first crystal some x-rays are diffracted and the second crystal comparable to a mirror, redirects the diffracted x-ray beam into its original direction, according to Bragg's law.

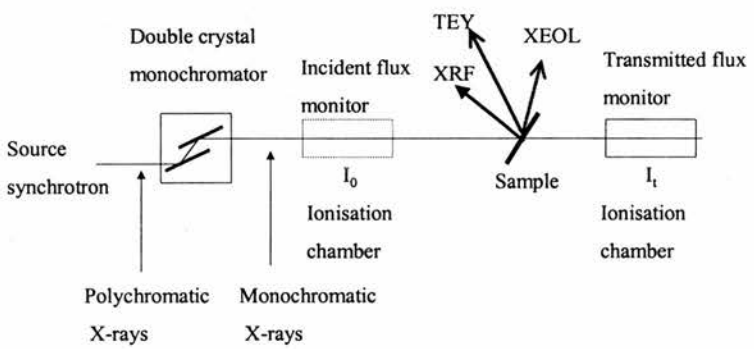

Figure 2.7: Schematic representation of an EXAFS experiment

2.2.2.b Description

During x-ray absorption, a photon with sufficient energy can ionise an electron from a deep core level of the absorbing element to an empty state located above the Fermi level (E_F). This ionisation process shows an absorption edge in the x-ray spectrum. Magnitude, position and shape of the absorption edge is characteristic for the oxidation state of each element. The final energy state reached after absorption depends on the kinetic energy of the excited electron. The excited electron waves interact with the electron shells of neighbouring atoms leading to backscattering. In

Figure 2.8, the waves (solid lines) emanating from the absorbing atom are backscattered by the neighbouring atoms (dashed lines).

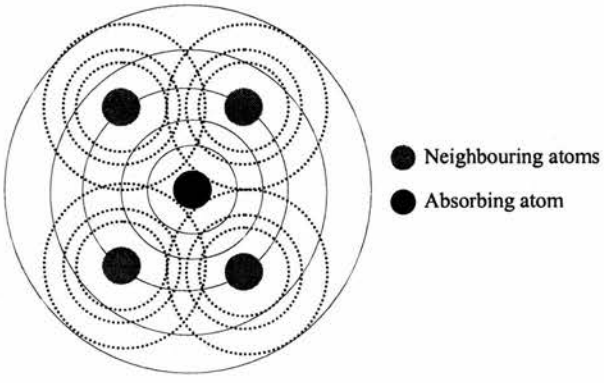

Figure 2.8: Backscattering phenomena

Thus backscattered waves interfere with the forward waves from the absorbing atom, and this changes the probability of electron ejection and therefore the probability of photon absorption. Practically that leads to oscillations known as EXAFS as shown in Figure 2.9.

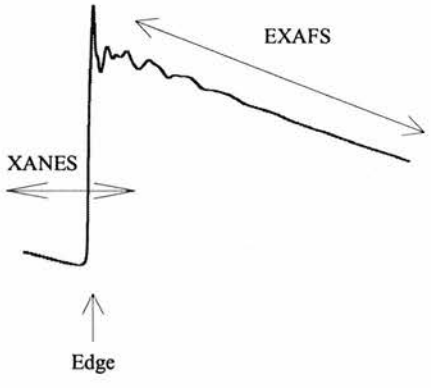

Figure 2.9: K shell absorption of Zinc

The frequency of the oscillation is related to the bond distance between the absorbing (or scattering) atom and the neighbouring atoms. The amplitude of these oscillations

is related to the number and type of scattering centres. In an EXAFS spectrum, EXAFS oscillations of the various coordination shells around the scattering atom are superposed. The Fourier Transform of the EXAFS data is used to visualise the co-ordination number and the local ordering which affects the bond distance.

2.2.2.c Analysis

Collected EXAFS data needs to be calibrated, summed and background subtracted before fitting to extract useful structural information. The programs[23,24] ECABS, EXCALIB and EXCURV98 were used to process the data. When using ECABS the type of silicon crystal and the gain value I_0/It (I_0 and I_t correspond to the incident and the transmitted x-rays intensities respectively) are required.

Data collected were calibrated in EXCALIB. The calibrated files were background subtracted in ECABS. Often during data collection, glitches from the crystal appear, so it was preferable to remove the glitches in a text editor program before performing any background subtraction to obtain clean data.

The program EXCURV98 uses a model to describe the local environment around the scattering atom and EXAFS is calculated from this model. This model is compared with the experimental data before the fitting. Another program included in EXCURV98 was written to calculate the phase shift of each atom and consequently the potential of each atom that has been defined by their scattering properties was calculated. The actual fitting starts when a radial shell model of the atoms around the

central atom is defined. Each shell has four principal parameters: the type of atom, the number of atoms, the bond distances between the atom shell and the centre atom, and the Debye-Waller factor which expresses static and thermal disorder. These four parameters can be refined separately or together, however it is better at the beginning of the refinement to refine each parameter separately. There is a fifth parameter, energy of Fermi (EF) that should be taken into account during the refinement. EF is the difference between the theoretical Fermi energy calculated from the potentials and the EF assigned to the edge position.

In these samples, at least two types of compounds are often present, oxides and metals; thus the notion of clusters had to be introduced. Each cluster corresponds to a type of compound and has its own shells and parameters. In the case of multiple clusters, parameters of each individual cluster should be refined separately. For the data presented here usually three shells give a satisfactory fit and identification.

2.2.2.d Experiment

EXAFS were collected in transmission mode in Combined XRD Fast scanning mode at the station 9.3 in Daresbury Laboratory Synchrotron Radiation Source (UK), with the assistance of Dr. Ian Harvey. The beam used had an average diameter of approximately 3 mm and the sample is at an angle of 45° to the beam to allow the collection of XRD simultaneously. The K absorption edges of zinc and tin are 9660 and 29200 eV respectively.

To perform *in-situ* EXAFS measurements, the coin cell was modified to allow this experiment as described in section 2.1.2.b. The difficult task is the choice of the current collector as it should not insert Li and not absorb the x-rays.

For *ex-situ* EXAFS measurements, the sample preparation is different. The battery was dismantled in the glove box then the anode was washed with dry PC for a minimum of 10 minutes to remove the electrolyte. As described in section 2.1.2.b, a 5 mm hole was punched in both coin cell cases and a kapton window was glued onto the inside of both cases. The anode was then placed between both coin cell cases then the cell was crimped inside the glove box. These coin cells were chosen for *ex-situ* measurements because they provide a good seal for the air sensitive anodes.

EXAFS measurements were made on the zinc and tin edges. Either a 0.015 mm thick zirconium foil or a 0.0075 mm thick nickel foil, are suitable current collectors for the tin edge as nearly 75 % and 93 % of the energy are respectively transmitted. Zirconium foil was used as a current collector when performing EXAFS on the zinc edge because a 0.015 mm thick zirconium foil transmits 45 % of the energy and does not significantly alloy with Li. Some of the samples contain zinc and tin so, zirconium was used as measurements were made on zinc and tin edges.

2.2.3 Scanning electron microscopy (SEM)

In electron microscopy, electrons rather than photons are used in order to produce a higher resolution image. Electron microscopy is an extremely flexible technique and can be carried out in reflection (SEM) or transmission (TEM) mode. SEM provides microstructural information such as surface, texture and particle size at a wide range of magnifications and details down to 10^{-8} m can be observed.

A schematic representation of a SEM instrument is shown in Figure 2.10. In the electron gun, an electron beam is generated, usually from a filament of tungsten, which also forms the cathode of the instrument. The generated electron beam is accelerated by an anode, condensed by a magnetic lens and finally focused using an objective lens. When the electron beam hits the sample, photons and various electron signals and x-rays are emitted. However backscattered electrons or x-rays are most commonly used for SEM.

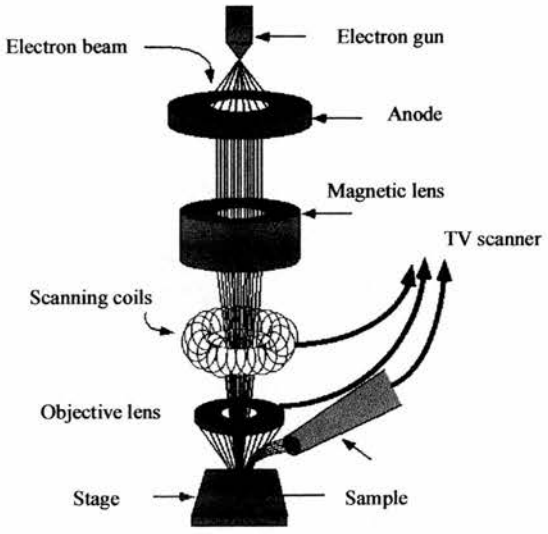

Figure 2.10: Schematic representation of a SEM set up

Highly conductive samples, like metals, can be analysed directly in a SEM, however insulating samples need to be coated with a thin conductive layer, such as gold, to allow an electron flow and to prevent the built-up of surface charge.

SEM measurements were performed on conductive and semi-conductive samples using a JEOL 5600 SEM. Some of the semi-conductive materials viewed by SEM showed a built-up of surface charge. So these materials were pressed into pellets then coated with gold before making the measurement to make them more conductive and more readily viewed by SEM.

2.3 **Materials**

2.3.1 Synthesis method

Most materials were used as prepared. However some materials were required to be made by standard solid state reaction synthesis. Powder materials were intimately mixed together under acetone in order to obtain a homogeneous paste before firing. The powders were mixed by either hand-grinding or ball-milling. Grinding was carried out in an agate mortar and pestle. Usually a minimum of 20 minutes was sufficient. Commonly, materials[25] are synthesised by repeated hand-grinding and firing at high temperatures, above 1000 °C. At such high temperatures, only the thermodynamically stable phases can be synthesised, which is a limitation of firing.

Ball-milled products have much smaller grain sizes than hand-ground products and hence, are more chemically active. Ball-milling was carried out in a Planetary Micro Mill "pulverisette-7" ball-mill, with zirconia 7 grinding balls (12 mm diameter) and mills (25 ml volume). 6-7 g of the powder was mixed with 15 ml of acetone and milled for 10-50 hours. Milling before sintering can allow a solid state reaction to be carried out at relatively low temperatures or over shorter periods of time, compared to hand-ground samples.

2.3.2 $ZnO:SnO_2$ systems

Previous work has shown that some syntheses can be performed mechanically[26] by ball-milling, for example $LiMO_2$ (M= Ti, Fe). So SnO_2 (cassiterite) and ZnO (zincite) were ball-milled together to produce fine particles to be used as active materials and to attempt to synthesise new compounds mechanically. ZnO and SnO_2 were mixed in molar ratios of 1:1, 1:2 and 2:1. After a certain milling time, a small sample (~1g) was removed for testing and the remainder returned for further milling. XRD was performed on all batches in order to identify the different phases present. All batches were used as active material without any heating.

2.3.3 Inverse spinel Zn_2SnO_4

The inverse spinel[27, 28] Zn_2SnO_4 was prepared by both ball-milling for 12 hours and by hand-grinding stoichiometric amounts of ZnO and SnO_2 together. The ball-milled oxides were sintered at 1000° C for 16 hours and the hand-ground oxides 1100° C for 24 hours. The resulting XRD pattern matches the JCPDS-ICDD number, 24-1470 recorded for the spinel.

2.3.4 Li_2SnO_3

SnO_2 (cassiterite) was milled for 12 hours under acetone using zirconia balls prior to hand-grinding with Li_2CO_3 in stoichiometric amounts. The resultant mixture was first fired at 450 °C to remove CO_2, thereafter at 650 °C to form low temperature (LT) Li_2SnO_3. High temperature (HT) Li_2SnO_3 was prepared at 1000°C from non-milled cassiterite and Li_2SnO_3. Both LT and HT Li_2SnO_3 display the same XRD pattern which matches the JCPDS-ICDD number, 31-761.

2.4 References

1 A. S. Gozdz, C. N. Schmutz, J. M. Tarascon, P. C. Warren, U.S. Patent 5, 552, 239 (1996)

2 I. A. Courtney, J. R. Dahn, J. Electrochem. Soc. 144, 2045, (1997)

3 M. N. Richard, I. Koetschau, J. R. Dahn, J. Electrochem. Soc. 144, 554 (1997)

4 K. M. Kim, W. S. Jeon, I. J. Chung, S. H. Chang, J. Power Sources 83, 108 (1999)

5 M. Winter, J. O. Besenhard, Electrochimica Acta 45, 31 (1999)

6 M. Winter, J. O. Besenhard, M. E. Spahr, P. Novak, Electrochimica Acta 10, 725 (1998)

7 H. Li, X. Huang, L. Chen, Solid State Ionics 123, 189 (1999)

8 J. Wang, I. D. Raistrick, R. A. Huggins, J. Electrochem. Soc. 133, 457 (1986)

9 J. Wang, P. King, R. A. Huggins, Solid State Ionics 20, 185 (1986)

10 P. Poizot, S. Laruelle, S. Grugeon, L. Dupont, J. M. Tarascon, Nature 407, 496 (2000)

11 T. Brousse, R. Retoux, U. Herterich, D. M. Schleich, J. Electrochem. Soc. 145, 1 (1998)

12 S. Nam, Y. H. Kim, W. I. Cho, B. W. Cho, H. S. Chun, K. S. Yun, Electrochem. Solid State Lett. 2, 9 (1999)

13 R. Retoux, T. Brousse, D. M. Schleich, J. Electrochem. Soc. 146, 2472 (1999)

14 N. Li, C. R. Martin, B. Scrosati, Electrochem. Solid State Lett. 3, 316 (2000)

15 J. Zhu, Z. Lu, S. T. Aruna, D. Aubarch, A. Gedanken, Chem. Mater. 12, 2557 (2000)

16 M. T. Weller, *Inorganic Materials Chemistry*, Oxford Science Publications, Chemistry Primers, n°23 (1994)

17 R. De L. Kronig, Z. Phys. 70, 371 (1931)

18 E. A. Stern, Phys. Rev. B 10, 3027 (1974)

19 E. A. Stern, D. Sayers, F. W. Lytle, Phys. Rev. B 11, 4825 (1975)

20 E. A. Stern, D. Sayers, F. W. Lytle, Phys. Rev. B 11, 4836 (1975)

21 P. A. Lee, J.B. Pendry, 11, 2795 (1975)

22 J. Goulon, C. Goulon-Ginet, Pure & Appl. Chem. 54 (12), 2307 (1982)

23 N. Binsted, EXCURV98 (1998): CCLRC Daresbury Laboratory computer program

24 S. J. Gurman, N. Binsted, I. Ross, J. Phys. C. 17,143 (1984)

25 A. Manthiram, J. Kim, Chem. Mater. 10, 2895 (1998)

26 M. N. Obrovac, O. Mao, J. R. Dahn, Solid State Ionics 112, 9 (1998)

27 T. Hashemi, H. M. Al-Allak, J. Illingsworth, A.W. Brinkman, J. Woods, J. Mater. Science Lett. 9, 776 (1990)

28 I. S. Tambolova, K. Konstantinov, D. Kovacheva, P. Peshev, T. Donchev, J. Solid State Chem. 128, 305 (1997)

3 Electrochemical results

3.1 Super S Carbon

The Super S carbon was included in the electrode preparation to facilitate the electric conductivity through the electrode as described in chapter 2.1.1. The Super S carbon was tested electrochemically in order to quantify the capacity it provides during cycling. The Super S carbon was tested against Li metal between 0.02 and 1.5 V with two currents, 0.05 and 0.1 mA. The galvanostatic plots of Super S carbon for both currents are similar thus only the galvanostatic plot cycled with a current of 0.1 mA is shown Figure 3.1.

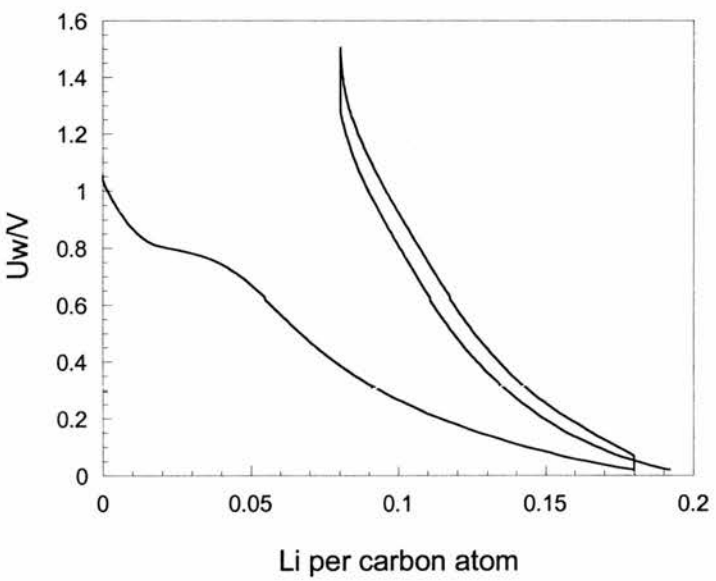

Figure 3.1: Galvanostatic plot of Super S carbon cycled between 0.02 and 1.5 V (0.1 mA)

One plateau is observable during the initial discharge around 0.8 V and corresponds approximately to 0.04 Li intercalated per carbon atom, then the voltage decreases gradually to 0.02 V. During the initial charge no plateau is observable, and about 50 % of the initial capacity is lost. The plateau present at 0.8 V during the initial discharge disappears during the second discharge. Capacities and Li inserted/de-inserted per carbon atom are summarised in Table 3.1. The theoretical capacity of carbon is 372 mAh/g.

	Li inserted per carbon atom	1st irreversible capacity, mAh/g	Li de-inserted per carbon atom	1st reversible capacity, mAh/g
0.05 mA	0.19	69	0.10	38
0.1 mA	0.18	67	0.10	37

Table 3.1: Initial experimental capacities and Li inserted/de-inserted per carbon atom

These numbers are quite small compared to the theoretical capacities of the materials investigated. As the proportion of carbon used in each electrode was also small, therefore Super S carbon will not affect significantly the absolute experimental capacity during electrochemical tests.

3.2 SnO_2 model

3.2.1 Results

SnO_2 was used to prepare most of the materials tested as negative electrodes and naturally was studied as a model to be compared with the oxides investigated. In this study no attempt was made to optimise the morphology of SnO_2 to improve the

cycling performance. The suggested mechanism[1] occurring during cycling described in chapter 1 for SnO_2 is written as followed:

Equation 3.1 $SnO_2 + 4Li^+ + 4e^- \rightarrow 2Li_2O + Sn$ *irreversible capacity*

Equation 3.2 $4.4Li^+ + Sn + 4.4e^- \leftrightarrow Li_{4.4}Sn$ *reversible capacity*

SnO_2 was tested in galvanostatic mode between 0.02 and 2 V with a current of 0.05 mA. The galvanostatic plot for the first 1.5 cycles is shown in Figure 3.2.

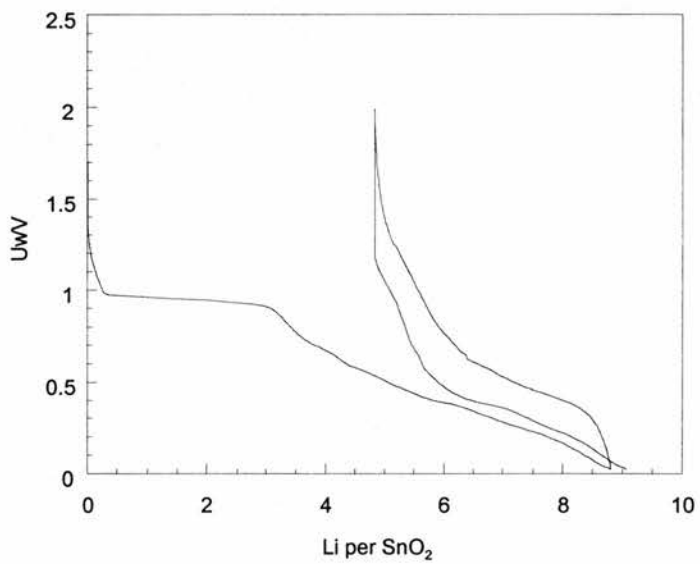

Figure 3.2: Galvanostatic plot of SnO_2 cycled between 0.02 and 2 V (0.05 mA)

During the initial discharge a large plateau and three small plateaus are observable at approximately 0.95 V, 0.7 V, 0.55 V and 0.4 V respectively. Around 0.4 V a plateau is observable during the initial charge and during the second discharge. On charge about 50 % of the initial capacity is lost. The plateau at about 0.95 V corresponds to the reduction of SnO_2 into Sn metal and the formation of the oxide framework Li_2O.

Experimentally around 3 Li/SnO_2 was necessary to reduce SnO_2 that is lower than the theoretical 4 Li/SnO_2 needed (Equation 3.1). The three small plateaux observed below 0.8 V during the initial discharge correspond to various Li-Sn alloys formation[2-3-4-5]. At the end of the initial discharge in total about 8.7 Li/SnO_2 were inserted, this number is similar to the theoretical value 8.4.

As suggested in the Equation 3.1, about 50 % of the initial capacity are lost due to the irreversible formation of Li_2O. During the charge process around 4 Li are de-inserted which is 91 % of the theoretical value, 4.4. The plateau observed approximately at 0.4 V for the initial charge and the 2nd discharge corresponds to reversible alloying of Sn metal[2] with Li.

Many works[1-6-7-8-9] were performed on SnO_2 material and our results are in agreement with these previous studies. SnO_2 is reduced into Sn metal and form irreversibly Li_2O, then Li are inserted reversibly into Sn metal.

The galvanostatic plot of SnO_2 showed in Figure 3.2 was differentiated and the derivative plot is represented Figure 3.3. Five cathodic and four anodic peaks are observed during the initial discharge and initial charge respectively. The cathodic peak at 0.95 V corresponds to the reduction of SnO_2 into Sn metal. The cathodic peaks at 0.69 V, 0.57 V, 0.39 V and 0.27 V correspond to the formation of $Li_{0.4}Sn$, $Li_{0.7}Sn$, $Li_{2.33}Sn$, $Li_{3.5}Sn$ respectively[2]. The anodic peaks at 0.42 V, 0.59 V and 0.67 V correspond to $Li_{3.5}Sn$, $Li_{2.33}Sn$, and $Li_{0.7}Sn$ formation. The anodic peak at 1.23 V that could not be identified implies the existence of an electrochemical reaction. This

reaction is not related to the destruction of Li-Sn alloys as the reversible Li insertion into Sn metal occurs below 0.8 V^2 at room temperature.

Two broad anodic peaks around 1.5 V and 2 V were observed by several authors but not discussed[1]. Recently however, Brousse *et al.* [10] reported a surprising result concerning these two peaks, when the SnO_2 electrode is charged up to 3 V. They claimed according to XRD results that these peaks is the result of the re-oxidation of Sn metal. Thus the anodic peak observed at 1.23 V Figure 3.3 could be related the re-oxidation of Sn metal. If the re-oxidation of Sn metal occurs that implies the partial destruction of Li_2O. SnO_2 does not follow the mechanism suggested, as it does not predict the electrochemical phenomena that occur above 1 V. This implies that a refinement of the suggested model for SnO_2 is needed.

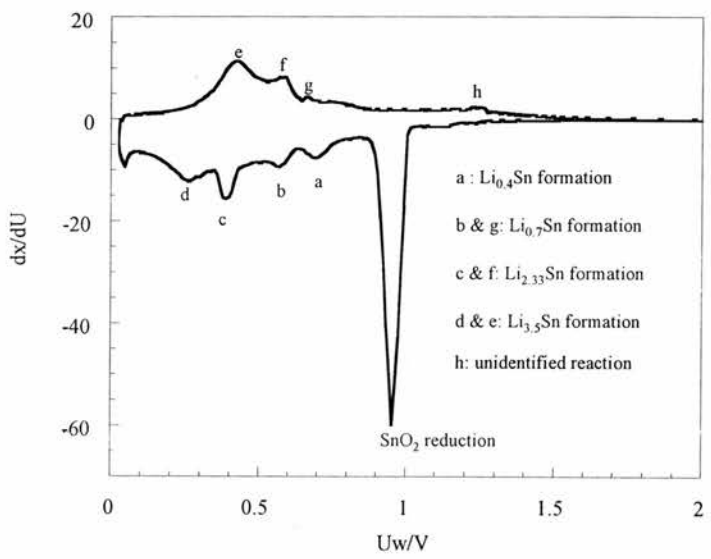

Figure 3.3: Derivative plot of SnO_2 cycled between 0.02 and 2 V

3.2.2 Cycling performance

The cycling performance of SnO_2 was studied on the basis of parameters used in a previous study[11]. SnO_2 was cycled with several window voltages (0.02-2V, 0.02-1V and 0.2-0.8V) in order to determine the best cycling performance. The best electrochemical response is obtained when SnO_2 is cycled in the range 0.2-0.8 V and the worst response for SnO_2 cycled up to 2V as shown in Figure 3.4. SnO_2 cycled up to 1 V and 2 V have the highest initial reversible capacity but the capacity drop is higher than SnO_2 cycled up to 0.8 V. About 40 % of the initial reversible capacity is lost at the 10^{th} cycle for SnO_2 above 0.8 V while SnO_2 cycled up to 0.8 V has only lost 10 % of its initial capacity. When the 25^{th} cycle is reached SnO_2 cycled up to 0.8 V, 1 V and 2 V has 76 %, 30 % and 15 % of the initial reversible capacity left. SnO_2 cycled between 0.2 and 0.8 V exhibits the best cycling performance.

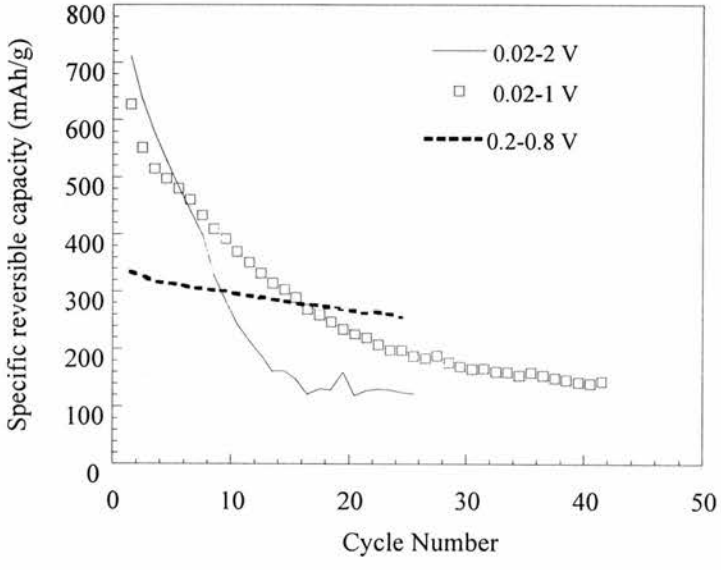

Figure 3.4: Cycling performance of SnO_2 (0.1 mA)

3.3 ZnO

3.3.1 Results

It has previously been reported that lithium-zinc alloys [12-13-14] can be formed electrochemically and indeed ZnO seems to follow a similar mechanism[1-15] to that proposed in chapter 1 for Tin-Based Oxides materials.

Equation 3.3 $ZnO + 2Li^+ + 2e^- \rightarrow Li_2O + Zn$ *irreversible capacity*

Equation 3.4 $1.5Li^+ + Zn + 1.5e^- \leftrightarrow Li_{1.5}Zn$ *reversible capacity*

ZnO was tested in galvanostatic mode (Figure 3.5) between 0.02 and 1.8 V with a current of 0.05 mA. The galvanostatic plot of ZnO Figure 3.5 has a large plateau at 0.60 V during the initial discharge, and three other small plateaus are observable at 0.22 V, 0.15 V and 0.10 V. During the initial charge three plateaus at 0.18 V, 0.52 V and 0.64 V, and during the second discharge two plateaus at 0.51 V and 0.23 V are observable. All these plateaux decrease gradually until the 5th cycle to disappear afterwards.

The large plateau observed during the initial discharge corresponds to the reduction of ZnO into Zn metal. Approximately 2.2 Li were needed to reduce ZnO, that is slightly over the theoretical value (Equation 3.3). The plateaus observed at 0.22 V, 0.15 V and 0.10 V during the initial discharge correspond to the formation of various Li-Zn alloys. The first two plateaux observed during the initial charge correspond to the formation of LiZn (0.18 V) and Li_2Zn_5 (0.52 V)[12]. During the initial discharge 3.4 Li/ZnO were inserted and 1.6 Li/ZnO were de-inserted during the initial charge.

These two values are similar to the theoretical values, 3.5 Li/ZnO and 1.5 Li/ZnO. On charge, more than half of the initial capacity is lost due to the formation of the matrix Li_2O according to Equation 3.3.

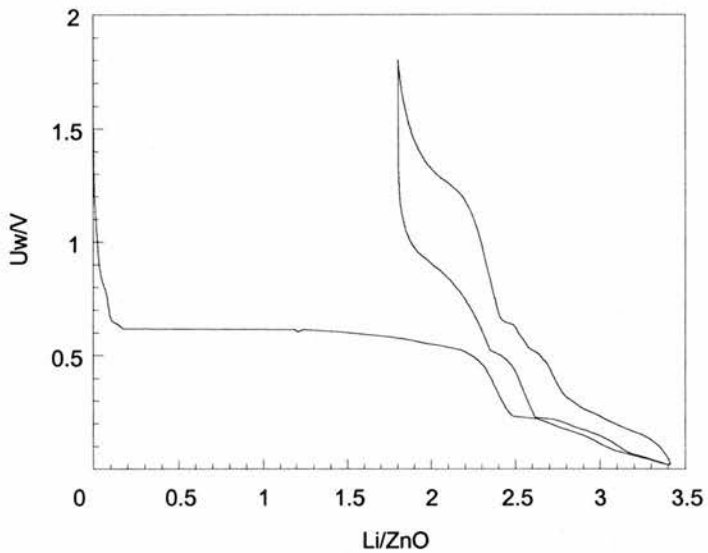

Figure 3.5: Galvanostatic plot of ZnO cycled between 0.02 and 1.8 V (0.05 mA)

ZnO was as well tested in potentiostatic mode between 0.02 and 2 V (Figure 3.6). Four cathodic peaks at 0.8 V, 0.5 V, 0.20 V and 0.14 V, and five anodic peaks at 0.18 V, 0.26 V, 0.53 V, 0.66 V and 1.25 V are observable. The cathodic peak at 0.5 V is the result of two peaks, which are overlapping. This cathodic peak corresponds to the reduction of ZnO and to the formation of Li_2Zn_5. Cathodic peaks at 0.20 V and 0.14 V correspond to the formation of Li_2Zn_3 and LiZn respectively[12]. The small cathodic peak at 0.8 V corresponds to the intercalation of Li into the Super S carbon used to prepare the electrode as seen in Figure 3.1 section 3.1. The anodic peak at 0.66 V that has not been identified was as well observed for Li-Zn alloys tested as negative electrodes[13-14]. The anodic peaks observed at 0.18 V, 0.26 V and 0.53 V correspond to

the formation of Li_2Zn_3, $LiZn_2$ and Li_2Zn_5 alloys respectively. All the peaks corresponding to the different Li-Zn alloys are present except for the highest Li-Zn alloy, $Li_{1.5}Zn$ that should be observed at 5mV[12]. Most publications have reported LiZn as the highest Li-Zn alloys[6-15-16]. But the formation of a higher Li-Zn alloy, $Li_{1.5}Zn$ has been reported[12] and the electrochemical tests (Figure 3.5) performed on ZnO agree as almost 3.5 Li/ZnO were inserted during the initial discharge.

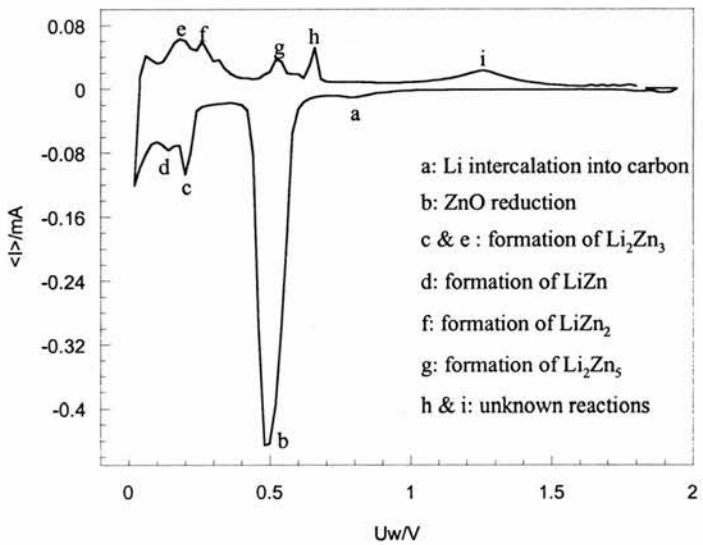

Figure 3.6: Potentiostatic plot of ZnO cycled between 0.02 and 1.8 V (20mV/h)

3.3.2 Cycling performance

According to the theoretical reversible capacity (496 mAh/g) ZnO might seem to be a good candidate[6] for Li-ion batteries, however the cycling performance is not as good as might be expected. ZnO was cycled between 0.1 V and 0.66 V, 0.1 V and 0.8 V, and finally 0.1 and 1.5 V and compared to each other in order to analyse the influence of these unknown electrochemical reactions on the cycling performance (Figure 3.7).

The percentage of the initial reversible capacity is plotted vs. cycle number. ZnO cycled up to 1.5 V has the worst capacity retention and ZnO cycled up 0.66 V has the best capacity retention. When cycling ZnO up to 1.5 V, the combination of both unidentified electrochemical reactions involved in the cycling process lower ZnO electrochemical performance. When the electrochemical process occurring at 1.25 V is removed the cycling performance improves slightly. The improvement of the cycling performance is higher when the upper cut off is 0.66 V; although cycling up to 0.66 V does not prevent the unknown electrochemical process. At the fifth cycle about 70 % of the initial reversible capacity is already lost when ZnO cycled up to 0.66 V while about 85 % of the initial reversible capacity is lost for ZnO cycled up to 1.5 V. There is little capacity left after the tenth cycle, and overall ZnO cycled very badly whatever the upper cut off voltage chosen.

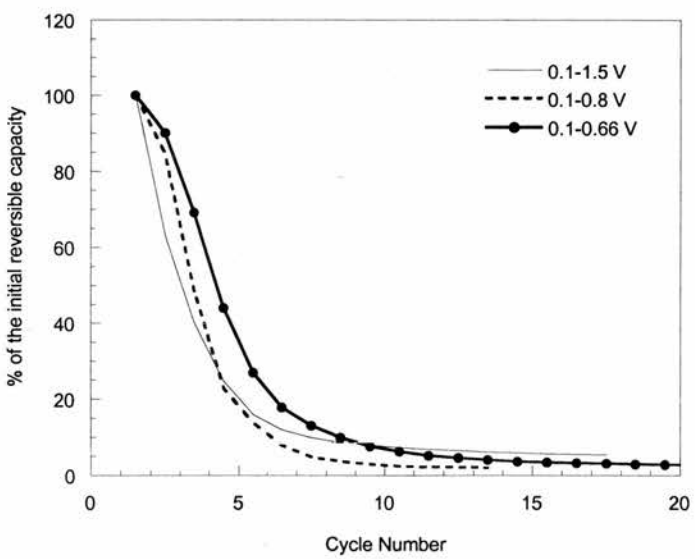

Figure 3.7: Comparison of the cycling performance of ZnO cycled between 0. 1 V and 1.5 V

The electrochemical tests were performed using three other window voltages than above in order to improve the cycling performance. Figure 3.8 displays the specific reversible capacity of ZnO cycled between 0.01 and 1.5 V, 0.01 and 0.5 V, 0.1 and 0.66 V, and 0.2 and 0.8 V is plotted vs. cycle number. ZnO cycled up to 1.5 V and cycled up to 0.8 V have the highest and the lowest initial specific reversible capacity respectively (Figure 3.8). The specific reversible capacity of ZnO cycled up to 1.5 V, although very promising fades so quickly that after 5 cycles approximately 90 % of the initial capacity is already lost. Fujieda *et al.* thought that discharging from Li_2Zn_5 (0.53 V) generates irreversible chemical reactions[13], thus ZnO was cycled between 0.01 and 0.5 V. The capacity loss is slower for the first three cycles but soon after the electrode degrades very quickly to finally have similar bad performance to ZnO cycled up to 1.5 V. ZnO cycled up to 0.5 V has better capacity retention than ZnO cycled up 0.66 V because the unidentified reaction occurring at 0.66 V is prevented. At the 5^{th} cycle less than 20 % of the initial reversible capacity of ZnO cycled between 0.2 and 0.8 V has been lost and when the 10^{th} cycle it remains 50 % of the initial reversible capacity. ZnO cycled between 0.2 and 0.8 V has the best cycling profile, although the reversible capacity at the 20^{th} cycle is only about 50 mAh/g.

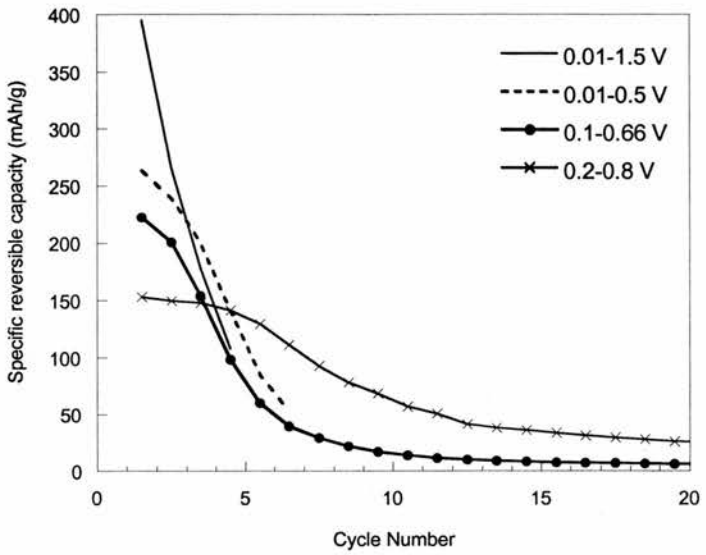

Figure 3.8: Specific reversible capacity (mAh/g) of ZnO vs. cycle number

3.3.3 Conclusion

It was shown that ZnO is reduced into Zn metal and irreversibly forms Li_2O, then Li is inserted reversibly into Zn metal. However ZnO does not follow the mechanism suggested for Tin-Based-Oxides as the plateau observed at 0.64 V in Figure 3.5 and the anodic peaks observed at 0.66 V and 1.25 V in Figure 3.6 reveal the presence of another electrochemical phenomena. During the initial charge when the potential 0.6 V is reached the last Li-Zn alloy, Li_2Zn_5 is completely destroyed to form Zn metal. Thus a re-oxidation of Zn metal at 0.66 V is possible as the reduction potential of ZnO occurs around 0.6 V. EXAFS studies on the ZnO electrode during charge have shown the re-oxidation of Zn metal above 0.6 V, more details are given in chapter 4.

The cycle life of an electrodeposited Zn electrode has improved by dispersing 2% of iron in the electrode composition. The advantage of using ZnO instead of Zn metal initially was to generate a matrix, Li_2O that is believed to moderate the effects of morphological changes occurring in alloy phases upon cycling[5-11] and thus improving the electrochemical performance. Nevertheless the ZnO-derived electrode still degrades upon cycling and exhibits poor cyclability. ZnO is definitely not a promising material to be used in Li-ion batteries as negative electrodes.

ZnO poor cyclability is due to the high crystallinity of Zn metal. *In-situ* XRD (more details are given in chapter 4) performed on ZnO electrode during the initial discharge down to 0.05 V reveals the presence of LiZn alloy. Whatever the window voltage chosen, Zn metal peaks are observable on the XRD pattern. ZnO is reduced into crystalline Zn metal and the consequence is the fast degradation of the electrode.

3.4 $ZnO:SnO_2$ systems

3.4.1 Overview

Initially it was thought that ZnO would show similar cycling behaviour to SnO_2 and hence that the combination might prove attractive. Unfortunately, ZnO displays poor cyclability, therefore SnO_2 was combined with ZnO to study the influence of ZnO on the electrochemical behaviour of the $ZnO:SnO_2$ systems. Both oxides were also ball-milled to provide fine particles. Several studies[17-5] have shown that small particle size significantly reduces the problems associated with volume expansion occurring during the reversible process of Li insertion into a metal. In addition small particle size should ease Li diffusion into and out of the material. Mixing SnO_2 and ZnO could allow an improvement in cyclability to be achieved by controlling the composite composition.

Batches of ZnO and SnO_2 were ball-milled together for different times to form the $ZnO:SnO_2$ systems with molar ratios 1:1, 2:1 and 1:2. Milling is known to be a useful technique, which apart from reducing the particle size may allow some unusual synthesis such as mechanical alloying[18]. It is difficult to envisage a mechanosynthesis between both these oxides due to the hardness[19] of SnO_2 (6.5 Mohs on a scale of 10). No new phases appear during milling of the mixtures, although the x-ray peaks become broader as the mixture becomes more amorphous. An example is shown for the mixture $ZnO:SnO_2$ (1:2) in Figure 3.9, peaks become broader with milling especially ZnO. ZnO is softer than SnO_2 with a hardness[19] of 4 Mohs therefore ZnO peak intensities decrease faster than SnO_2. From the XRD pattern the Debye-Scherrer

formula was used to estimate the particle size of ZnO and SnO_2 from the ZnO:SnO_2 systems; these are detailed separately later.

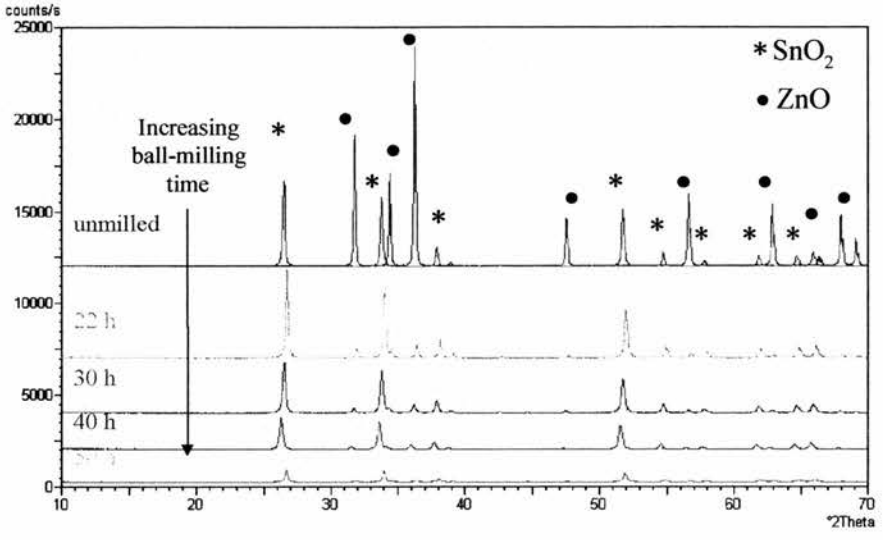

Figure 3.9: Powder x-ray diffraction data for ZnO:SnO_2 (1:2) exposed to different milling times

A disadvantage of ball-milling is that often contamination with zirconia (ZrO_2) may occur. In order to investigate if contamination with ZrO_2 had occurred during milling, X-ray fluorescence (XRF) were carried out on selected samples. Small amounts of yttria were added as an internal reference and different amounts of ZrO_2 were added, so as to back-calculate the amount of ZrO_2 contamination after ball-milling. From this, the contamination of the sample by the ZrO_2 balls was found to be around 0.07 %. Although little contamination had occurred, ZrO_2 was tested as a negative electrode following similar procedure described in Chapter 2.1. The electrochemical test showed that ZrO_2 is not reduced and the amount of Li inserted reversibly is accord with that expected for a cell containing only the carbon usually used to prepare the electrodes.

3.4.2 $ZnO:SnO_2$ (1:2)

The voltage curves of the $ZnO:SnO_2$ (1:2) systems cycled between 0.02 and 1.5 V with a current of 0.05 mA and exposed to several milling times are shown in Figure 3.10. During the initial discharge one large and two small plateaus are observable at 0.95 V, 0.6 V and 0.4 V respectively. Both small plateaus observed at 0.6 V and 0.4 V decrease gradually with milling. During the initial charge a semi-plateau is observed between 0.4 and 0.6 V. The plateau noticed at 0.95 V (~ 5 $Li/ZnO\text{-}2SnO_2$) during the initial discharge corresponds to the reduction of SnO_2 into Sn metal. The plateau at 0.6 V (~ 2 $Li/ZnO\text{-}2SnO_2$) corresponds to the reduction of ZnO into Zn metal. In the $ZnO:SnO_2$ (2:1) system the reduction of ZnO is complete as theoretically 2 $Li/ZnO\text{-}2SnO_2$ are needed but the reduction of SnO_2 is incomplete as in theory 8 $Li/ZnO\text{-}2SnO_2$ are necessary. It is expected that most of the Li insertion into Sn[12] and Zn[2] metals occurs after the reduction of ZnO below 0.7 V. Thus the reduction of SnO_2 which is incomplete at the end of the plateau at 0.95 V, probably continues below 0.95 V. The small plateau noticed at 0.4 V during the initial discharge and charge correspond to Li-Sn formation[2].

The initial experimental Li inserted and de-inserted per $ZnO:SnO_2$ (1:2) unit and capacities of $ZnO:SnO_2$ (1:2) cycled between 0.02 and 1.5 V with a current of 0.05 mA are summarised in Table 3.2. Initial irreversible capacity increases until 40 hours milling times then decreases while the initial reversible capacity upon milling time is inconsistent. The initial reversible capacity decreases until 22 hours then rises up to 40 hours and finally decreases again at 50 hours. However overall, 40 hours of ball-

milling displays the best initial capacities in this system. At 40 hours ball-milling the number of Li inserted per metal is similar to the theoretical value, 20.3 whereas the number of Li de-inserted is approximately 23% less than the expected value 10.3. After 40 hours of ball-milling, milling appears to be pointless as there is no initial capacity improvement.

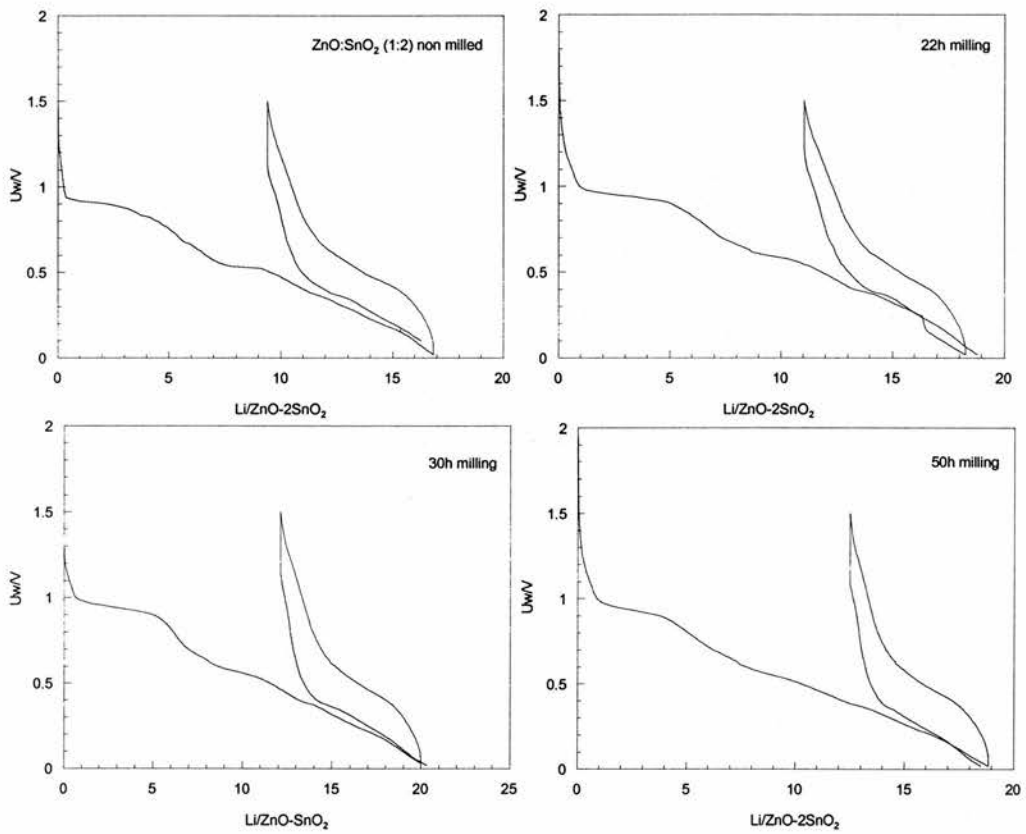

Figure 3.10: Galvanostatic plots for the 1st 1.5 cycles of $ZnO:SnO_2$ (1:2) cycled between 0.02 and 1.5 V (0.05 mA) exposed to different milling times, voltage is plotted vs. $Li/ZnO\text{-}2SnO_2$

	Li inserted per $ZnO:2SnO_2$ unit	1st irreversible capacity (mAh/g)	Li de-inserted $ZnO:2SnO_2$ unit	1st reversible capacity (mAh/g)
Non-milled	16.84	1175	7.45	519
22h milling	18.28	1275	7.25	505
40 h milling	20.00	1395	7.89	550
50h milling	18.84	1314	6.35	443

Table 3.2: Initial experimental capacities and number of Li/ZnO-$2SnO_2$ unit inserted/de-inserted vs. milling time for $ZnO:SnO_2$ (1:2) mixture

The cycling behaviour of the $ZnO:SnO_2$ (1:2) system cycling between 0.02 and 1 V with a current of 0.05 mA and exposed to a range of milling times upon cycling were studied and results are shown in Figure 3.11. There is a significant difference between milled samples and the non-milled sample. The non-milled sample gives the worst profile. Samples milled for 40 and 50 hours that have identical profile retain capacity better than the non-milled and 22 hour milled samples display the best cycling performance. Thus over 40 hours milling it is unnecessary to continue the milling process in order to improve the cycling performance $ZnO:SnO_2$ (1:2) system because the optimum milling time is already reached.

The cycling performance of each sample correlates perfectly with the crystallite size of each oxide in the mixture $ZnO:SnO_2$ (2:1) as shown in Table 3.3. The ZnO and SnO_2 starting materials have similar crystallite size, which decreases up to 40 hours milling time. Thus there is no need to ball-mill the oxides for more than 40 hours because the particles have reached an optimum size where it is impossible to reduce

the particle size further. Nevertheless, milling both oxides improves the cycle life of the electrode with the reduction of particle size.

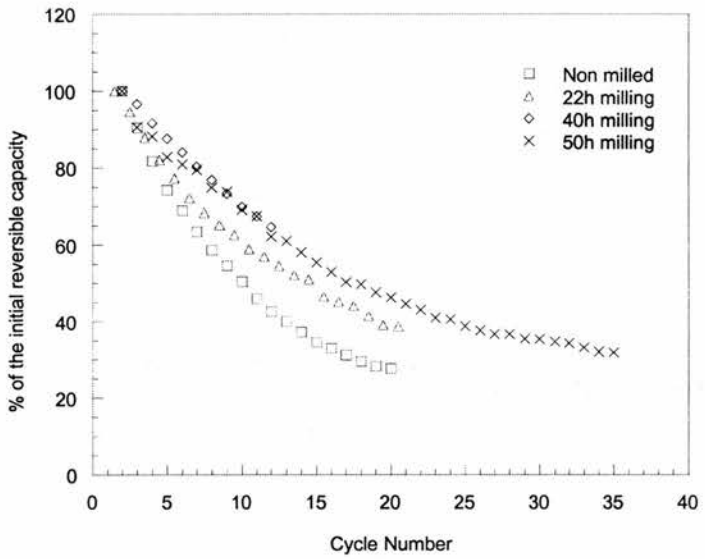

Figure 3.11: Percentage of the initial reversible capacity vs. cycle number of ZnO:SnO_2 (1:2) cycled between 0.01 and 1 V (0.05 mA)

Milling time of ZnO:SnO_2 (1:2)	Crystallite size ± 10 nm	
	ZnO	SnO_2
non-milled	**1000-5000**	**1000-5000**
22 hours	**56**	**50**
40 hours	**34**	**33**
50 hours	**36**	**41**

Table 3.3: Dependence of particle size of ZnO and SnO_2 in the ZnO:SnO_2 (1:2) system upon milling time

Despite the best cycling performance observed for ZnO:SnO_2 (1:2) milled for 40 and 50 hours, the capacity drop per cycle is critical. At the 5^{th} cycle the electrode has

already lost 20 % of its initial capacity and by the time the 20th cycle is reached only 50 % of the capacity remains which makes this mixture not promising as an anode material for Li-ion cells.

3.4.3 $ZnO:SnO_2$ (1:1)

The voltage profiles of $ZnO:SnO_2$ (1:1) cycled after different milling times are shown in Figure 3.12. The samples were tested between 0.02 and 1.5 V with a current of 0.05 mA. Three plateaus are observable at 0.95 V, 0.6 V and 0.4V during the initial discharge. A plateau around 0.4 V is observed during the initial charge. The size of the plateau at 0.95 V does not change upon milling time. Plateaus at 0.6 V and at 0.4 V decrease gradually with milling time. Plateaus at 0.95 V (~ 3Li/ZnO-SnO_2) and 0.6 V (~ 2Li/ZnO-SnO_2) correspond to the reduction of SnO_2 into Sn metal and ZnO into Zn metal respectively. The reduction of SnO_2 is incomplete as in theory 4 Li/ZnO-SnO_2 are needed for a complete reduction; ZnO reduction on the other hand is complete. It is possible that the reduction of SnO_2 continues below the reduction plateau at 0.95 V as most of the Li insertion into Sn metal occurs below 0.7 V at room temperature[2]. The plateau observed at 0.4 V during the initial discharge and charge corresponds to the formation of Li-Sn alloys[2].

The initial experimental capacities and Li inserted/de-inserted per $ZnO:SnO_2$ (1:1) unit for the $ZnO:SnO_2$ (1:1) systems cycled between 0.02 and 1.5 V at 0.05 mA are summarised in Table 3.4. Two groups can be distinguished for the initial irreversible capacities, non-milled and 10 hour milled samples, and 20 and 30 hour milled

samples. The initial reversible capacity for each milling time is different, the lowest initial reversible capacity is given by the sample milled for 20 hours and the highest initial reversible capacity by the sample milled for 30 hours. Overall Li inserted/de-inserted per $ZnO:SnO_2$ (1:1) unit decreases evenly until 20 hours of milling but at 30 hours milling Li inserted/de-inserted per $ZnO:SnO_2$ (1:1) unit increases.

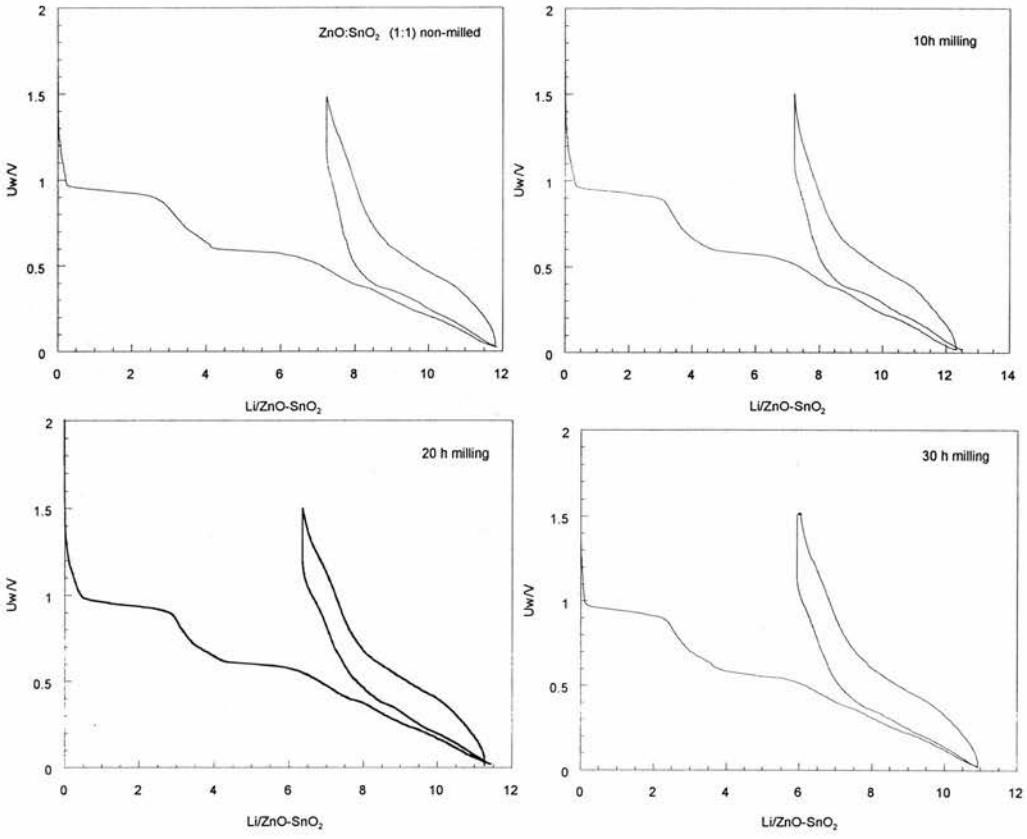

Figure 3.12: Galvanostatic plots for the 1st 1.5 cycles of $ZnO:SnO_2$ (1:1) cycled between 0.02 and 1.5 V (0.05 mA) exposed to different milling times, voltage is plotted vs. $Li/ZnO\text{-}SnO_2$

	Li inserted per $ZnO:SnO_2$ unit	1st irreversible capacity (mAh/g)	Li de-inserted per $ZnO:SnO_2$ unit	1st reversible capacity (mAh/g)
Non-milled	11.81	1361	4.58	529
10h milling	11.73	1352	4.25	491
20h milling	10.89	1256	4.15	479
30h milling	10.92	1259	4.88	563

Table 3.4 Initial experimental capacities and number of Li/ZnO-SnO_2 unit inserted/de-inserted vs. milling time for $ZnO:SnO_2$ (1:1) cycled between 0.02 and 1.5 V (0.05 mA).

The cyclability of the $ZnO:SnO_2$ (1:1) cycled between 0.02 and 1 V (0.05 mA) was analysed and the result is displayed in Figure 3.13. All samples should have the same theoretical reversible capacity. However as seen previously Table 3.4, the initial reversible capacity is different for each milling time. The highest initial reversible capacity is given by the sample milled 20 hours and the lowest by the sample milled 30 hours. Until the 5th cycle all samples exposed to different milling times exhibit similar capacity drop, approximately 20 % of the initial capacity is already lost. Thereafter the cycling performance of each sample has a distinct behaviour. The sample milled for 30 hours has the worst performance profile and the non-milled sample the best cycling performance; cycling performance of samples milled 20 and 30 hours are quite similar. All samples in the $ZnO:SnO_2$ (1:1) system show rapid capacity loss. Nevertheless the non-milled sample has the best cycling performance though only 50 % of the initial reversible capacity (~ 260 mAh/g) remains at the 15th cycle. Milling the oxides reduces the electrochemical performance of the battery in the $ZnO:SnO_2$ (1:1) system.

The crystallite size of ZnO and SnO_2 within the ZnO:SnO_2 (1:1) system is shown in Table 3.5. The particle size of ZnO and SnO_2 decreases gradually and similarly with milling time. The particle size of ZnO is similar to the particle size of SnO_2 for samples milled 20 and 30 hours. The electrochemical performance of the samples in the ZnO:SnO_2 (1:1) system did not improve with milling although the crystallite size of ZnO and SnO_2 decreased. Thus for this ratio milling ZnO and SnO_2 shortens the cycle life of the battery despite the reduction of the particle size.

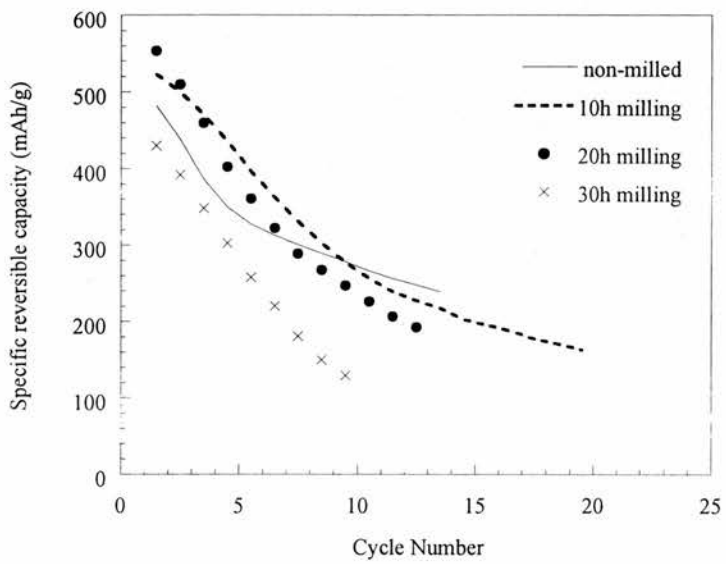

Figure 3.13: Specific reversible capacity vs. cycle number for ZnO:SnO_2 (1:1) cycled between 0.01 and 1 V (0.05 mA)

Milling time of $ZnO:SnO_2$ (1:1)	Crystallite size ± 10 nm	
	ZnO	SnO_2
Non-milled	**1-5 μm**	**1-5 μm**
10 hours	**51**	**60**
20 hours	**52**	**55**
30 hours	**42**	**43**

Table 3.5: Dependence of particle size of ZnO and SnO_2 in the $ZnO:SnO_2$ (1:1) system upon milling time

3.4.4 $ZnO:SnO_2$ (2:1)

The voltage profile of the $ZnO:SnO_2$ (2:1) systems cycled between 0.02 and 1.5 V with a current of 0.05 mA are displayed in Figure 3.14. Two large plateaus approximately at 0.95 V (~ 3 Li/Sn) and 0.6 V (~ 4 Li/Zn), and two small plateaus at 0.4 V and 0.2 V are observable in the mixture during the initial discharge. The plateaus at 0.95 V (~ 3 Li/Sn) and 0.6 V (~ 4 Li/Zn) correspond to the reduction of SnO_2 and ZnO respectively. In the $ZnO:SnO_2$ (2:1) system the reduction of ZnO is complete as theoretically 4 Li are needed but the reduction of SnO_2 is incomplete as in theory 4 more Li are also needed. It is expected that most of the Li insertion into Sn[2] and Zn[12] metals occurs after the reduction of ZnO below 0.7 V. Thus the reduction of SnO_2 that is incomplete at the end of the plateau at 0.95 V, presumably continues until 0.7 V. The small plateau observed around 0.4 V corresponds to Li-Sn alloys formation[2]. The other small plateau observed during the initial discharge at 0.2 V corresponds to the formation of Li-Zn alloys[12].

Initial experimental capacities for the $ZnO:SnO_2$ (2:1) system are shown in Table 3.6. During the initial discharge the non-milled sample and the oxides milled separately samples in the $ZnO:SnO_2$ (2:1) system have relatively similar irreversible capacities. The highest irreversible capacity is given by the co-milled sample. Overall the experimental initial irreversible capacity for all samples in this system is very similar to the theoretical value 1316 mAh/g. The non-milled sample has slightly lower initial reversible capacity. The initial reversible capacity of the non-milled sample is 35 % less than the theoretical value 633 mAh/g while the milled samples represents 92 % of the theoretical value. Milling separately or co-milling the oxides equally improve the initial reversible capacity in the $ZnO:SnO_2$ (2:1) system.

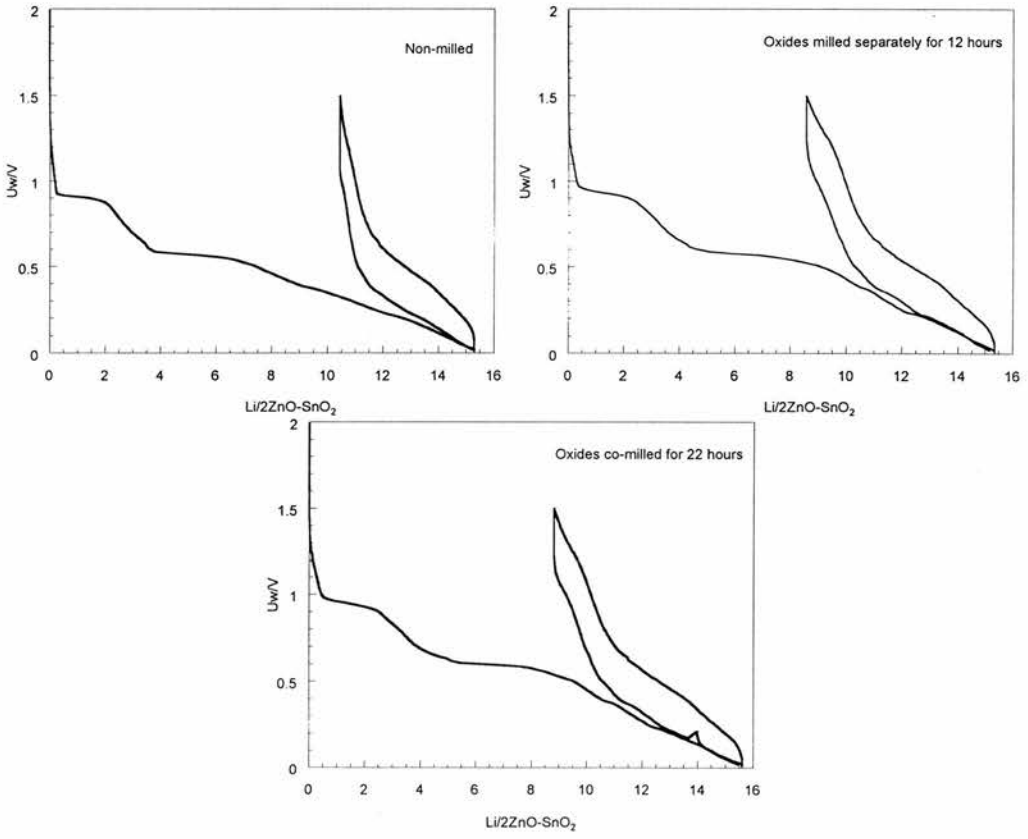

Figure 3.14: Galvanostatic plots for the 1.5 first cycles of $ZnO:SnO_2$ (2:1) cycled between 0.02 and 1.5 V (0.05 mA)

	Li inserted per $2ZnO:SnO_2$ unit	1st irreversible capacity (mAh/g)	Li de-inserted per $2ZnO:SnO_2$ unit	1st reversible capacity (mAh/g)
$2ZnO+SnO_2$ non-milled	15.30	1307	4.87	417
$2ZnO+SnO_2$ milled separately 12 hours	15.36	1313	6.8	582
$2ZnO+SnO_2$ 22 hours milling	15.60	1333	6.8	582

Table 3.6: Initial experimental capacities and Li/$2ZnO:SnO_2$ unit inserted/de-inserted in the $ZnO:SnO_2$ (2:1) mixture

The capacity retention upon cycling of the samples from the $ZnO:SnO_2$ (2:1) system cycled between 0.2 and 0.8 V with a current of 0.1 mA is shown in Figure 3.15. Milling separately and co-milling ZnO and SnO_2 give the same electrochemical performance. The non-milled sample has the worst electrochemical performance whereas the milled samples display the best electrochemical performance. The difference between the non-milled sample and the milled samples is very significant for this $ZnO:SnO_2$ (2:1) ratio. The milled samples have lost less than 40 % of the initial reversible capacity at the 15th cycle while the non-milled sample has already lost more than 80 % of the initial reversible capacity. In this case milling the oxides gives better capacity retention upon cycling, but milling separately or together the two oxides does not affect the electrochemical performance of the electrode.

The particle size of ZnO and SnO_2 in the $ZnO:SnO_2$ (2:1) system is shown Table 3.7. When ZnO is co-milled with SnO_2 its particle size is bigger compared to ZnO milled

alone. The particle size of SnO_2 for the sample where both oxides are co-milled is smaller than sample where SnO_2 is milled alone. Overall the particle size of ZnO and SnO_2 decrease upon milling. Co-milling and milling separately both oxides show similar capacity retention although the particle size for each oxide in each sample is different. In the ZnO:SnO_2 (2:1) system the electrochemical performance of the electrode improves with the decrease of the particle size.

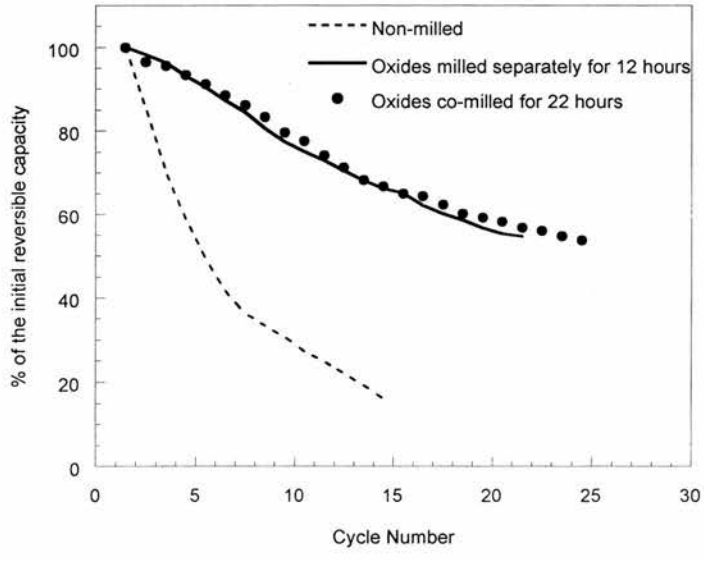

Figure 3.15: Percentage of the initial reversible capacity of ZnO:SnO_2 (2:1) tested between 0.2-0.8 V (0.1mA) vs. cycle number

Milling time	Crystallite size ± 10 nm	
ZnO:SnO_2 (2:1)	ZnO	SnO_2
Non-milled	**1000-5000**	**1000-5000**
12 hours separately	**35**	**59**
20 hours together	**51**	**49**

Table 3.7: Crystallite size of ZnO and SnO_2 in the ZnO:SnO_2 (2:1) system upon milling time

3.4.5 Conclusion

In the $ZnO:SnO_2$ system whatever the ratio used each oxide behaves independently electrochemically. SnO_2 is reduced first into Sn metal at 0.95 V then ZnO is reduced into Zn metal at 0.6 V. Two plateaus corresponding to the formation of Li-Sn alloys and Li-Zn alloys were visible on the galvanostatic plots during the initial discharge. Most of the Li insertion into Sn and Zn metal seems to occur after the reduction of ZnO localised at 0.6 V[2-12]. Milled samples show improved capacity retention only for the systems $ZnO:SnO_2$ (1:2) and $ZnO:SnO_2$ (2:1). Thus the benefit of the particle size reduction depends on the ratio of ZnO and SnO_2 present in the mixture.

The percentage of the initial reversible capacity of the best sample of each series from the $ZnO:SnO_2$ system is plotted vs. cycle number in Figure 3.16. The samples were cycled with a current of 0.1 mA within the optimised cycling range of voltage, 0.2-0.8 V found for SnO_2 and ZnO to allow the comparison with them. The $ZnO:SnO_2$ (1:2) sample milled 50 hours and the $ZnO:SnO_2$ (1:1) non milled sample have similar capacity retention. But the sample with high SnO_2 contents exhibits slightly better capacity retention compared to the sample with high ZnO contents until the 35^{th} cycle. Thereafter sample with high concentration of ZnO displays better capacity retention. But overall all the samples in the $ZnO:SnO_2$ mixtures have a poor capacity retention. These samples have only approximately 50% of the initial reversible capacity left after 35 cycles. Overall the difference between the three samples is very small.

The electrochemical performance of the $ZnO:SnO_2$ (1:1) mixture is not affected by the milling process whereas the electrochemical performance of $ZnO:SnO_2$ (1:2) and the $ZnO:SnO_2$ (2:1) mixtures have improved upon milling. After only 12 hours milling, the mixture with high contents of ZnO shows an improvement of the capacity retention. The mixture with high contents of SnO_2 on the other hand needs 50 hours milling to exhibit an improved capacity retention. It was expected to obtain after milling an improvement of the capacity retention for all mixtures and not only for the mixture $ZnO:SnO_2$ (1:2) and $ZnO:SnO_2$ (2:1). In the $ZnO:SnO_2$ (1:1) mixture milling decreases the capacity retention.

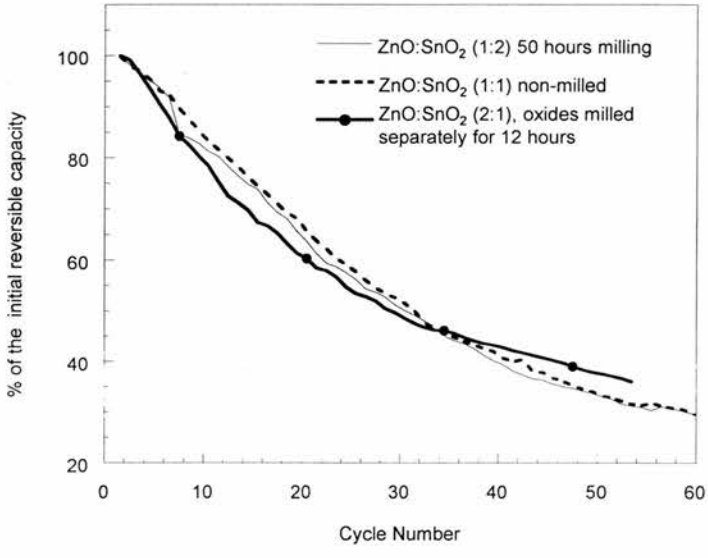

Figure 3.16: Percentage of the initial reversible capacity of $ZnO:SnO_2$ (1:2) ball-milled 12h, $ZnO:SnO_2$ (1:1) non-milled, $ZnO:SnO_2$ (2:1) ball-milled 12h separately cycled between 0.2 and 0.8 V (0.1 mA) vs. cycle number

The specific reversible capacity of $ZnO:SnO_2$ (1:2) ball-milled 50 hours, $ZnO:SnO_2$ (1:1) non-milled, $ZnO:SnO_2$ (1:2) where the oxides were ball-milled 12 hours separately are also compared to SnO_2 and ZnO Figure 3.17. ZnO has the lowest initial reversible capacity, and SnO_2 and $ZnO:SnO_2$ (1:2) the highest reversible capacity. SnO_2 and $ZnO:SnO_2$ (1:2) have similar reversible capacity during the first 7 cycles, thereafter SnO_2 exhibits better reversible capacity. The reversible capacities of the $ZnO:SnO_2$ mixtures are lower than for SnO_2 but higher than ZnO. For the $ZnO:SnO_2$ mixture, the samples with the larger concentration of SnO_2 have larger reversible capacity. ZnO reversible capacity remains almost constant until the 5^{th} cycle, then the capacity drops very quickly. At the 25^{th} cycle ZnO has almost no capacity left, the $ZnO:SnO_2$ mixtures have lost around 40 % of their initial reversible capacities and SnO_2 has only lost 20 % of its initial reversible capacity. ZnO exhibits the fastest capacity fade while SnO_2 has the slowest.

SnO_2 remains the most promising anode material for rechargeable Li-ion batteries. Poor cyclability of ZnO due to the high tendency of Zn metal to crystallise affects considerably the electrochemical behaviour of the samples from $ZnO:SnO_2$ mixtures. *Ex-situ* XRD performed on $ZnO:SnO_2$ show that both Zn and Sn metal are crystalline. The poor electrochemical performance is surprising because the shape of the galvanostatic plots of the $ZnO:SnO_2$ mixtures is dominated by SnO_2.

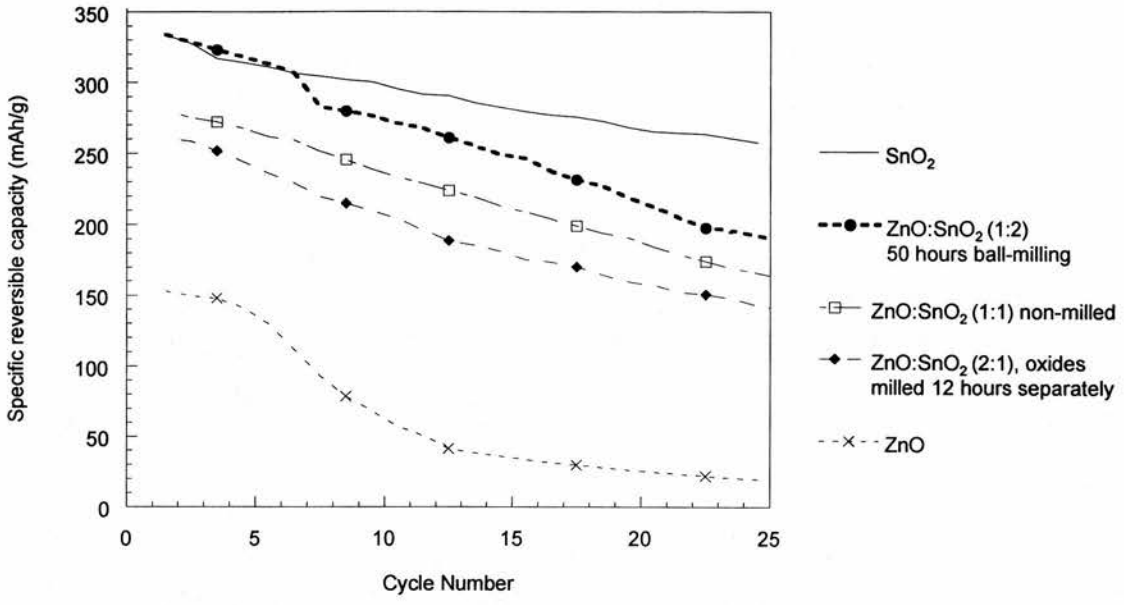

Figure 3.17: Comparison of the specific reversible capacity of $ZnO:SnO_2$ (1:2) ball-milled 12h, $ZnO:SnO_2$ (1:1) non-milled, $ZnO:SnO_2$ (2:1) ball-milled 12h separately, SnO_2 and ZnO cycled between 0.2 and 0.8 V (0.1 mA) vs. cycle number

3.5 Zn_2SnO_4

3.5.1 Particle size

The inverse spinel, Zn_2SnO_4 was prepared in two different ways by either ball-milling or hand-grinding together stoichiometric amounts of ZnO and SnO_2. The resulting powders were respectively fired at 1000 °C for 16 hours and 1100 °C for 24 hours to form Zn_2SnO_4 (1000 °C) and Zn_2SnO_4 (1100 °C). If the resulting powder obtained from hand-grinding is fired at 1100 °C for more than 24 hours, the spinel structure is partially destroyed. X-ray diffraction performed on this sample shows peaks corresponding to the spinel and SnO_2 but there was no sign of ZnO. Similar results were observed when the spinel prepared at 1100 °C was fired above this temperature. Thus when the spinel is destroyed, ZnO tends to evaporate. Therefore to reduce this tendency, ZnO and SnO_2 were ball-milled together to lower the synthesis temperature of Zn_2SnO_4. Zn_2SnO_4 synthesised at 1000 °C and then fired for more 16 hours is not destroyed after more than 72 hours at this temperature.

SEM was performed on both Zn_2SnO_4 samples to study the morphology and estimate the particle size of each Zn_2SnO_4 sample (Figure 3.18). SEM images show clearly that ball-milling ZnO and SnO_2 prior firing at 1000 °C gives smaller particle size than hand-grinding before firing at 1100 °C. The synthesis temperature plays an important role in determining particle size. The benefit of small particle size obtained after ball-milling is kept when combined with low temperature synthesis.

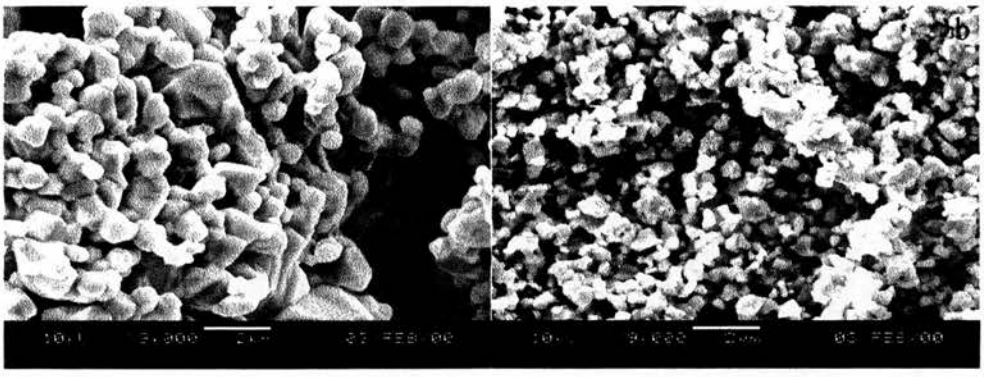

Figure 3.18: SEM of a) Zn_2SnO_4 (1000 °C) b) Zn_2SnO_4 (1100 °C)

In complement to the SEM images, the particle size of Zn_2SnO_4 was measured using a Coulter LS particle analyser which gives an accurate distribution of the particle size. Three regions can be distinguished in the particle size distribution showed in Figure 3.19: region 1 (0-10 μm), region 2 (10-100 μm) and region 3 (> 100 μm). The particle size of Zn_2SnO_4 observed in region 3 did not decrease when milling ZnO and SnO_2 before sintering. Ball-milling affects only the particle size (<100 μm) of the spinel in regions 1 and 2. In the case of Zn_2SnO_4 (1100 °C), 25 % and 10 % of the particle size are smaller than 27 and 9 μm respectively. Zn_2SnO_4 (1000 °C) have 25 % and 10 % of the particle size smaller than 19 and 2 μm respectively. The observations made in particle size distribution confirm that the small particles are more representative for Zn_2SnO_4 (1000 °C) than Zn_2SnO_4 (1100 °C) as seen in Figure 3.18.

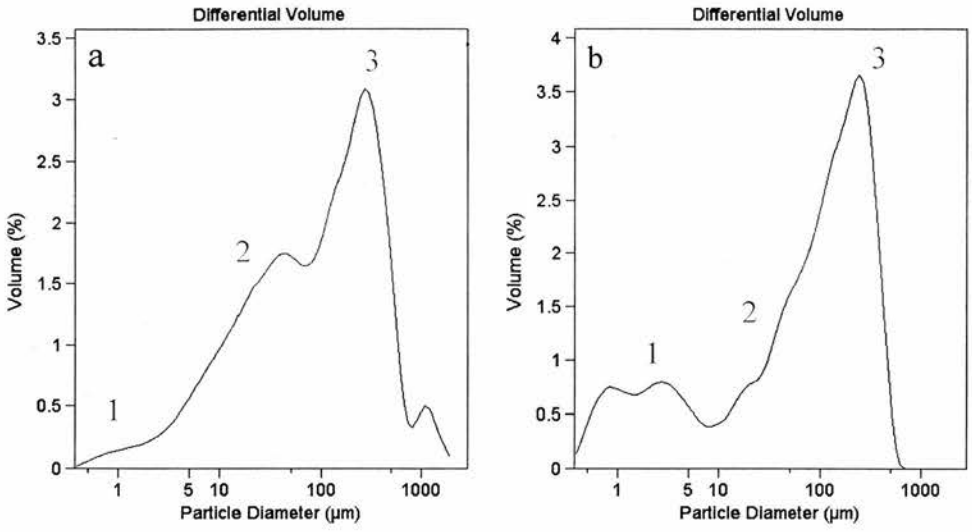

Figure 3.19: Particle size distribution of a) Zn_2SnO_4 (1100 °C) b) Zn_2SnO_4 (1000 °C)

3.5.2 Electrochemical results

In the preceding sections the electrochemistry of $ZnO:SnO_2$ mixtures was discussed. In this section the electrochemical behaviour of the compound Zn_2SnO_4 inverse spinel is discussed. According to the mechanism proposed for tin oxides, Zn_2SnO_4 should be reduced into tin and zinc metal in a framework of Li_2O. Li then is inserted reversibly into tin and zinc to form Li-Sn and Li-Zn alloys respectively. The expected mechanism can be expressed by the following equations:

Equation 3.5 $Zn_2SnO_4 + 8Li^+ + 8e^- \rightarrow 4Li_2O + 2Zn + Sn$ *irreversible capacity*

Equation 3.6 $2Zn + Sn + 7.4Li^+ + 7.4e^- \leftrightarrow 2Li_{1.5}Zn + Li_{4.4}Sn$ *reversible capacity*

In the earlier sections however it was demonstrated that SnO_2 and ZnO do not follow the above model. Thus it is expected that the spinel will not follow this model either. The first cycle of the galvanostatic plots of Zn_2SnO_4 (1000 °C) tested between 0.02 and 1.5 V with a current of 0.1 mA is shown in Figure 3.20. The galvanostatic plot of Zn_2SnO_4 (1100 °C) is not displayed because the voltage profile is similar to Zn_2SnO_4 (1000 °C). A large plateau around 0.5 V is observed for both Zn_2SnO_4 samples during the initial discharge. This plateau corresponds to the reduction of spinel into tin and zinc metals and the formation of Li_2O. This plateau is very close to the ZnO reduction plateau at 0.6 V (Figure 3.5) and much lower than the SnO_2 reduction plateau near 0.9 V (Figure 3.2).

The reduction of Zn_2SnO_4 shows two surprising features. Zn_2SnO_4 has only one plateau corresponding to the reduction of Sn^{4+} and Zn^{2+} whereas the ZnO:SnO_2 mixtures have two plateaus for similar reductions. Moreover, the potential of reduction was expected between 0.6 and 0.9 V and not at 0.5 V. This characteristic is presumably related to the lattice energy. 11807 and 4142 kJ/mol that are the calculated lattice energies for SnO_2 and ZnO respectively[20]. The lattice energy of the spinel would therefore expected to be slightly lower than that of ZnO. The reduction of SnO_2 leads to two moles of Li_2O (Equation 3.7), the reduction of ZnO to one mole of Li_2O (Equation 3.8) and the reduction of Zn_2SnO_4 to four moles of Li_2O (Equation 3.9). The energy required to form Li_2O depending on each oxide can be estimated. The lattice energy of Li_2O is 2799 kJ/mol. The energy of formation of Li_2O is summarised Table 3.8. The energy required to form Li_2O from SnO_2 is twice that of ZnO, and consequently the reduction potential of SnO_2 is higher. The enthalpy of

formation of Zn_2SnO_4 is certainly higher than the enthalpy of formation of SnO_2 plus ZnO. Thus the reaction enthalpy of the reduction of Zn_2SnO_4 is much higher than SnO_2 and ZnO. More bond distances to break.For Zn_2SnO_4 the energy needed to form Li_2O is twice the energy needed for SnO_2 and four times for ZnO, but the reduction potential is much lower than SnO_2 and closer to ZnO. On electrochemical Li insertion the reduction potential of Zn_2SnO_4 has shifted to lower potential. The reduction of spinel does not follow classic electrochemistry law.

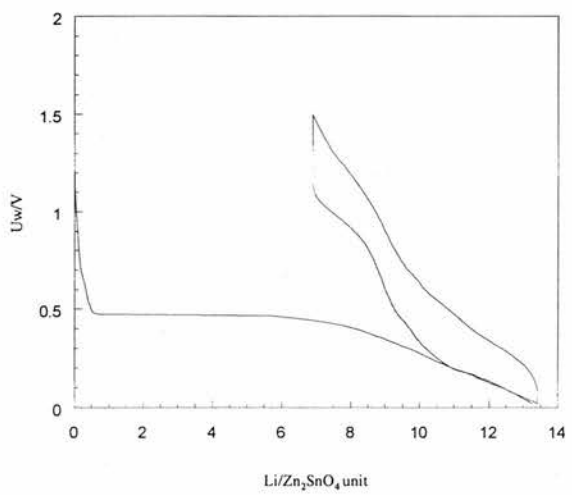

Figure 3.20: Galvanostatic plot for the 1st 1.5 cycle of Zn_2SnO_4 (1000 °C) cycled between 0.02 and 1.5 V (0.1mA)

Equation 3.7: $SnO_2 + 4Li^+ + 4e^- \rightarrow Sn + 2Li_2O$

Equation 3.8: $ZnO + 2Li^+ + 2e^- \rightarrow Zn + Li_2O$

Equation 3.9: $Zn_2SnO_4 + 8Li^+ + 8e^- \rightarrow Sn + 2Zn + 4Li_2O$

Material	ΔH_1 formation of Li_2O (kJ/mol)	ΔH_2 formation of the oxide[21] (kJ/mol)	$\Delta H_3 = \Delta H_1 - \Delta H_2$ (kJ/mol)	Reduction potential (V)
SnO_2	- 1196	- 580.8	- 1811.2	0.9
ZnO	- 598	- 350.5	- 247.5	0.6
Zn_2SnO_4	- 2392	- 931.3	- 1460.7	0.5

Table 3.8: ΔH formation for the oxides

In order to understand which phenomenon occurs below the reduction potential of Zn_2SnO_4 the galvanostatic plot of Zn_2SnO_4 (1000 °C) Figure 3.20 was differentiated (Figure 3.21). Three cathodic peaks at 0.20 V and 0.12 V, and four anodic peaks at 0.31 V, 0.55 V, 0.66 V and 1.25 V are observed. The anodic peak at 0.5 V corresponds to the reduction of Zn_2SnO_4. The cathodic peaks observed at 0.20 V and 0.12 V correspond respectively to Li_2Zn_3 and LiZn respectively[12]. The anodic peaks at 0.31 V, 0.55 V and 0.66 V can not be attributed to a specific Li-Sn alloys or Li-Zn alloys formation because it is impossible to discriminate between them. Thus below the reduction potential of Zn_2SnO_4 observed in Figure 3.20, Li is inserted reversibly into Zn and Sn metals. The anodic peak at 1.25 V has not been identified. This peak is similar to the one observed on the SnO_2 derivative plot Figure 3.3 and ZnO potentiostatic plot (Figure 3.6).

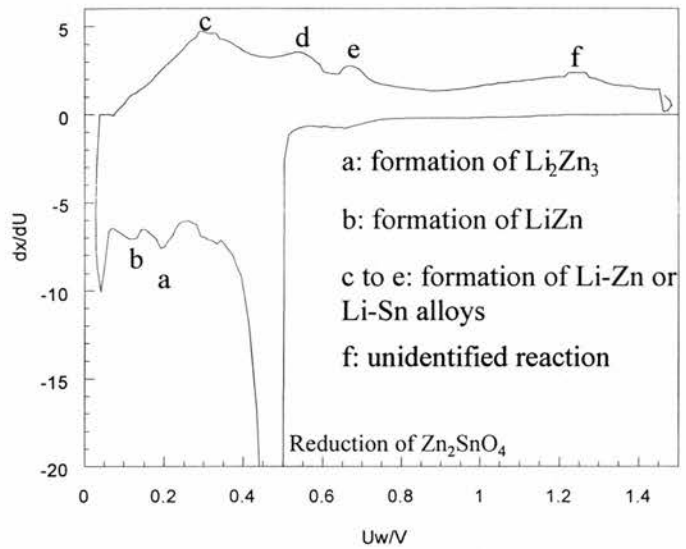

Figure 3.21: 1st cycle of the derivative plot of Zn_2SnO_4 (1000 °C)

Zn_2SnO_4 was cycled between several ranges of window voltages, 0.01-0.8, 0.2-1.5 V and 0.2-0.8 V in order to find the optimal window voltage. In Figure 3.22 the specific reversible capacity of Zn_2SnO_4 (1000 °C) cycled over the previous window voltages is plotted vs. cycle number. The highest initial reversible capacity is given by Zn_2SnO_4 (1000 °C) cycled between 0.2 and 1.5 V and the lowest by Zn_2SnO_4 (1000 °C) cycled between 0.2 and 0.8 V. Zn_2SnO_4 (1000 °C) cycled between 0.2 and 1.5 V and Zn_2SnO_4 (1000 °C) cycled between 0.01 and 0.8 V have similar capacity drop, although Zn_2SnO_4 (1000 °C) cycled between 0.2 and 1.5 V exhibits slightly better capacity retention after the 25th cycle. Zn_2SnO_4 (1000 °C) cycled between 0.2 and 0.8 V exhibits the best capacity retention. At the 20th cycle, Zn_2SnO_4 (1000 °C) cycled between 0.2 and 1.5 V, and Zn_2SnO_4 (1000 °C) cycled between 0.01 and 0.8 V have lost 60 % and 50 % of the initial reversible capacity respectively. When both samples have reached the 50th cycle, more than 80 % of the initial reversible capacity is lost.

Zn_2SnO_4 (1000 °C) cycled between 0.2 and 0.8 V retains the capacity much better, at the 50th cycle less than 20 % of the initial capacity is lost. Thus the optimised window voltage found for Zn_2SnO_4 (1000 °C) is between 0.2 and 0.8 V. Similar results were observed for Zn_2SnO_4 (1100 °C).

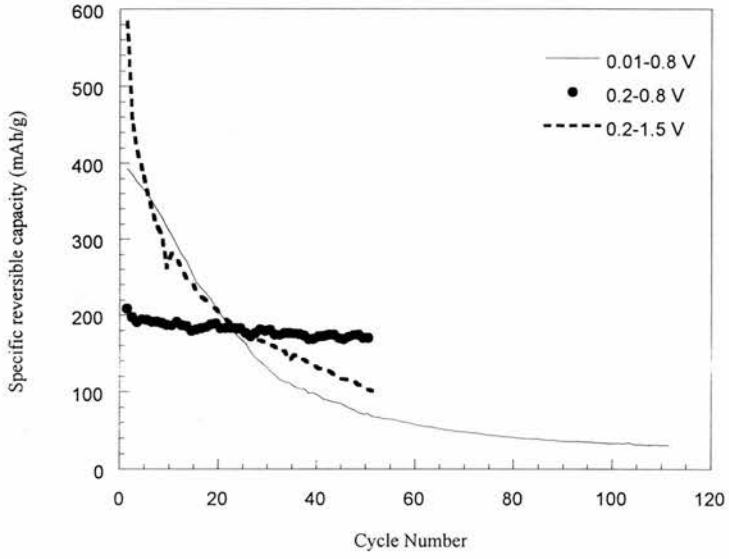

Figure 3.22: Specific reversible capacity of Zn_2SnO_4 (1000 °C) vs. cycle number

The cycling performance of Zn_2SnO_4 degrades when cycling below 0.2 V and above 0.8 V. Electrochemical studies have shown that reversible Li insertion into Sn and Zn metal occurs below 0.8 V[2-12]. Thus the reversible capacity observed above 0.8 V in Figure 3.20 and Figure 3.21 is not provided by the Li-Sn or Li-Zn alloys. Thus Zn_2SnO_4 (1000 °C) was initially discharged down to 0.02 V and then cycled between 0.8 and 2 V. The 1st reversible capacity observed between 0.8 and 2 V is about 85 mAh/g, which is much higher than the 1st reversible capacity provided by Super S carbon present (37 mAh/g). This reversible capacity is probably related to the same electrochemical phenomena occurring around 1.23 V for SnO_2 and ZnO.

Ex-situ XRD measurements were performed on the three spinel electrodes showed in Figure 3.22 at the end of the charge (more details are given in chapter 4). Zn_2SnO_4 cycled between 0.2 and 0.8 V and Zn_2SnO_4 cycled between 0.01 and 0.8 V have similar XRD patterns, no crystalline Sn and Zn metals are observable. However Zn_2SnO_4 cycled up to 1.5 V reveals the presence of crystalline Zn metal and crystalline Sn metal after 50 cycles. The high crystallinity of the metals is responsible for the bad electrochemical performance of Zn_2SnO_4 cycled between 0.2 and 1.5 V but this is not the case for Zn_2SnO_4 cycled between 0.01 and 0.8 V. Discharging Zn_2SnO_4 below 0.2 V lowers the electrochemical performance of the electrode probably because the lower cut off voltage is too close to the Li electrochemical potential. In addition the number of Li inserted into Sn and Zn metal is higher for Zn_2SnO_4 cycled until 0.01 V than Zn_2SnO_4 cycled until 0.2 V. Therefore Zn_2SnO_4 cycled down to 0.2 V formed less different Li-Sn and Li-Zn alloys and consequently Sn and Zn metals face less volume changes during the reversible alloying formation. Thus the electrode is more stable and retains capacity better upon cycling. The combination of amorphous metals resulting from the reduction of Zn_2SnO_4, and the reduction of the number of Li-Sn and Li-Zn alloys formed upon cycling improve considerably the cycling performance of Zn_2SnO_4.

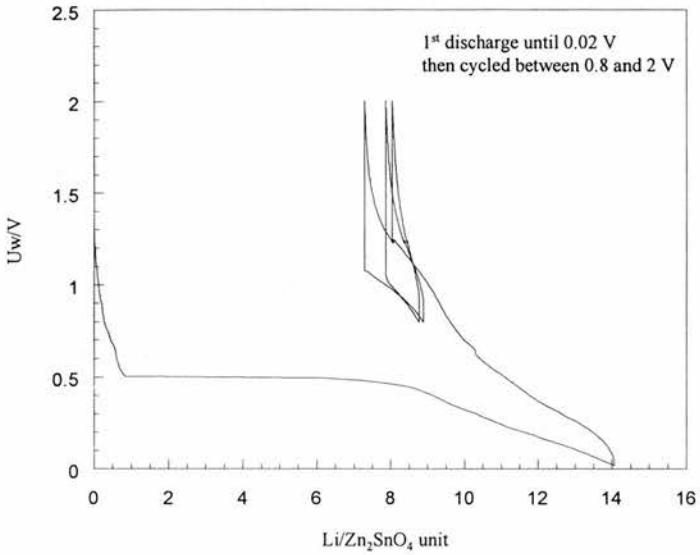

Figure 3.23: Galvanostatic plot of Zn_2SnO_4 (1000 °C) initially discharged down to 0.02V, then cycled between 0.8 and 2 V with a current of 0.1 mA

The cycling performance of both spinel compounds was studied and compared in order to determine which of the spinel compounds retain capacity better upon cycling. Both spinel compounds were then cycled with a current of 0.1 mA within the optimised window voltage, 0.2-0.8 V and the comparison between the two spinel samples is shown in Figure 3.24. The specific reversible capacity is plotted vs. the cycle number. Although Zn_2SnO_4 (1100 °C) exhibits the highest initial reversible capacity, upon cycling Zn_2SnO_4 (1000 °C) shows better capacity retention. At the 10^{th} cycle both spinel compounds have approximately similar reversible capacity around 190 mAh/g, although Zn_2SnO_4 (1100 °C) has lost about 18 % of the initial reversible capacity whereas Zn_2SnO_4 (1000 °C) has only lost 10 % of the initial reversible capacity. At the 50^{th} cycle however Zn_2SnO_4 (1000 °C) has just lost 20 % of the initial reversible capacity while 60 % of the initial reversible capacity remains for Zn_2SnO_4

(1100 °C). This observation is in good accord with the particle size observations described in section 3.4.1.

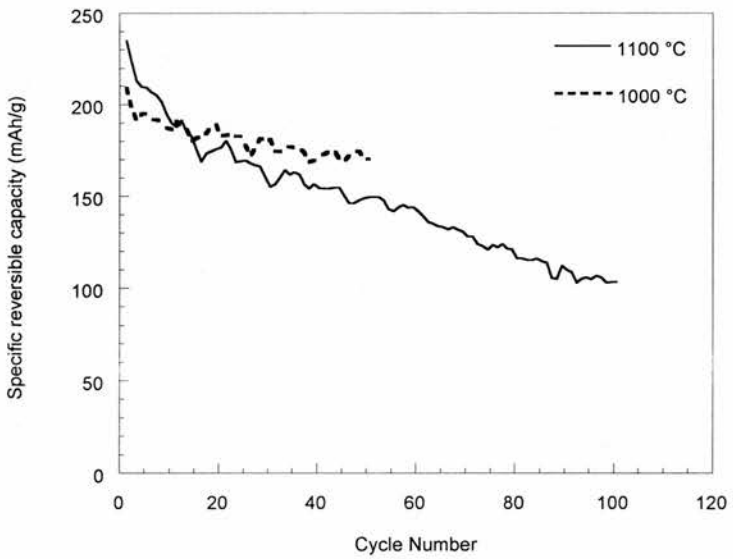

Figure 3.24: Specific reversible capacity of Zn_2SnO_4 cycled between 0.2 and 0.8 V

It is believed that small particles better absorb the volume expansion[5] occurring during the reversible Li alloying formation. Therefore Zn_2SnO_4 (1000 °C) which has a smaller particle compared to Zn_2SnO_4 (1100 °C) retains capacity much better upon cycling. Ball-milling the precursors before reaction at 1000 °C certainly provides a more homogeneous spinel material compared to the spinel where the precursors were hand-ground.

The crystallinity of both spinel samples cycled between 0.2 and 0.8 V, shown in Figure 3.24, was studied. *Ex-situ* XRD were performed on the electrodes at the end of the charge (0.8 V) and the pattern is shown Figure 3.25. The residual peak of Zn_2SnO_4 and the Cu grid peak used as an internal standard are present for both Zn_2SnO_4

electrodes. The residual peak of Zn_2SnO_4 proves that the reduction of the spinel is incomplete. On the XRD pattern there is no sign of Sn or Zn metals, which means they are not crystalline. Zn_2SnO_4 (1100 °C) was cycled twice more than Zn_2SnO_4 (1000 °C) but on the XRD pattern there is no significant difference between the samples. Thus the good electrochemical performance of Zn_2SnO_4 (1000 °C) compared to Zn_2SnO_4 (1100 °C) is not related to crystallinity but to the small particles. More details on the crystallinity of the spinel are given in chapter 4.

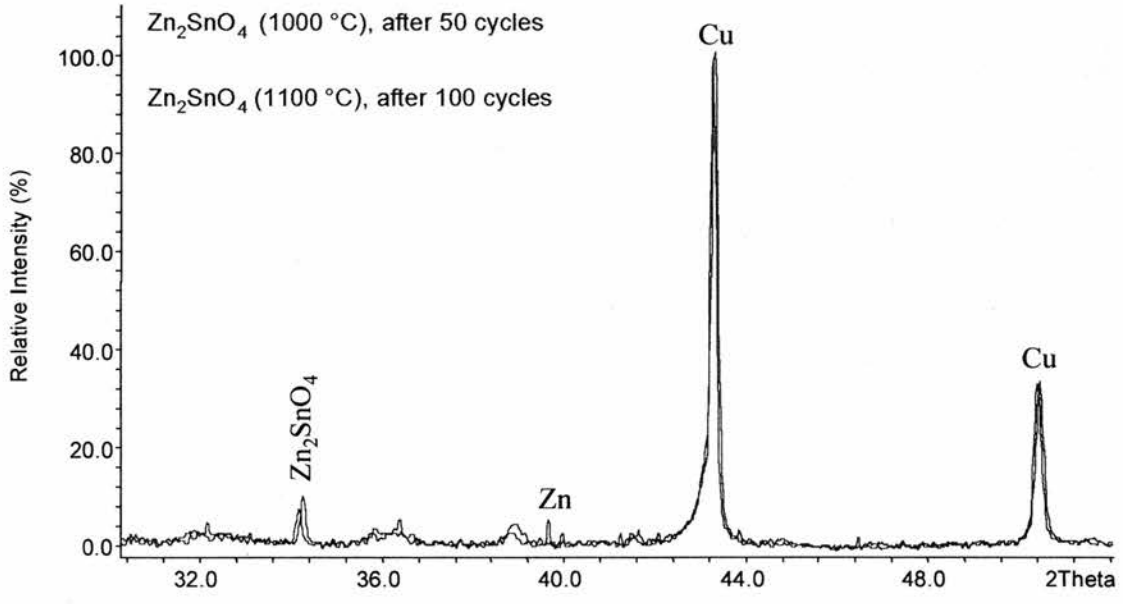

Figure 3.25: Ex-situ XRD performed on Zn_2SnO_4 cycled between 0.2 and 0.8 V with a current of 0.1 mA

3.5.3 Electrochemical comparison of Zn_2SnO_4 and $ZnO:SnO_2$ (2:1)

In the $ZnO:SnO_2$ (2:1) mixtures, each oxide behaves electrochemically independently towards Li metal, during the initial discharge two plateaux are observable for the reduction of SnO_2 and ZnO. In contrast, Zn_2SnO_4 has only one plateau corresponding to the simultaneous reduction of Sn^{4+} and Zn^{2+}. In theory Zn_2SnO_4 and $ZnO:SnO_2$ (2:1) should have exactly the same initial reversible capacities. Only the sample exhibiting the best cycling performance for the Zn_2SnO_4 and the $ZnO:SnO_2$ (2:1) mixture are considered. Thus the cyclability of Zn_2SnO_4 (1000 °C) was compared to the $ZnO:SnO_2$ (2:1) mixture, ZnO and SnO_2 milled separately for 12 hours (Figure 3.26). Upon cycling the capacity of the $ZnO:SnO_2$ (2:1) system fades so quickly that at the 20^{th} cycle approximately 55 % of the initial reversible capacity is lost while 90 % of Zn_2SnO_4 capacity remains. According to electrochemical studies, ZnO exhibits poor cyclability so it certainly affects the cycling performance of the $ZnO:SnO_2$ (2:1) system despite the presence of SnO_2. Nevertheless Zn_2SnO_4 displays satisfactory electrochemical performance compared to the $ZnO:SnO_2$ (2:1) system suggesting the zinc effects are being masked by the spinel starting structure.

The cycling performance of Zn_2SnO_4 (1000 °C), SnO_2 and ZnO were compared to each other in Figure 3.27, the specific reversible capacity is plotted vs. the cycle number. The oxides were cycled between 0.2 and 0.8 V with a current of 0.1 mA. SnO_2 has the highest initial reversible capacity and ZnO the lowest. Zn_2SnO_4 (1000 °C) exhibits the best cycling performance even if its initial reversible capacity is less than SnO_2. At the 25^{th} cycle Zn_2SnO_4 (1000 °C) has lost less than 15 % of its initial

reversible capacity whereas ZnO and SnO_2 have lost more than 85 % and 20 % of their initial reversible capacity respectively. The poor cyclability of ZnO seems to have no influence on the electrochemical performance of Zn_2SnO_4 (1000 °C). However, when the shape of Zn_2SnO_4 profile was compared to that of ZnO, it appears that the spinel seems to show features reminiscent of ZnO whilst its capacity retention is definitely dominated by the tin content.

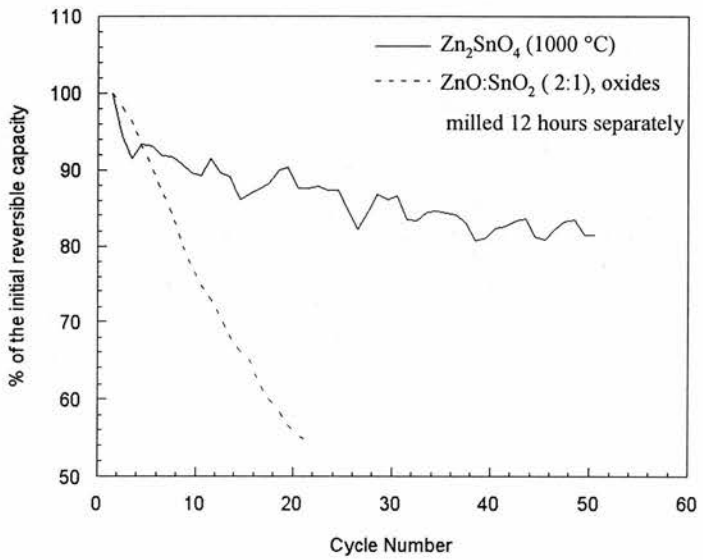

Figure 3.26: Comparison between the capacity retention of Zn_2SnO_4 (1000 °C) and ZnO:SnO_2 (2:1), oxides milled 12 hours separately cycled between 0.2 and 0.8 V with a current of 0.1 mA

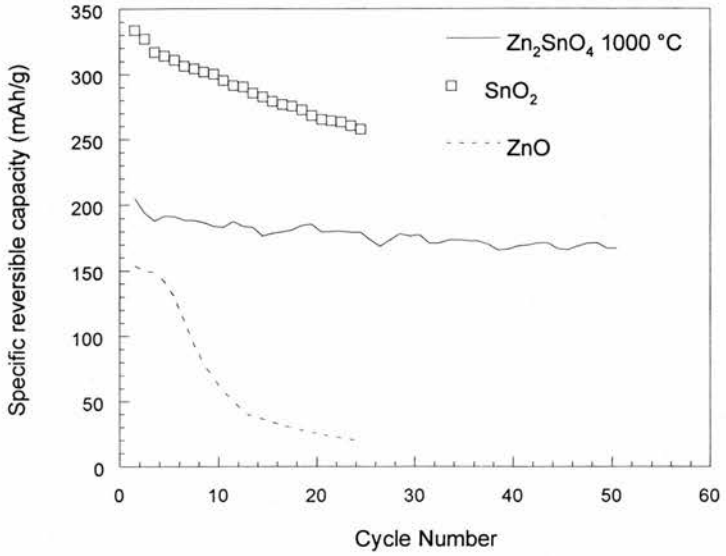

Figure 3.27: Specific reversible capacity of Zn_2SnO_4 (1000 °C), SnO_2 and ZnO cycled between 0.2 and 0.8 V with a current of 0.1 mA vs. cycle number

3.5.4 Conclusion

Zn_2SnO_4 is reduced during the initial discharge into Sn and Zn metals then Li inserts reversibly into Sn and Zn metal to form various Li-Sn and Li-alloys respectively. Above 0.8 V during charge the presence an unknown electrochemical process has been shown. The resulting compound consumed reversibly Li. Thus Zn_2SnO_4 does not exactly follow the model suggested for Tin-based-Oxides materials.

Two factors controlled the electrochemical performance of Zn_2SnO_4, crystallinity of the metals and the lower cut off voltage used to cycle the electrode. Zn_2SnO_4 cycled below 0.8 V show no sign of crystalline Sn or Zn metals in contrast with Zn_2SnO_4 cycled above 0.8 V. Having the cut off voltage at 0.2 V instead of 0.01 V improves the cycling performance because the electroplating of Li is minimised. In addition the

number of different Li alloys formed upon cycling is reduced therefore the volume changes occurring during alloying and de-alloying decreases.

Zn_2SnO_4 synthesised at 1000 °C exhibits better electrochemical performance than Zn_2SnO_4 synthesised at 1100 °C, because Zn_2SnO_4 (1000 °C) has smaller particles. The reduction of Zn_2SnO_4 (1000 °C) leads probably to small particle of Sn and Zn metals which are believed to better absorb the volume expansion occurring during the reversible insertion of Li into a metal. The properties of the starting material before its electrochemical reduction are a determining factor for the cyclability.

3.6 Li_2SnO_3

3.6.1 Electrochemical results

Li_2SnO_3 materials prepared at two different temperatures, 650 °C (LT) and 1000 °C (HT) were tested as possible Li-ion battery negative electrodes. Courtney *et al.*[1] have previously studied Li_2SnO_3 synthesised at 1000°C and have suggested an equation which might explain the mechanism occurring during discharge and charge:

Equation 3.10 $8.4\ Li + Li_2SnO_3 \rightarrow 3Li_2O + Li_{4.4}Sn \leftrightarrow 3Li_2O + 4.4Li + Sn$

Li_2SnO_3-LT and Li_2SnO_3-HT tested in galvanostatic mode have similar profiles, so for clarity only the galvanostatic plot of Li_2SnO_3-LT is shown in Figure 3.28. Li_2SnO_3-LT displays near 0.36 V and 0.18 V small and large plateaus respectively. The large plateau at about 0.18 V corresponds to the reduction of Li_2SnO_3 into Sn metal and to the formation of Li_2O. The plateau observed around 0.36 V during the initial discharge resembles a Li-Sn alloy plateau[2]. However this is quite unlikely, because this latter plateau appears before and not after the reduction of Li_2SnO_3.

On the initial charge about 50 % of the initial capacity is lost as predicted by the Equation 3.10. During charging, two plateaus are observable at about 0.4 and 1.3 V and they are still noticeable during the second discharge at approximately 0.4 and 1 V respectively. Plateaus around 0.4 V correspond to the reversible insertion of Li into Sn metal. Above 0.8 V no Li can be inserted reversibly into metallic tin[2] so the plateaus

at about 1 V during the second discharge and 1.3 V on initial charge reveal the presence of another compound that probably reversibly inserts Li.

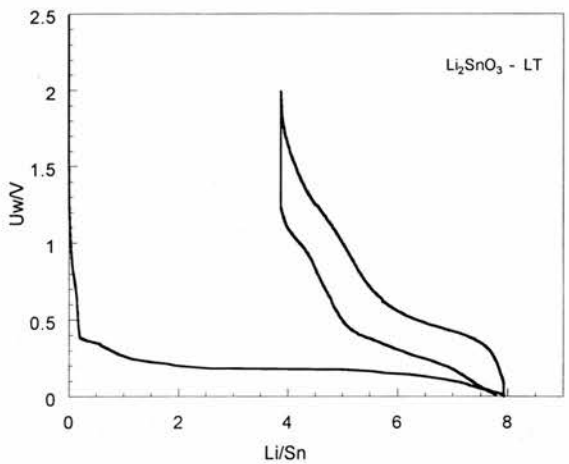

Figure 3.28: Galvanostatic plot for the 1st 1.5 cycles of Li_2SnO_3-LT cycled between 0.02 and 2 V (0.05 mA)

The galvanostatic plot of Li_2SnO_3-LT (Figure 3.28) was differentiated in order to extract more information on what is occurring during the initial cycle. The derivative plot of Li_2SnO_3-LT is shown Figure 3.29. Four cathodic peaks at 0.36 V, 0.19 V, 0.17 V and 0.13 V; and two anodic peaks at 0.43 V and 1.23 V are observable. The anodic peak at 0.19 V corresponds to the reduction of Li_2SnO_3 and the two anodic peaks at 0.13 V and 0.17 V correspond to the formation of Li-Sn alloys. These two phenomena are so close to each other that a single plateau at about 0.18 V is observed for both phenomena during the initial discharge on the galvanostatic plot (Figure 3.28). The anodic peak at 0.43 V corresponds to the formation of Li-Sn alloys[2]. The anodic peak at 1.23 V and the cathodic peak at 0.36 V are unidentified although the peak at 1.23 V

is similar to the one observed for SnO_2 (Figure 3.3), ZnO (Figure 3.6) and Zn_2SnO_4 (Figure 3.21).

Li_2SnO_3 is reduced into Sn metal and form Li_2O, and then Li reversibly inserts into the Sn metal. During the initial discharge and the initial charge two unknown phenomena occur respectively at 0.36 V and 1.23 V; thus Li_2SnO_3 does not follow the suggested model (Equation 3.10). This observation is similar to those made for SnO_2, ZnO and Zn_2SnO_4 in the previous sections of this chapter.

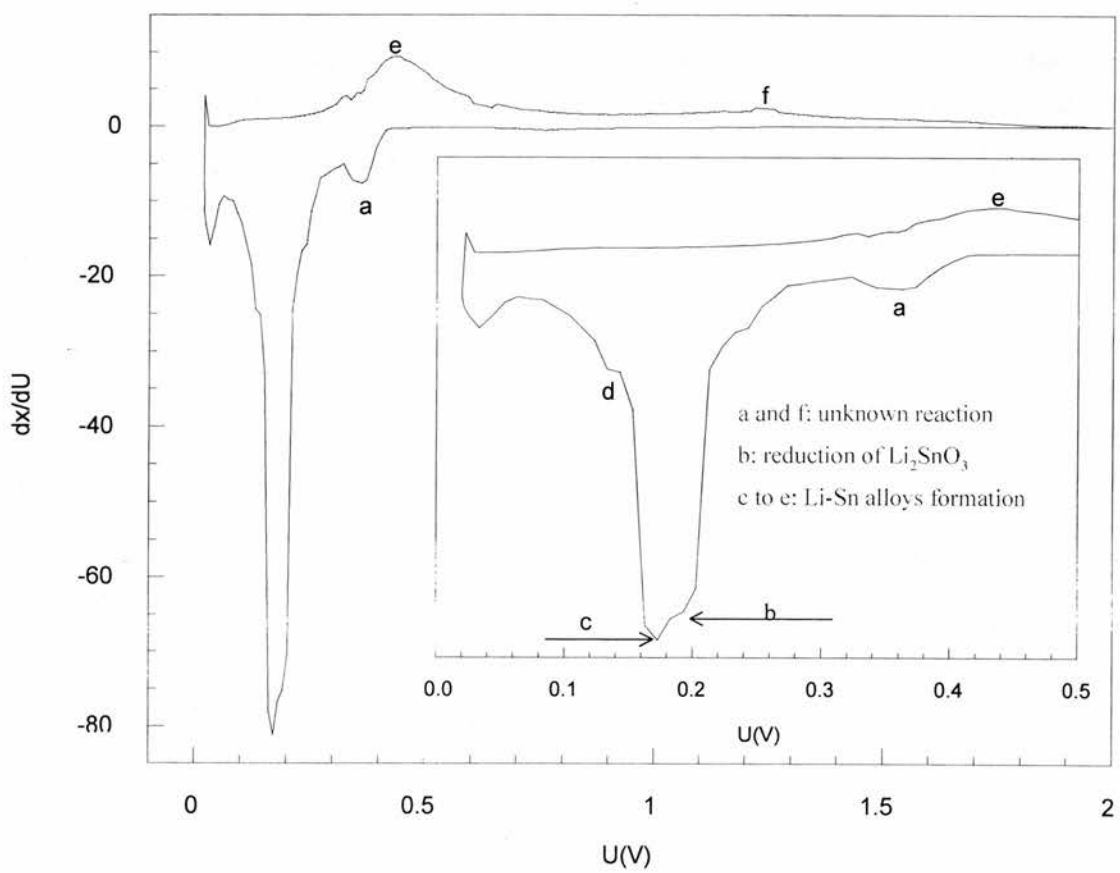

Figure 3.29: Derivative of the galvanostatic plot of Li_2SnO_3-LT cycled between 0.02 and 2 V (0.05 mA)

The initial capacities of Li_2SnO_3-LT and Li_2SnO_3-HT cycled between 0.02 and 2 V with a current of 0.05 mA are summarised in Table 3.9. Li_2SnO_3-LT and Li_2SnO_3-HT have similar initial capacity but Li_2SnO_3-HT has de-inserted more Li than Li_2SnO_3-LT. The difference between the initial charge for Li_2SnO_3-HT and Li_2SnO_3-LT is relatively significant, so to see if this difference will be stable upon cycling, the electrochemical performances of both Li_2SnO_3 materials are compared.

	1st irrev. capacity (mAh/g) *Lithium inserted*		1st rev. capacity (mAh/g) *Lithium de-inserted*	
	Theory	Experiment	Theory	Experiment
Li_2SnO_3 (HT)	1233 *8.4*	1177 *8.02*	643 *4.4*	685 *4.67*
Li_2SnO_3 (LT)	1233 *8.4*	1167 *7.93*	643 *4.4*	596 *4.06*

Table 3.9: Li_2SnO_3 initial capacities

Thus Li_2SnO_3 was cycled between 0.01 and 2 V and the number of Li de-inserted per Sn atom is plotted vs. cycle number Figure 3.30. During the first six cycles the number of Li de-inserted for Li_2SnO_3-HT is superior to that of Li_2SnO_3-LT, although the gap between the two Li_2SnO_3 samples decreases gradually. Thereafter the profile of the performance changes; Li_2SnO_3-LT exhibits slightly better electrochemical performance than Li_2SnO_3-HT, this implies that both Li_2SnO_3 samples have similar structure. SEM measurements were performed on both Li_2SnO_3 samples and the images are shown Figure 3.31. Li_2SnO_3-LT has smaller particle size than Li_2SnO_3-

HT. Li_2SnO_3-LT was prepared at 650 °C with SnO_2 that had been ball-milled 12 hours while Li_2SnO_3-HT was prepared at 1000 °C with non-milled SnO_2. The particle sizes of non-milled SnO_2 and milled SnO_2 are about 1000-5000 nm and 59 nm respectively. After sintering the precursors with small particle size give small particle because the sintering temperature is lower to the temperature used for the precursors with large particle size. Various publications[17-5] have demonstrated that small particle sizes enhance the performance of the electrode as they are thought to accommodate better the reversible alloying process of Sn metal with Li metal. But the particle size difference between both Li_2SnO_3 does not make a big difference in the electrochemical behaviour, as the good performance of Li_2SnO_3-LT is not significantly different to that of Li_2SnO_3-HT. Furthermore the capacity retention of Li_2SnO_3-HT and Li_2SnO_3-LT is very poor. Li_2SnO_3-HT and Li_2SnO_3-LT have lost approximately 92 and 86 % of their initial reversible capacity respectively when the 20^{th} cycle is reached.

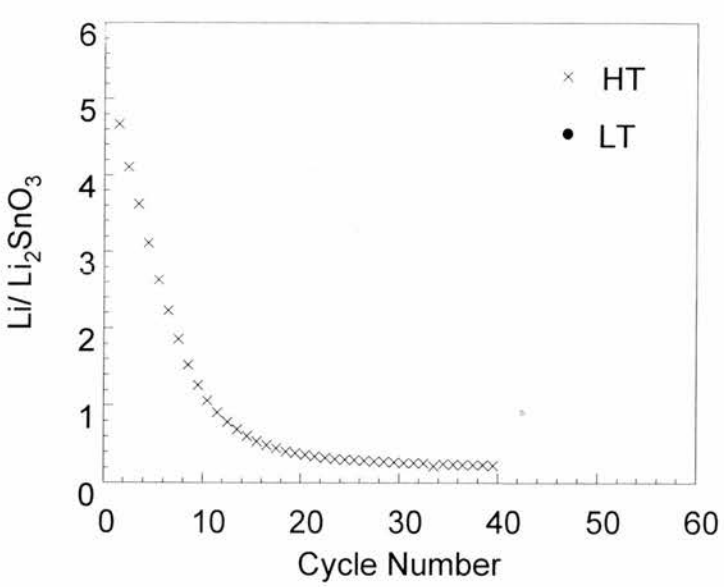

Figure 3.30: Number of Li/Li_2SnO_3 de-inserted vs. cycle number (0.01-2 V)

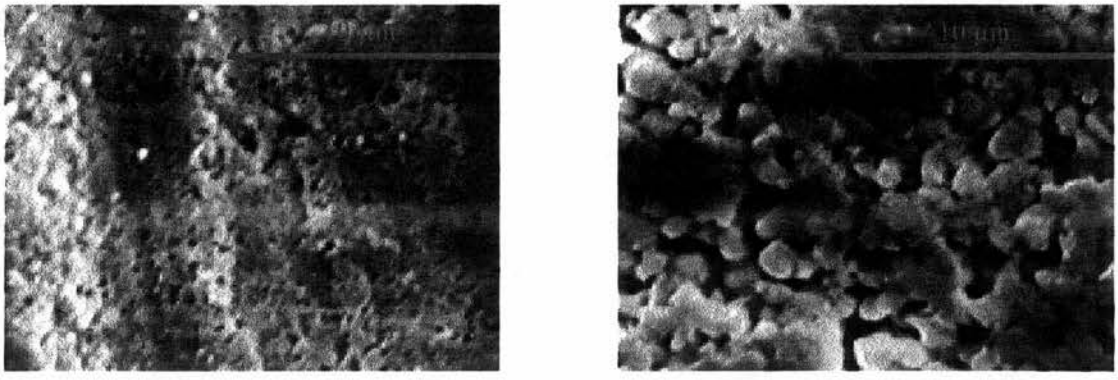

LT HT

Figure 3.31: SEM image of Li_2SnO_3

3.6.2 Cycling performance

The window voltage 0.01-2 V is obviously not the best window voltage to cycle lithium tin oxide. Li_2SnO_3 was also cycled between, 0.01 and 1.5 V, 0.01 and 0.8 V, and the specific reversible capacity of Li_2SnO_3-LT for the two window voltages plotted vs. the cycle number is shown in Figure 3.32. Li_2SnO_3-LT cycled between 0.01 and 0.8 V displays better capacity retention than Li_2SnO_3-LT cycled up to 1.5 V. 60 % of the initial reversible capacity is lost at the 10^{th} cycle when Li_2SnO_3-LT is cycled up to 1.5 V while only 20 % is lost when Li_2SnO_3-LT is cycled up to 0.8 V. The better window voltage in term of capacity retention for Li_2SnO_3-LT is between 0.01 and 0.8 V. Even when Li_2SnO_3-LT is cycled within the optimised window voltage, the capacity loss is very fast. After only 40 cycles the Li_2SnO_3-LT electrode has lost half of its initial capacity, which makes this material an unpromising negative electrode for Li-ion cells. Similar conclusions were observed for Li_2SnO_3-HT.

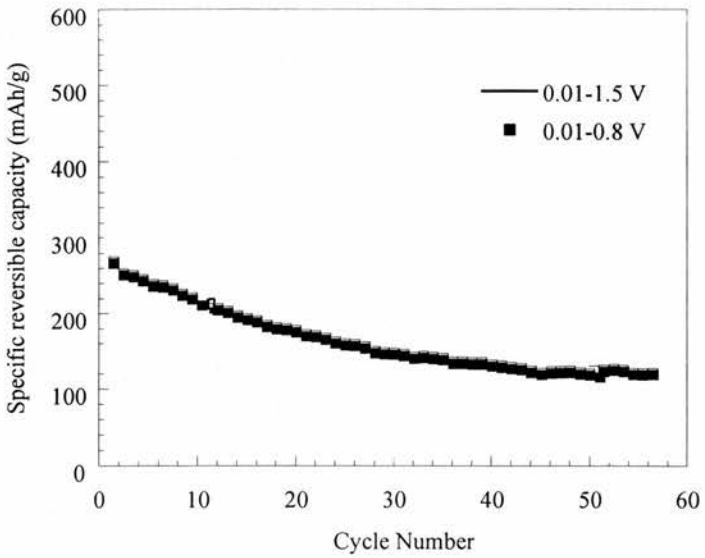

Figure 3.32: Li_2SnO_3-LT specific reversible capacity vs. cycle number

Li_2SnO_3 was initially discharged down to 0.02 V and charged up to 2 V, thereafter the same Li_2SnO_3 was cycled between 0.8 and 2 V several times. The idea is to see if the reversible capacity observed above 0.8 V, is responsible for the poor cyclability of Li_2SnO_3 cycled between 0.02 and 1.5 V. The percentage of the initial reversible capacity of Li_2SnO_3 cycled between 0.01 and 1.5 V, of Li_2SnO_3 cycled between 0.01 and 0.8 V, of Li_2SnO_3 cycled between 0.8 and 2 V after the initial discharge down to 0.02 V was plotted vs. cycle number as shown Figure 3.33. Li_2SnO_3 cycled between 0.8 and 2 V, after the initial discharge down to 0.02 V and Li_2SnO_3 cycled between 0.01 and 1.5 V have similar capacity drop. As seen previously, Li_2SnO_3 cycled between 0.01 and 0.8 V shows better capacity retention. Thus the reversible capacity observed above 0.8 V appears to be responsible for the bad electrochemical performance of Li_2SnO_3 cycled up to 1.5 V.

Li insertion into Sn metal occurs below 0.8 V at room temperature[2], therefore Li-Sn alloys reversible formation is not the source of reversible capacity observed above this voltage. The phenomenon that occurs above degrades the electrochemical performance of Li_2SnO_3. An *ex-situ* XRD performed at the end of the charge on Li_2SnO_3 electrode cycled between 0.8 and 2 V after a complete discharge only reveals the presence of Sn metal. The unidentified compound is probably amorphous.

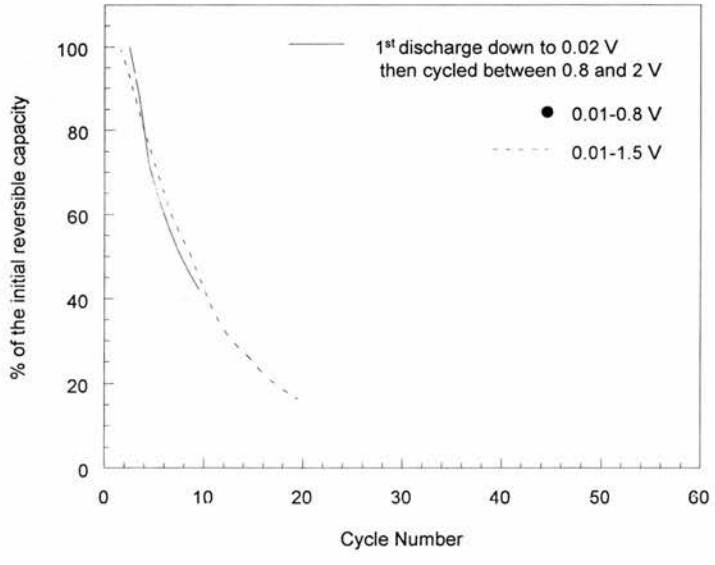

Figure 3.33: Percentage of the initial reversible capacity of Li_2SnO_3-LT vs. cycle number

3.6.3 Electrochemical comparison between Li_2SnO_3 and SnO_2

In their study[1] of Li_2SnO_3 Courtney *et* al. emphasised the importance of the electrochemical behaviour of atoms which are not involved in the alloying / de-alloying process. The derivative profile shows no emergence of bulk lithium-tin phases during the first discharge but clusters begin to appear in subsequent cycles. Tin aggregation is presumably hindered by the presence of "spectator atoms". *In-situ*

XRD showed no presence of tin peaks at the end of the initial charge. This could be the result of the formation of three moles of Li_2O per mole of Li_2SnO_3 compared to two moles of Li_2O per mole of SnO_2, which should slow down the aggregation of tin metal. Despite the irreversible loss caused by the Li_2O formation, it is believed that the Li_2O matrix minimises the volume expansion resulting from the alloying/de-alloying process of Sn with Li although the role of the Li_2O in the electrode performance is far from being well understood[1]. Thus if Li_2SnO_3 is used as a possible anode the Li_2O matrix should promote volume stability.

Winter *et al.* reported a reduction in the expected volume expansion during the formation of lithium-tin alloys whilst using small tin particle sizes and a matrix[5]. Therefore, it is thought that the combination of small particle size and the presence of the Li_2O matrix would enhance the cycle life of the Li_2SnO_3 electrode. Moreover, the number of lithium atoms inserted / de-inserted per tin atom for Li_2SnO_3 and SnO_2 should be equal. So Li_2SnO_3 and SnO_2 should have similar electrochemical performance, but even better cycling performance is expected for lithium tin oxide.

The cycling performance of Li_2SnO_3-LT cycled between 0.01 and 0.8 V and SnO_2 cycled between 0.2 and 0.8 V with a current of 0.1 mA were compared Figure 3.34. SnO_2 initial reversible capacity is higher than Li_2SnO_3-LT initial reversible capacity. Li_2SnO_3-LT has lost around 19 % of its initial reversible capacity whereas SnO_2 has lost about 10 % at the 10^{th} cycle. At the 20^{th} cycle Li_2SnO_3-LT has only 63 % of the initial reversible capacity left and SnO_2 80 %. Li_2SnO_3-LT capacity drops faster than for SnO_2, therefore SnO_2 exhibits better electrochemical behaviour. The extra mole of

Li_2O and the combination of small particle size did not improve the cycle life of Li_2SnO_3-LT.

The shape of the Li_2SnO_3 profile is similar to SnO_2, but the cycling performance is not influenced by SnO_2. The initial electrochemical insertion of Li is different for both oxides. The reduction of Li_2SnO_3 occurs at a very low potential, around 0.18 V compared to the reduction of SnO_2 (0.9 V). Li is inserted reversibly into Sn metal after the reduction of SnO_2 below 0.8 V. But in the case of Li_2SnO_3, the reduction of Li_2SnO_3 and Li insertion into Sn metal occurs simultaneously. The electrochemical performance of the starting material depends on its properties.

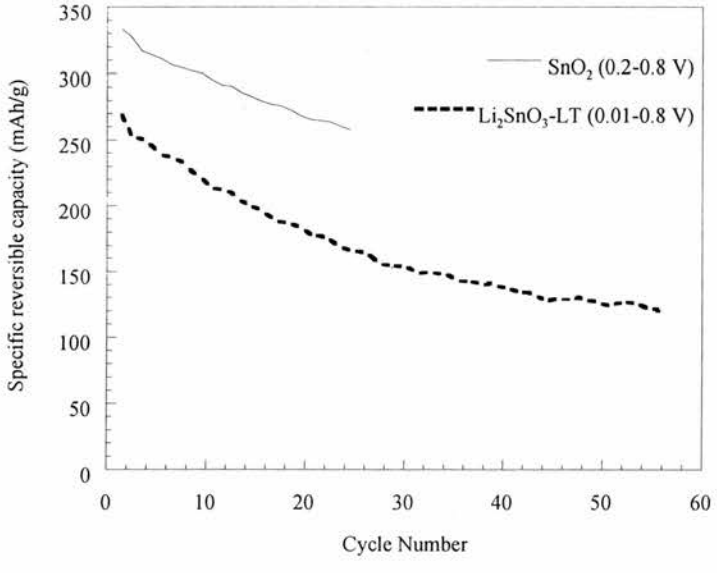

Figure 3.34: Specific reversible capacity of SnO_2 and Li_2SnO_3-LT vs. cycle number

3.7 Discussion

The derivative plots of SnO_2, Li_2SnO_3, Zn_2SnO_4 and ZnO are compared to each other Figure 3.35. Previously in this chapter an anodic peak around 1.25 V was observed for all materials investigated. The peak shape of Zn_2SnO_4 and ZnO is different from SnO_2 and Li_2SnO_3. The peak observed around 1.25 V for SnO_2 matches exactly the peak observed for Li_2SnO_3. The examination of the derivative plot of carbon super S shows as well the presence of this peak (Figure 3.36) around 1.25 V. Thus this peak is not related to the oxides investigated. The shape of the peak observed for the tin oxides is similar to that of carbon. The shape of the peak observed for the tin oxide materials and carbon is not observable for the zinc oxide materials. It is possible that the peak observed for carbon and tin oxides is hidden underneath the well defined peak observed for zinc oxides at the same potential. Thus this peak around 1.25 V could be the result of an instrumental effect, or related to the PVDF or the electrolyte.

The broad anodic peak observed at 0.7 V for Zn_2SnO_4 is similar to the one observed at 0.65 V for ZnO, although it has shifted. This peak was attributed to the re-oxidation of Zn metal according to EXAFS data in the case of ZnO. So the peak at 0.7 V in the case of Zn_2SnO_4 could be related to the re-oxidation of Zn metal as well. This is possible as Zn_2SnO_4 is reduced into Sn metal and Zn metal according to EXAFS and x-rays studies.

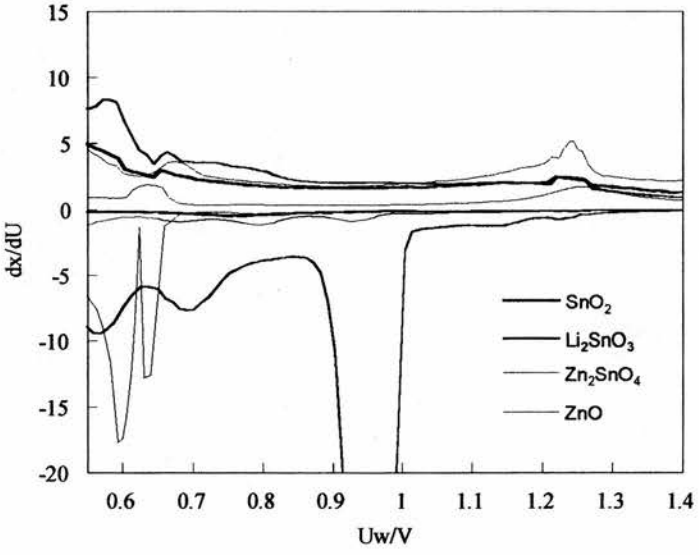

Figure 3.35: Derivative plots of the materials investigated

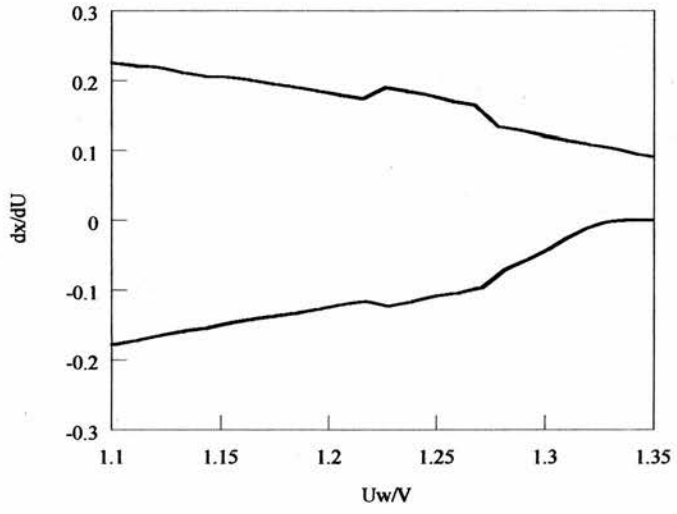

Figure 3.36: Derivative of Super S carbon

3.8 References

1 I. A. Courtney, J. R. Dahn, J. Electrochem. Soc. 144, 2045 (1997)

2 J. Wang, I. D. Raistrick, R. A. Huggins, J. Electrochem. Soc. 133, 457 (1986)

3 C. J. Wen, R. A. Huggins, J. Electrochem. Soc. 128, 1181 (1981)

4 R. A. Huggins, Solid State Ionics 113-115, 57 (1998)

5 M. Winter, J. O. Besenhard, Electrochimica Acta 45, 31 (1999)

6 T. Brousse, D. Defives, L. Pasquereau, S. M. Lee, U. Herterich, D. M. Scheich, Solid State Ionic 113-115, 51 (1998)

7 N. Li, C. R. Martin, B. Scrosati, Electrochem. Solid State Lett. 3, 316 (2000)

8 J. Zhu, Z. Lu, S. T. Aruna, D. Aurbach, A. Gedanken, Chem. Mater. 12, 2557 (2000)

9 S. C. Nam, C. H. Paik, W. I. Cho, H. S. Chun, K. S. Yun, J. Power Sources 84, 24 (1999)

10 T. Brousse, I. Sandu, J. Santos-Pena, M. Danot, R. Retoux, D. M. Scheich, LiBD meeting in Arcachon (2000)

11 I. A. Courtney, J. R. Dahn, J. Electrochem. Soc. 144, 2943, (1997)

12 J. Wang, P. King and R. A. Huggins, Solid State Ionics 20, 185 (1986)

13 T. Fujieda, S. Takahashi, S. Higuchi, J. Power Sources 40, 283 (1992)

14 Z. Chi, M. Liu, J. L. Gole, Electrochem. Solid State Lett. 3, 312 (2000)

15 H. Li, X. Huang, I. Chen, Solid State Ionics 123, 189 (1999)

16 J. O. Besenhard, M. Hess, P. Komenda, Solid State Ionics 40-41, 525 (1990)

17 J. Yang, M. Winter, J. O. Besenhard, Solid State Ionics 90, 281 (1996)

18 M. N. Obrovac, O. Mao, J. R. Dahn, Solid State Ionics 112, 9 (1998)

19 CRC Handbook of Chemistry and physics, 76th edition, CRC Press, Boca Raton, FL, 1995

20 http://www.webelements.com

21 M. Binnewies, E. Milke, Thermochemical Data of Elements and Compounds, WILEY-VCH

4 EXAFS and XRD studies

4.1 ZnO

4.1.1 EXAFS

4.1.1.a Introduction

In Chapter 3 it was demonstrated that ZnO partially follows the mechanism proposed for Tin-Based-Oxide materials[1]. It was shown that during the discharge process ZnO is reduced by Li metal into Zn metal and irreversibly forms the matrix Li_2O; then Li inserts reversibly Zn metal to form several Li-Zn alloys[2-3-4-5]. But during charge another electrochemical phenomenon was revealed above 0.7 V suggesting the formation of an unidentified compound. Consequently the equation below is incomplete:

Equation 4.1: $ZnO + 3.5Li \rightarrow Li_2O + 1.5Zn + Li \leftrightarrow Li_2O + Li_{1.5}Zn$

EXAFS were performed on a ZnO electrode during charge and discharge. In the galvanostatic plot, Figure 4.1 are indicated where the EXAFS data on Zn edge were collected.

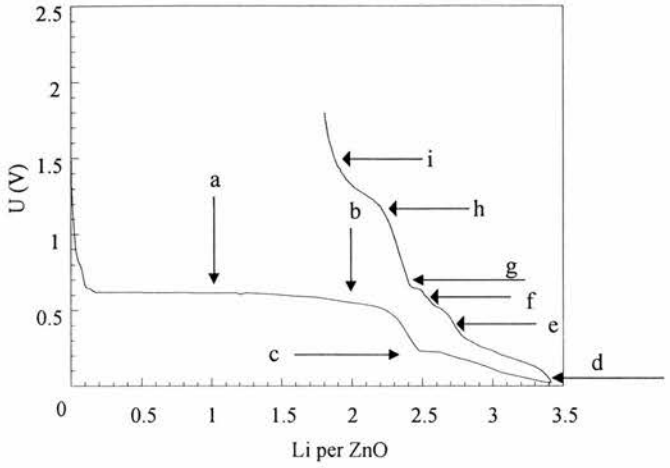

Figure 4.1: ZnO galvanostatic plot with the points (a to i) where the EXAFS data were collected

The theoretical Zn-Zn and Zn-O bond distances described by Albertsson[6] for ZnO (zincite) were used to fit the EXAFS data collected on the ZnO electrode before testing. The resulting fit was used as a starting model for the fitting of the EXAFS data collected on the ZnO electrode during discharge and charge. The Zn-Zn bond distances present in the Zn metal were fitted using the theoretical Zn-Zn bond distances described by Swanson[7] for pure Zn metal. The only Li-Zn alloy present in the JCPDS-ICDD is LiZn (3-954), but the Zn-Zn bond distances within LiZn are not available in the ICSD database. Both LiZn (a = 6.235 Å)[8] and LiAl (a=6.373 Å)[9] have a NaTl type structure and crystallise in a cubic structure-space group Fd3m. the structure of NaTl is shown Figure 4.2. In the NaTl structure, Na and Tl form two independent diamond lattices. Based on this structure and the cell parameter of LiZn, the Zn-Zn bond distances, d present in Li-Zn alloys can be calculated.

$$a\sqrt{3} = 4*d$$

$$d = 6.235\sqrt{3}/4 = 2.699 \text{ Å}$$

The calculated Zn-Zn bond distance is close to the Al-Al bond distances (2.758 Å) described for LiAl[10], and was used to fit the Zn-Zn bond distances present in the Li-Zn alloys.

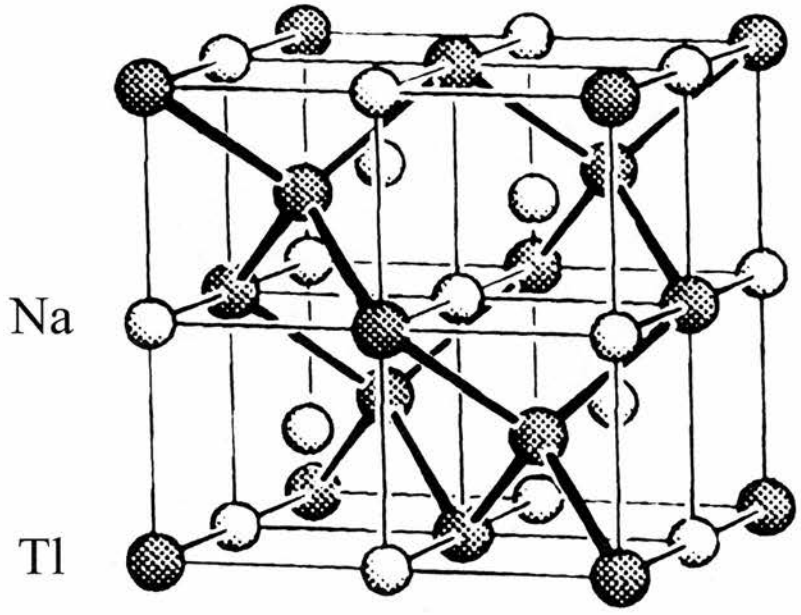

Figure 4.2: NaTl structure (taken from reference 11)

Often during the fitting of the EXAFS data two phases are simultaneously present, zinc oxide and zinc metal phases, which makes the fitting process more complex. An extra parameter is then introduced to estimate the proportion of each phase. It is really important when both phases are present to refine each parameter separately. The best fit obtained for the ZnO electrode during discharge and charge are summarised in Table 4.1 and Table 4.2 respectively.

4.1.1.b Discharge

Figure 4.3 shows the comparison of the EXAFS collected on the ZnO electrode before testing, on the ZnO electrode initially discharged until 0.5 V and discharged until 0.01 V. At 0.5 V the oxygen shell corresponds to ZnO and the Zn shell is attributed to Zn metal. When the battery is fully discharged (0.01 V) only the Zn shell assigned to the Zn metal is noticeable. The intensities due to the oxygen and Zn shell of ZnO decrease with discharge (0.5 V) and disappear completely at 0.01 V, while the Zn shell attributed to Zn metal increases. The bond distances and coordination numbers fitted during the initial discharge of ZnO electrode are shown in Table 4.1.

The fitted Zn-Zn bond distance within the ZnO electrode before testing correlates perfectly with the theoretical Zn-Zn bond distance described for ZnO powder. Before testing the fitted coordination numbers of ZnO electrode match exactly the theory (Table 4.1). EXAFS data were collected when 1 Li/ZnO and 2 Li/ZnO were inserted at the same potential, 0.5 V during the initial discharge. 40 % and 80 % of ZnO were reduced when 1 Li and 2 Li were respectively inserted into ZnO. For ZnO the number of oxygens surrounding the Zn atom decreases with Li insertion at 0.5 V, but the number of Zn surrounding the Zn atom remains constant. At 0.5 V the Zn-Zn bond distance and the coordination number in the Zn metal phase increase with Li insertion. There is no sign of ZnO when ZnO was discharged from 0.2 V until 0.01 V. The coordination number of Zn and the Zn-Zn bond distance in the Zn metal phase decreases from 0.5 V (2Li/ZnO) to 0.01 V.

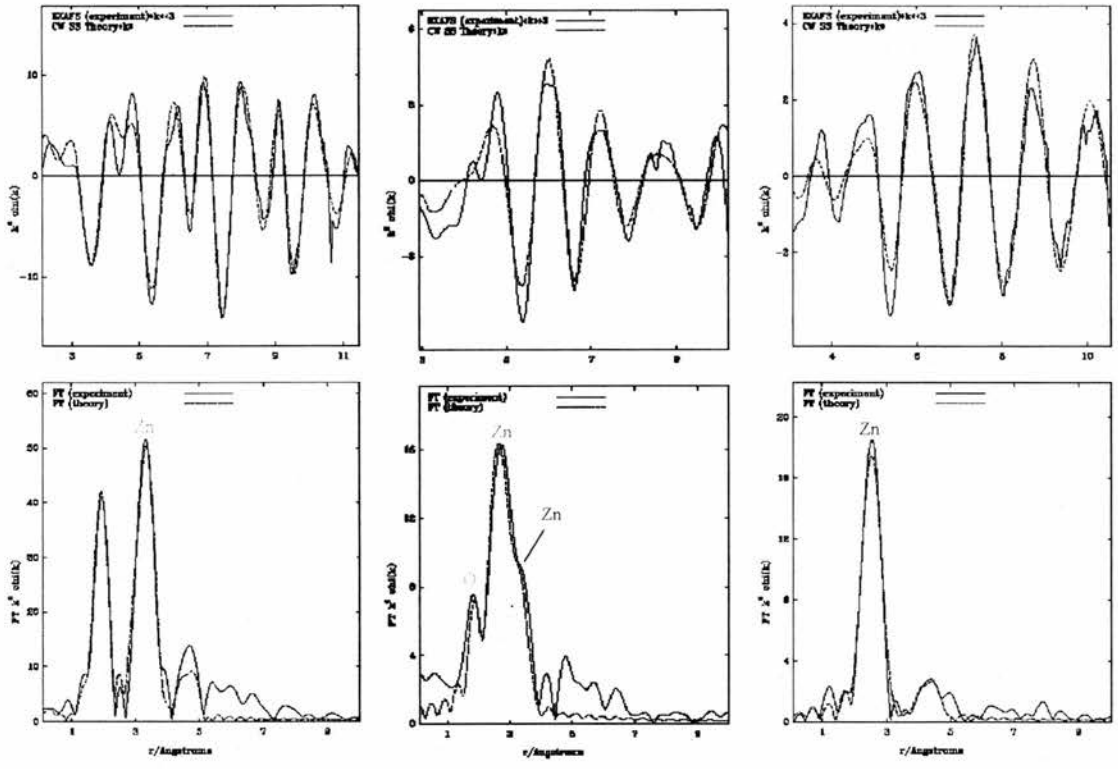

ZnO electrode | ZnO discharged until 0.5 V (2 Li/ZnO) | ZnO discharged until 0.01 V

Figure 4.3: *In-situ* EXAFS collected on Zn edge during the discharge of ZnO

It is very difficult to see the trend of the data presented in Table 4.1, as the bond distances and the coordination numbers observed during discharge are not very consistent. At 0.5 V the bond distances and coordination number of the zinc oxide phase are relatively similar on Li insertion. However, in the Zn phase the Zn-Zn bond distance and coordination number at 0.5 V (1 Li/ZnO) are very low compared to the Zn-Zn bond distance observed at 0.5 V (2 Li/ZnO). At 0.2 V and 0.01 V the bond distances and coordination number are quite similar but lower to that of Zn metal and LiZn.

Potential position	% Phases ± 10 %	Atom type	Coordination number ± 0.1	Distance ± 0.003 Å	R factor	Debye-Waller factor ± 0.001
Theoretical[6] ZnO	ZnO	O Zn	4.0 12.0	1.986 3.242	- -	- -
Theoretical Zn metal[7]	Zn	Zn	6.0	2.665	-	-
LiZn[10]	LiZn	Zn	4.0	2.699	-	-
ZnO electrode before testing	ZnO	O Zn	4.0 12.0	1.957 3.216	28.15	0.010 0.020
0.5 V 1 Li/ZnO (a)	60% of ZnO 40 % of Zn	O Zn Zn	4.0 8.9 1.5	1.967 3.222 2.608	47.31	0.008 0.013 0.010
2 Li/ZnO (b)	20 % of ZnO 80% of Zn	O Zn Zn	3.7 9.0 6.1	1.989 3.196 2.640	40.39	0.011 0.017 0.031
0.2 V (c)	100% of Zn	Zn	2.7	2.634	38.96	0.018
0.01 V (d)	100% of Zn	Zn	2.5	2.636	29.85	0.020

Table 4.1: *In-situ* EXAFS collected on Zn edge during the discharge of ZnO

The absorption near the Zn edge of ZnO collected during the initial discharge was examined Figure 4.4. The shape of the Zn absorption plot changes and shifts to the right on Li insertion. The peak observed for the ZnO electrode corresponds to a Zn atom with the oxidation state +2. At 0.5 V the peak is still present, as the reduction of

ZnO is not complete. The intensity of this peak decreases with Li insertion and disappears at 0.01 V. This means that Zn^{2+} has been completely reduced to Zn metal. These observations are in accord with the EXAFS data confirming the reduction of ZnO into Zn metal on Li insertion.

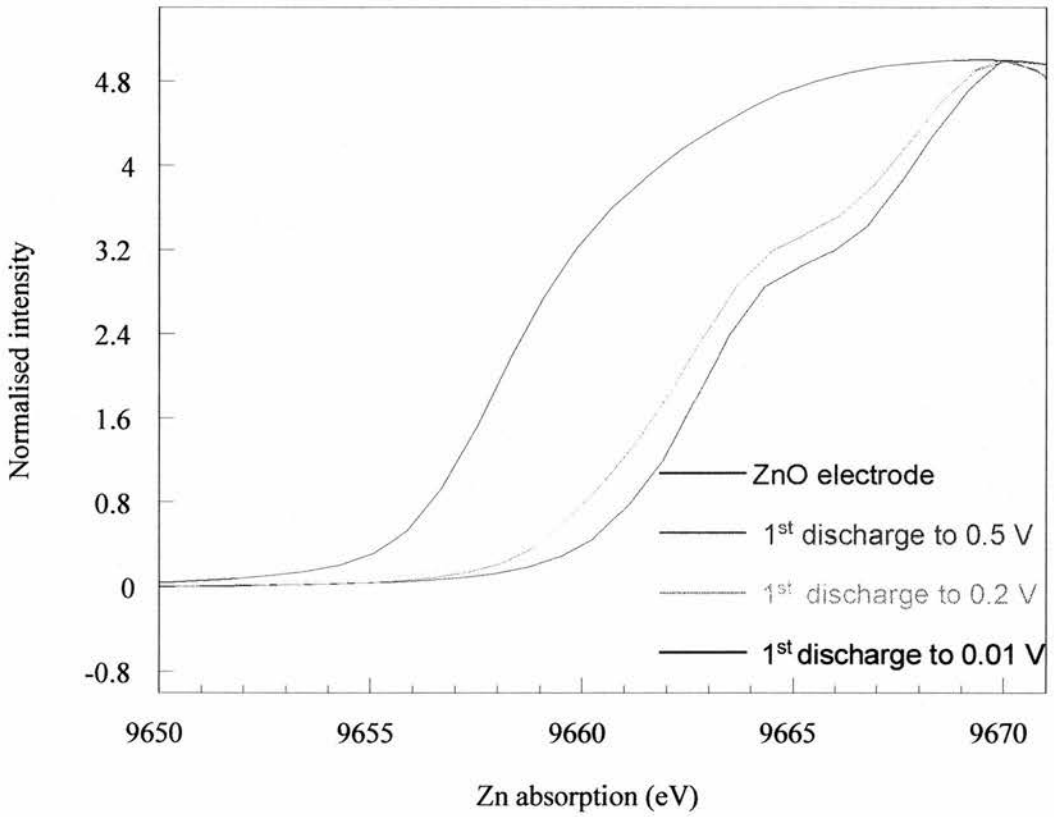

Figure 4.4: Zn XANES collected on ZnO electrode during discharge

4.1.1.c Charge

Table 4.2 shows the fitted EXAFS data collected during the charge of ZnO electrode. The coordination number in the Zn metal phase increases from the discharge at 0.01 V to the charge at 1.5 V. The Zn-Zn bond distance in the Zn metal phase as a whole

increases with charge. From 0.7 V until 1.5 V the Zn metal phase and a zinc oxide phase are simultaneously present. At 0.7 V there is 20 % of this zinc oxide phase, which remains constant until 1.5 V. The number of oxygens surrounding the Zn atom and the Zn-O bond distance in this zinc oxide phase increases until 1.5 V.

The coordination number in the Zn metal phase increases because the Zn atom is less surrounded by Li atoms due to the de-alloying of Li from the Zn metal occurring during charge. The coordination number of the Zn metal phase at 1.5 V is similar to the coordination number of the theoretical Zn metal. The Zn-Zn bond distance at 1.5 V of the Zn phase is much closer to the Zn-Zn bond distance of Zn metal than the Zn-Zn bond distance observed when ZnO was discharged until 0.01 V. This concurs with the de-insertion of Li from the Li-Zn alloy occurring during charge that leads to Zn metal.

The presence of a zinc oxide phase above 0.6 V during charge suggests the re-oxidation of Zn metal. The EXAFS data collected on ZnO during charge between 0.7 V and 1.5 V were performed *ex-situ*, thus on different electrodes. The Zn-O bond distances are different from the fitted Zn-O bond distance of the ZnO electrode. The Zn-O bond distances are smaller than that of ZnO electrode for 0.7 V and 1.25 V, and decreases from 0.7 V to 1.25 V. At 1.5 V the Zn-O bond distances increases and is higher compared to the Zn-O bond distances fitted for ZnO electrode. The number of oxygen atoms surrounding the Zn atom increases with charge. The bond distances of this zinc oxide are so inconsistent that is difficult to make some conclusions. The percentage of this zinc oxide remains constant from 0.7 V to 1.25 V, which suggests

that Zn metal is only re-oxidised between 0.6 V and 0.7 V. The re-oxidation of Zn metal occurs at a similar potential to the plateau around 0.6 V Figure 4.1, which is situated slightly above the potential of reduction of ZnO at 0.5 V.

Potential position	% Phases ± 10 %	Atom type	Coordination number ± 0.1	Distance ± 0.003 Å	R factor	Debye-Waller factor ± 0.001
Theoretical Zn metal[7]	Zn	Zn	6.0	2.665	-	-
LiZn[10]	LiZn	Zn	4.0	2.699	-	-
ZnO electrode before testing	ZnO	O Zn	4.0 12.0	1.957 3.216	28.15	0.010 0.020
Discharge until 0.01 V (d)	100% of Zn	Zn	2.5	2.636	29.85	0.020
0.4 V (e)	100% of Zn	Zn	3.1	2.661	38.37	0.019
0.6 V (f)	100% of Zn	Zn	4.4	2.636	19.99	0.022
0.7 V (g)*	20% of Zn-O 80 % of Zn	O Zn	3.4 5.3	1.949 2.636	31.37	0.011 0.025
1.25 V (h)*	20% of Zn-O 80 % of Zn	O Zn	3.6 5.6	1.939 2.645	42.36	0.011 0.025
1.5 V (i)*	20% of Zn-O 80 % of Zn	O Zn	5.1 6.3	1.989 2.683	38.67	0.011 0.031

Table 4.2: ZnO *in-situ* EXAFS collected on Zn edge during charge (* *ex-situ* EXAFS)

To visualise better the re-oxidation of Zn metal, EXAFS collected on ZnO charged up to 0.6 and 1.5 V are compared to the EXAFS collected on the ZnO electrode before testing Figure 4.5. The blue line represents the exact Zn-O bond distance found in the

ZnO electrode before testing. The Zn-O bond distance for ZnO electrode before testing is not observable at 0.6 V and 1.5 V. This suggests that the zinc oxide formed above 0.6 V is different from the starting ZnO (zincite).

The absorption near the Zn edge of ZnO during charge was examined Figure 4.6. The Zn absorption plot of ZnO shifts to the right on charge compared to ZnO fully discharge (0.01 V) until 0.7 V, then shift back to left at 1.25 V. The shift of the Zn absorption plot to the right on charge corresponds to the de-alloying of Zn metal with Li. A peak is observed at 0.7 V and this peak is similar to the peak noticed for ZnO electrode, which corresponds to Zn^{2+}. Thus the peak observed at 0.7 V suggests the presence of a zinc oxide, this implies the re-oxidation of Zn metal on charge above 0.6 V. Even a small amount of Zn metal has been re-oxidised, the de-alloying of Zn metal with Li metal continues theoretically up to 0.8 V. That is the reason for the reduction of the peak corresponding to the re-oxidation of Zn metal and the left shift of the Zn absorption plot at 1.25 V.

It should be pointed out that the EXAFS collected between 0.7 V and 1.5 V were done *ex-situ*. Thus it is possible that the re-oxidation of Zn metal is caused by exposure to air. But it seems almost impossible as the battery was opened inside an Ar-filled glove box and then the electrode was placed into a coin cell designed for *in-situ* measurements that provides an excellent seal, as described in chapter 2. Zn metal is relatively stable to air oxidation unless very fine particles. Furthermore other authors have reported the re-oxidation of copper[12], cobalt[13] and tin[14] during charging which makes the re-oxidation of Zn metal possible.

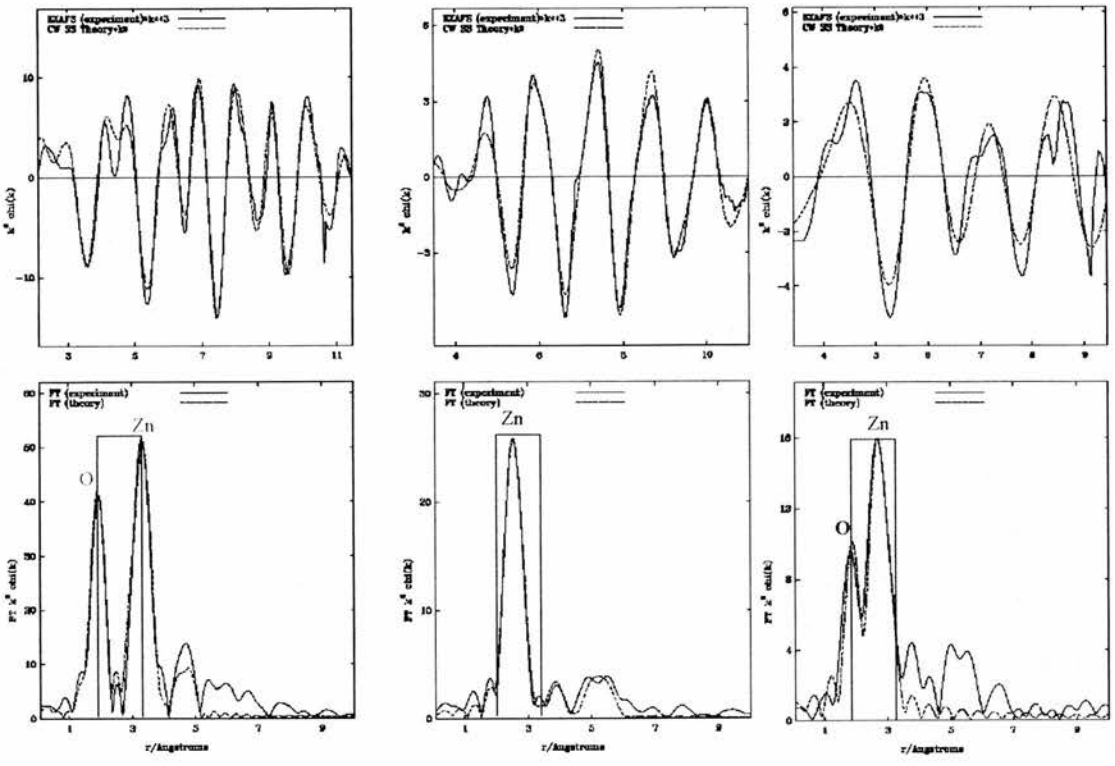

Figure 4.5: Comparison of EXAFS data during the charge of ZnO

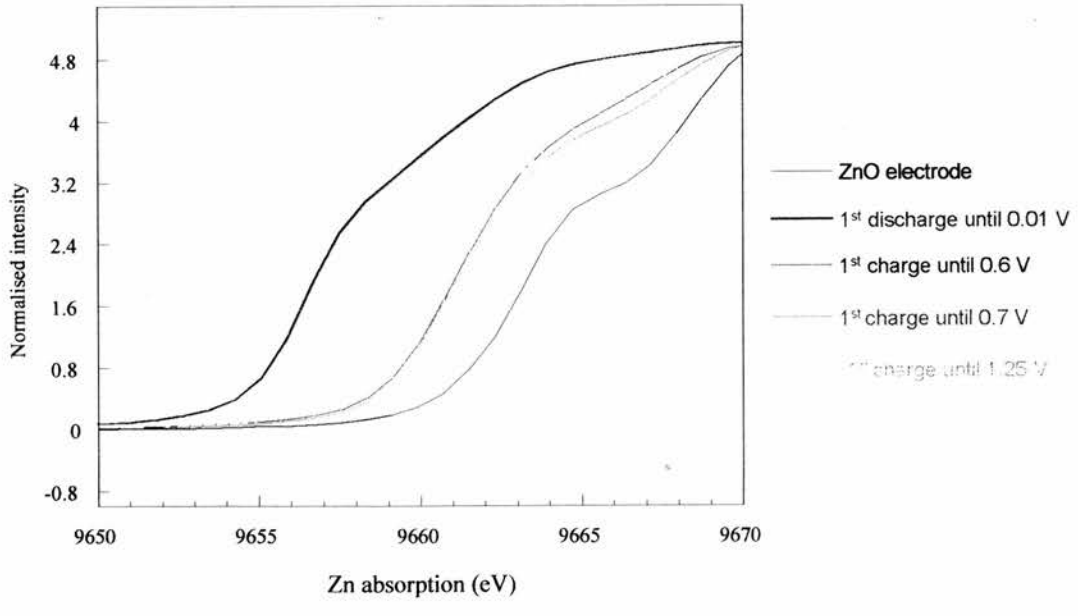

Figure 4.6: Zn XANES collected on ZnO electrode during charge

4.1.1.d Conclusion

EXAFS investigations on Li inserted ZnO confirm the reduction of ZnO into Zn metal. The reduction of the coordination number decrease in Zn-Zn bond distance in the Zn metal confirms that alloying of Zn metal with Li occurs during discharge. During charge the augmentation of the number of Zn atoms surrounding Zn in the Zn metal phase confirms the reversibility of Li-Zn alloys formation. However, during charge another phenomenon occurs above 0.6 V, the re-oxidation of Zn metal. This means that the suggested mechanism, via Equation 4.1 is incomplete. Thus a refinement of this equation is necessary.

It is assumed that the irreversible capacity lost observed electrochemically during the initial discharge is caused by the irreversible formation of Li_2O. But if a small amount of Zn metal is re-oxidised during charge, a partial decomposition of Li_2O is necessary to provide the oxygen atoms. Thus the formation of Li_2O is not totally irreversible as suggested in Equation 4.1. As a result a more accurate equation explaining the mechanism occurring during charging can be written as follows:

Equation 4.2: $ZnO + 3.5Li \rightarrow Li_2O + Li_{1.5}Zn$ discharge

Equation 4.3: $(1-x)Li_2O + Li_{1.5}Zn \leftrightarrow (1-2x)Li_2O + x\ ZnO + (1.5-x)Zn + (1.5+2x)Li$ charge

x: proportion of re-oxidised Zn metal

4.1.2 XRD

4.1.2.a Results

XRD was performed on the inserted ZnO electrodes *in-situ* and *ex-situ.* For the *in-situ* measurement a Cu grid was used as current collector and as internal standard. The Cu grid was also used as internal standard for *ex-situ* measurements.

The XRD pattern collected *in-situ* for a ZnO electrode discharged until 0.05 V is shown Figure 4.7. Peaks corresponding to the internal standard, ZnO and LiZn are observable. The presence of ZnO peaks means that the reduction was not complete, although the battery was discharged until 0.05 V. The incomplete reduction of ZnO is due to the cell designed for *in-situ* measurements as described in chapter 2 that lowers the electrochemical performance of the battery. The surprising result is the degree of crystallinity of LiZn alloy in the XRD pattern, which confirms the alloying of Zn metal with Li during discharge. The presence of LiZn reveals as well that ZnO is reduced into highly crystalline metal, which forms high crystalline Li-Zn alloy.

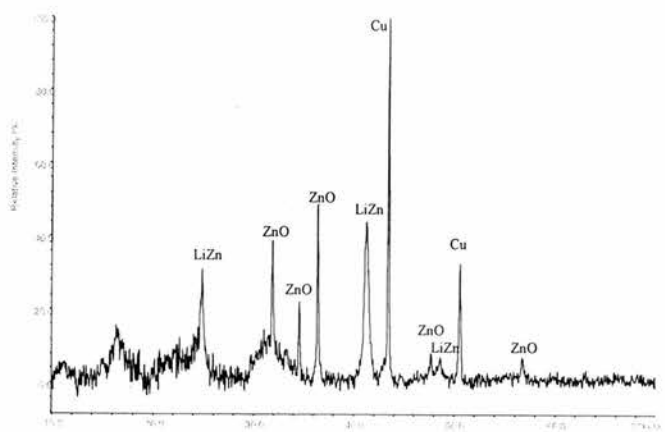

Figure 4.7: *In-situ* XRD collected on ZnO electrode discharged until 0.05 V

Ex-situ XRD measurements carried out at the end of charge on a ZnO electrode cycled between 0.02 and 2 V is shown Figure 4.8. In the XRD pattern only peaks corresponding to Zn metal and Cu grid are observable. The presence of Zn metal at the end of the charge confirms the reduction of ZnO into Zn metal and the reversible alloying process of Zn metal with Li.

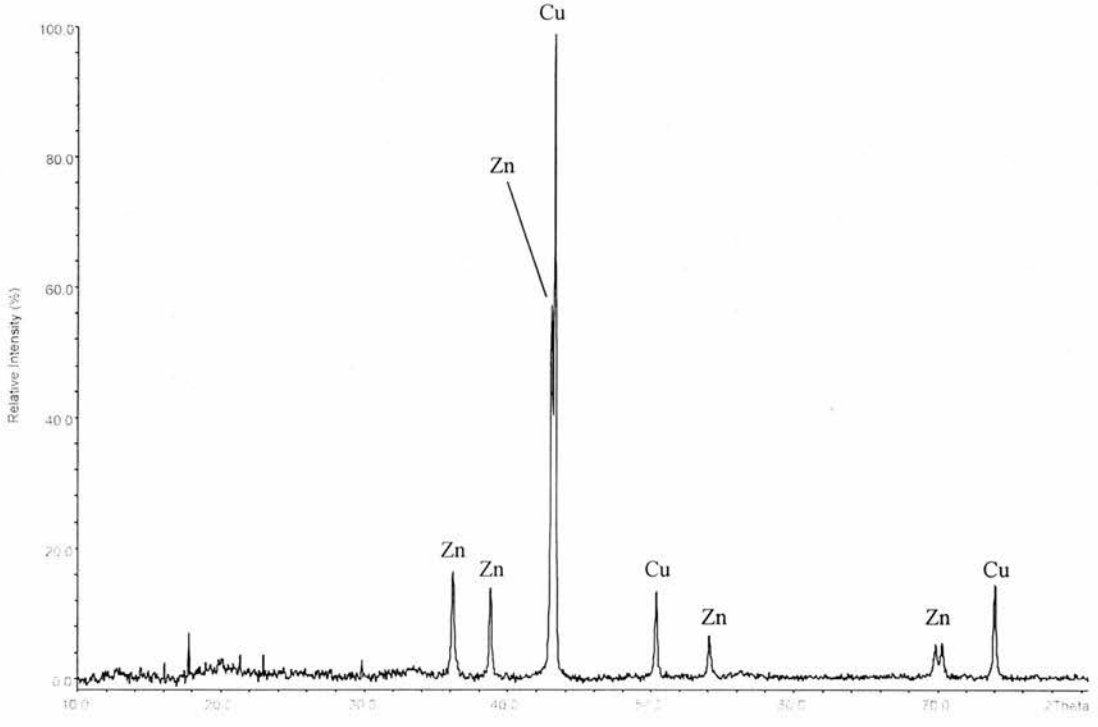

Figure 4.8: *Ex-situ* XRD collected on ZnO electrode at the end of the 1st cycle (0.02-2 V)

In chapter 3 it was demonstrated that the cycling range of voltage influences the cycling performance of the electrode. Thus the XRD pattern collected on ZnO cycled between 0.1 and 0.8 V was compared to the XRD pattern collected on ZnO cycled between 0.2 and 0.8 V in Figure 4.9. XRD data were collected at the end of the charge (0.8 V) where the Cu grid and Zn metal peaks can be seen. Zn metal peaks are more

intense for ZnO cycled down to 0.1 V compared to ZnO cycled down to 0.2 V even for a smaller number of cycles.

The cycling performance of these two ZnO electrodes cycled down to 0.1 and 0.2 V were compared to each other, Figure 4.10. ZnO cycled down to 0.1 V has greater reversible capacity during the first two cycles and thereafter the capacity fades so quickly that at the 10^{th} cycle there is no capacity left. Cycling ZnO down to 0.2 V retains capacity better well until the 6^{th} cycle then the capacity drops slowly in comparison to ZnO cycled until 0.1 V. Overall ZnO cycled between 0.2 and 0.8 V displays better capacity retention. Thus the cycling performance of the ZnO electrode is intimately linked to the degree of crystallinity of Zn metal.

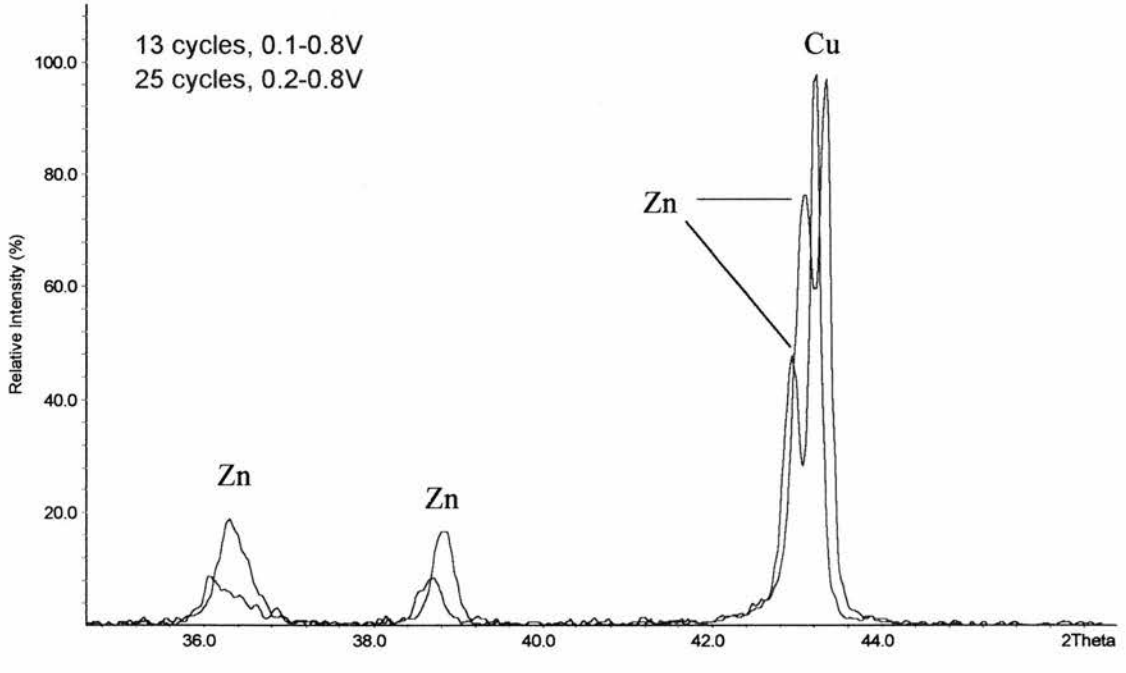

Figure 4.9: *Ex-situ* XRD collected on ZnO electrode at the end of charge

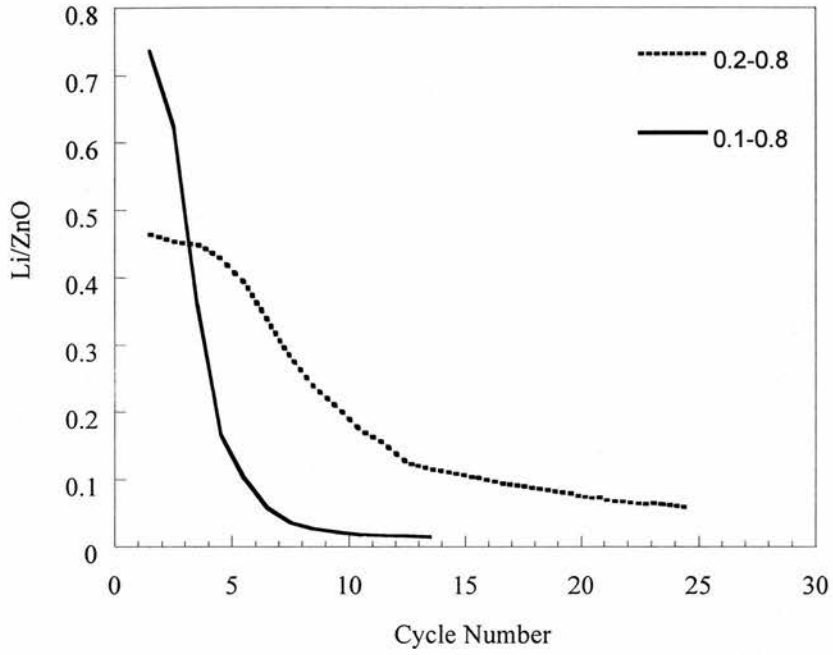

Figure 4.10: Li de-inserted per ZnO vs. cycle number

4.1.2.b Conclusion

The reduction of ZnO into Zn metal during the initial discharge and the reversible insertion of Li into Zn metal were verified by XRD measurements. The re-oxidation of Zn metal observed through EXAFS during charge is undetectable by XRD. This suggests that the zinc oxide formed during charge is either too amorphous or in too small quantity to be detected by XRD. The principal information extracted from the XRD pattern, however is that Zn metal is crystalline after the initial discharge. ZnO material cycles poorly, as reported in chapter 3, since after the initial discharge Zn metal is already quite crystalline, which leads to the quick degradation of the electrode. Thus crystallinity is a determining factor in the electrochemical performance of the electrode.

4.2 $ZnO:SnO_2$ systems

4.2.1 Electrochemistry review

In the $ZnO:SnO_2$ systems, ZnO and SnO_2 behave independently electrochemically. The reduction of SnO_2 and ZnO occur successively approximately at 0.95 V and 0.6 V respectively. Two plateaus corresponding to the reversible formation of Li-Sn alloys and Li-Zn alloys were visible on the galvanostatic plots during the initial discharge. Most of the Li inserted reversibly into Sn and Zn metal seems to occur after the reduction of ZnO (0.6 V)[15-16].

4.2.2 EXAFS

4.2.2.a Zn edge

EXAFS data were collected *ex-situ* on the $ZnO:SnO_2$ (1:1) mixture ball-milled 12 hours on the Zn edge. This mixture was cycled once between 0.02 and 1.8 V and the EXAFS collected at the end of charge is shown Figure 4.11. Two shells are observable, an oxygen shell and a Zn shell. The fitted bond distances and coordination number collected during charge at 1.8 V are summarised in Table 4.3.

At 1.8 V, two phases are in presence, a zinc oxide phase and a Zn metal phase. The coordination number in the Zn metal phase is similar in the matrix to the coordination number of Zn metal. Thus the Zn shell observed in Figure 4.11 can be attributed to Zn metal. However, the Zn-Zn bond distance is smaller than the theoretical bond distance in Zn metal.

The Zn-O bond distance of the zinc oxide phase is smaller than the fitted Zn-O bond distance within the ZnO electrode before testing. The oxygen and Zn shells observed on charge for $ZnO:SnO_2$ at 1.8 V are similar to that observed for a ZnO electrode charged up to 1.5 V (Figure 4.5). So the 30 % of zinc oxide observed is different from the starting ZnO present in $ZnO:SnO_2$. The re-oxidation of Zn metal was expected in the $ZnO:SnO_2$ as ZnO and SnO_2 are reduced separately electrochemically.

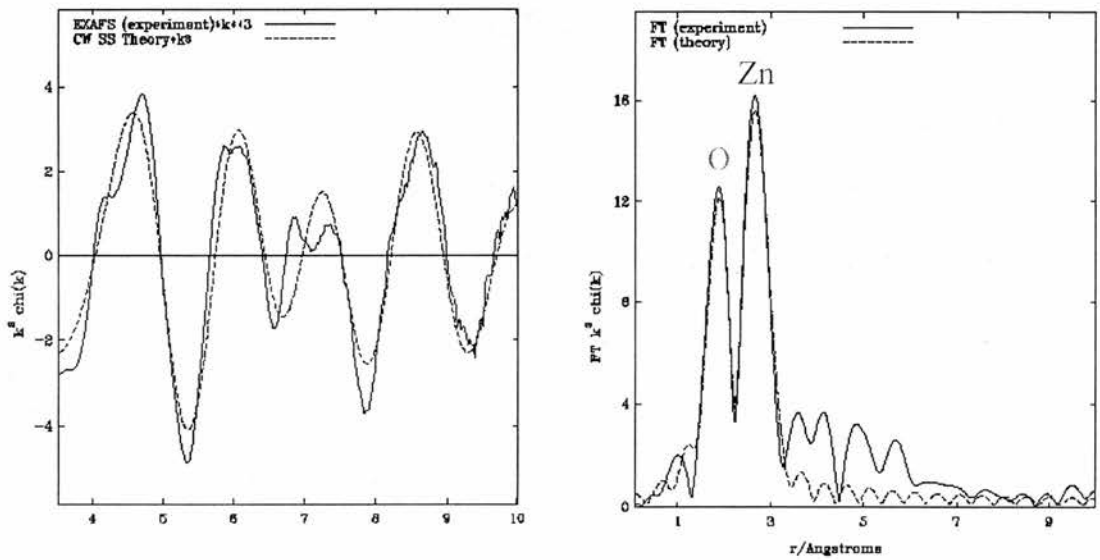

Figure 4.11: *Ex-situ* EXAFS collected on the Zn edge of $ZnO:SnO_2$ (1:1) ball-milled 12 hours at the end of the initial charge (0.02-1.8 V)

Potential position	% Phases ± 10 %	Atom type	Coordination number ± 0.1	Distance ± 0.003 Å	R factor	Debye-Waller factor ± 0.001
Theoretical Zn metal[7]	Zn	Zn	6.0	2.665	-	-
LiZn[10]	LiZn	Zn	4.0	2.699	-	-
ZnO electrode before testing	ZnO	O Zn	4.0 12.0	1.957 3.216	28.15	0.010 0.020
Charge until 1.8 V	30% of Zn-O 70 % of Zn	O Zn	4.5 6.1	1.942 2.649	31.94	0.013 0.031

Table 4.3: *Ex-situ* EXAFS data collected on ZnO:SnO_2 (1:1) (12 hours ball-milling) at the end of the initial charge (0.02-1.8 V)

4.2.2.b Sn edge

The SnO_2 present in ZnO:SnO_2 (1:1) mixture electrode was fitted using the theoretical Sn-O and Sn-Sn bond distances described by Seki *et al.* [17] (Table 4.4). The Sn-Sn bond distances observed in the Sn metal phases were fitted using the theoretical bond distances described for either alpha[18] Sn or beta[19] Sn. EXAFS were performed *in-situ* during discharge as shown Figure 4.12. The Sn-Sn bond distances present in the Li-Sn alloys were fitted using the Sn-Sn bond described for Li_2Sn_5 alloy[20].

Figure 4.12 shows the EXAFS data collected on the same battery for ZnO:SnO_2 (1:1) discharged until 0.5 V. Unfortunately no Sn EXAFS were recorded below 0.5 V because the battery degraded. The intensity of the oscillations decreases with Li insertion. Thus the tin and oxygen shells (in green) attributed to SnO_2 decrease with

Li insertion. The experimental Sn-O and Sn-Sn bond distances and coordination number extracted from Figure 4.12 are summarised in Table 4.4. SnO_2 was not reduced at 0.8 V and at 0.7 V during the initial discharge, and at 0.5 V 30 % of SnO_2 was reduced. At 0.8 V two shells of Sn atoms belonging to SnO_2 were fitted, but at 0.7 V and at 0.5 V only one Sn shell could be fitted. The coordination number of the Sn metal phase remains constant whereas the Sn-Sn bond distance increases with discharge.

At 0.8 and 0.7 V SnO_2 was not reduced while 2 and 3 Li were inserted. When 4 Li (0.5 V) are inserted only 30 % of SnO_2 was reduced which is 70 % lower than the theoretical 4 Li needed to reduce completely SnO_2. Only a part of this poor electrochemical performance can be attributed to the design of the *in-situ* cell. The Sn-Sn bond distance of the Sn metal phase at 0.5 V is situated between the Sn-Sn bond distance of alpha and beta tin. In Table 4.4, the R factors displayed are very high, about 60 at 0.5 V, which means that the fitting is not good as can be seen in Figure 4.12. It should be pointed out that the fitting was so difficult that the Debye-Waller was not fitted at 0.7 V and 0.5 V. The oscillations contain so many instrumental glitches that it was almost impossible to remove them without damaging the EXAFS data. As a result the proportion of SnO_2 and Sn displayed in Table 4.4 are presumably not correct despite the fact that the *in-situ* cell design lowers the electrochemical performance.

As the fitting was so bad, an alternative way of seeing the reduction of SnO_2 was used. The experimental intensity k^3 chi (k) of the oxygen shell of ZnO:SnO_2 (1:1) (12

hours ball-milling) were calculated manually from the Fourier Transform plot as can be seen in Figure 4.12. Thus the experimental oxygen intensity observed in this mixture was plotted vs. the number of Li inserted (Figure 4.13). Figure 4.13 shows more clearly the reduction of SnO_2 into Sn metal compared to the EXAFS data presented in Figure 4.12. Approximately 18 % of the oxygen intensity is lost when 2 Li are inserted, then when 4 Li are inserted about 60 % of the initial intensity is lost. These numbers are much better than those showed in Table 4.4, although it was expected a complete reduction of SnO_2 at 0.5 V (4 Li inserted).

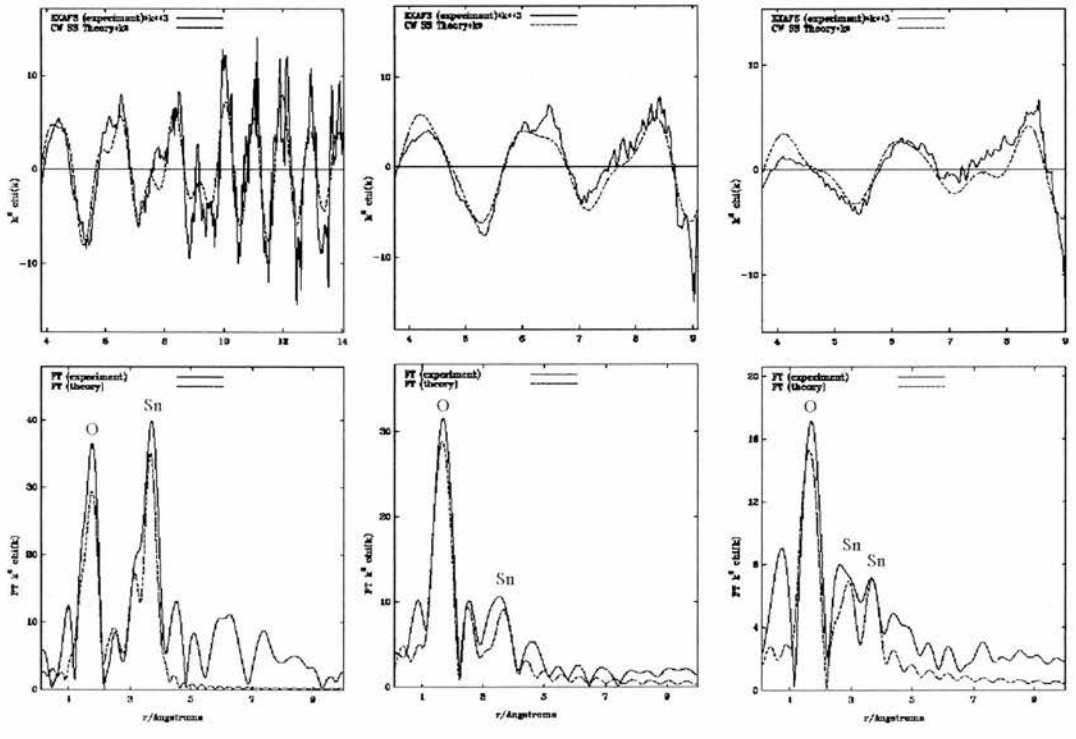

1st discharge down to 0.8 V (2 Li/ZnO:SnO_2) 1st discharge down to 0.7 V (3 Li/ZnO:SnO_2) 1st discharge down to 0.5 V (4 Li/ZnO:SnO_2)

Figure 4.12: *In-situ* EXAFS on the Sn edge collected on ZnO:SnO_2 (1:1) (12 hours ball-milling) during the initial discharge

Potential position	% Phases ± 10 %	Atom type	Coordination number ± 0.1	Distance ± 0.003 Å	R factor	Debye-Waller factor ± 0.001
Theoretical[17] SnO_2	SnO_2	O	6.0	2.058	-	-
		Sn	2.0	3.193	-	-
		Sn	8.0	3.716	-	-
SnO_2 in the ZnO:SnO_2 (1:1) mixture before testing	SnO_2	O	6.0	2.055	43.30	0.014
		Sn	2.0	3.163		0.031
		Sn	4.0	3.739		0.007
Li_2Sn_5[20]	Li-Sn alloy	Sn	1.0	3.113	-	-
Theoretical alpha Sn[18]	Sn	Sn	4.0	2.810	-	-
Theoretical beta Sn[19]	Sn	Sn	4.0	3.023	-	-
0.8 V (2 Li/ZnO-SnO_2)	100% of SnO_2	O	6.0	2.034	47.63	0.011
		Sn	2.2	3.179		0.009
		Sn	7.0	3.711		0.010
0.7 V (3 Li/ ZnO-SnO_2)	100% of SnO_2	O	6.0	2.058	33.96	0.010
		Sn	3.9	3.657		0.010
0.5 V (4 Li/ ZnO-SnO_2)	70% of SnO_2	O	4.0	2.058	60.13	0.010
		Sn	3.2	3.657		0.010
	30% of Sn	Sn	4.0	2.914		0.010

Table 4.4: *In-situ* EXAFS on Sn edge collected on ZnO:SnO_2 (1:1) (12 hours ball-milling) during discharge

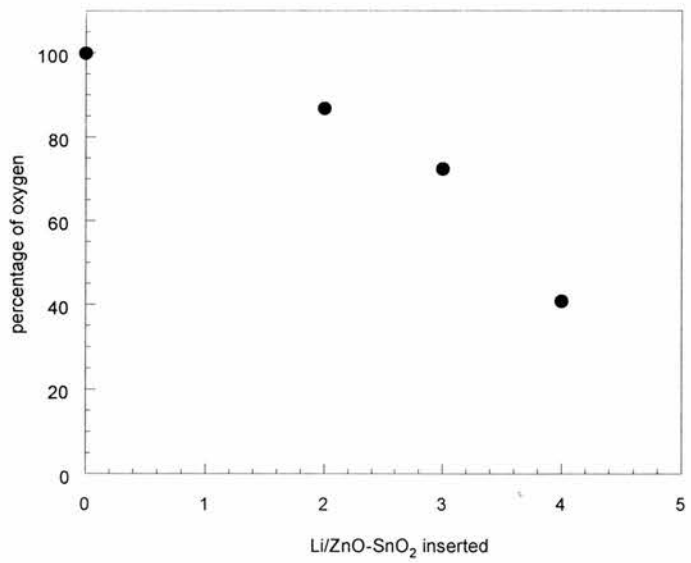

Figure 4.13: Oxygen intensity in SnO_2 for ZnO:SnO_2 (1:1) (12 hours ball-milling) vs. Li/ZnO:SnO_2 inserted

4.2.2.c Conclusion

It was demonstrated in the previous sections from XRD measurements that the reduction of ZnO leads to crystalline Zn metal. Thus the EXAFS data collected on the Zn edge for the mixture Figure 4.11 are probably so discernible due to the crystallinity of Zn metal. It is very difficult or almost impossible to follow the mechanism occurring during discharge and charge when EXAFS performed on the mixture is collected on the Sn edge (Figure 4.12). Thus the reduction of SnO_2 leads to amorphous Sn metal, which explains the decrease of the oscillations observed with the increase of the number of Li inserted as shown in Figure 4.12. For amorphous Sn metal, the oscillations corresponding to EXAFS cannot be differentiated from the background noise. Crystalline metal gives excellent EXAFS data whilst amorphous metal does not provide good EXAFS data. This is somewhat surprising as EXAFS is frequently used to probe the short-range order in glasses. It seems clear that the amorphous tin discussed herein not only has long range disorder but also must exhibit significant disorder at shorter length scales.

4.2.3 XRD

Sn and Zn metals are present in all *ex-situ* XRD performed on the $ZnO:SnO_2$ mixtures cycled several times. The XRD patterns of $ZnO:SnO_2$ (1:1), $ZnO:SnO_2$ (1:2) and $ZnO:SnO_2$ (2:1) are compared to each other Figure 4.14. Intense Sn peaks are observable for all mixtures whereas the intensity of Zn peaks varies as function of the $ZnO:SnO_2$ ratio. Zn peaks are more intense $ZnO:SnO_2$ (2:1) because in this mixture

there is twice as much ZnO by mole. In the $ZnO:SnO_2$ (1:1) and $ZnO:SnO_2$ (1:2) although Zn metal is very crystalline, its crystallinity is masked by the amount of SnO_2 present in the mixture. The crystallinity of Sn metal observed in all mixtures explains their poor electrochemical performance as seen in chapter 3. Plus the $ZnO:SnO_2$ (2:1) mixture has the worst cycling performance compared the other two mixtures because of the high degree of crystallinity of Zn metal, which impairs the electrode.

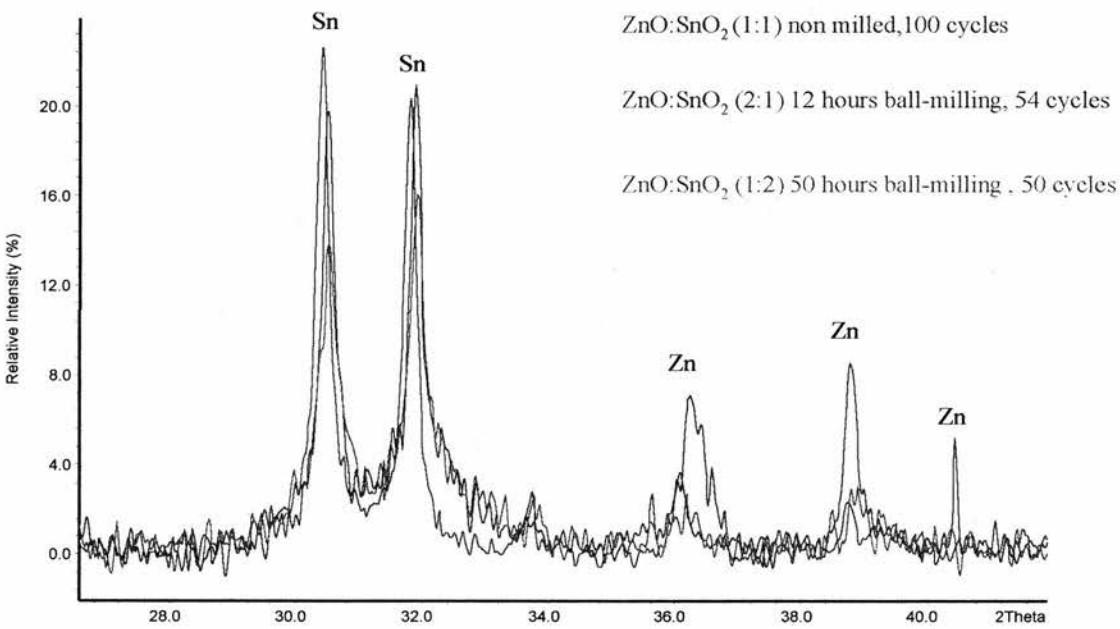

Figure 4.14: *Ex-situ* XRD collected on the $ZnO:SnO_2$ mixtures cycled between 0.2 and 0.8 V

4.3 Zn_2SnO_4, inverse spinel

4.3.1 EXAFS

4.3.1.a Introduction

In Zn_2SnO_4 material Zn^{2+} and Sn^{4+} are reduced simultaneously electrochemically in comparison to the mixtures $ZnO:SnO_2$. After the reduction of Zn_2SnO_4, Li is inserted irreversibly into Sn and Zn metal. EXAFS were performed on Zn_2SnO_4 on the Zn and Sn edges. The theoretical bond distances[21] described for Zn_2SnO_4 powder were used to fit the EXAFS data collected on Zn_2SnO_4 electrode. The theoretical Zn-Zn bond distances described for pure Zn metal[7] were used to fit Zn metal. The Zn-Zn bond distances for Li-Zn alloys were modelled using the Zn-Zn bond distances calculated for LiZn alloy in section 4.1[10]. The Sn-Sn bond distances for Sn metal were fitted using the theoretical bond distances of either alpha[18] Sn or beta[19] Sn. The Li-Sn alloy Sn-Sn bond distances were modelled using the Sn-Sn bond distances described for Li_2Sn_5[20].

4.3.1.b Zn EXAFS

The best fitting obtained for Zn_2SnO_4 during the initial discharge is shown Figure 4.15. The EXAFS data are shown on top of the figure and at the bottom the Fourier Transform (FT) of the EXAFS. The FT graph allows the visualisation of the different bond distances existing within the active material. Sn and Zn shells are observable when Zn_2SnO_4 has not been electrochemically tested, but when Zn_2SnO_4 is discharged until 0.4 V there are only an oxygen shell and a Zn shell. Finally Zn_2SnO_4

discharged down to 0.01 V exhibits only one Zn shell. The bond distances and coordination numbers fitted for Zn_2SnO_4 during discharge and charge are summarised in Table 4.5.

The spinel structure is more complex than showed in Table 4.5. The real bond distances and coordination number in the spinel structure is shown Table 4.6. In the Zn_2SnO_4 structure, two Zn atoms scatter when EXAFS is performed on Zn edge, thus an average of the coordination number was calculated as seen in Table 4.5. All the shells present until 4 Å in the Zn_2SnO_4 electrode were fitted but only the first three are shown in Table 4.5.

The bond distances found in the Zn_2SnO_4 electrode before testing match well the crystallographic bond distances for Zn_2SnO_4 powder. The Zn-Zn bond distance of the Zn_2SnO_4 electrode is smaller than the Zn-Sn bond distance while according to the crystal structure they should be identical (Table 4.6). The fitted Zn-O bond distance is larger than the crystallographic in the literature, but the fitted coordination numbers are identical to the theory. These differences are in accord with the fact that the crystallographic differences are an average over both Sn and Zn whereas the EXAFS data actually measure the short-range bond distances for Zn. At 0.4 V during the initial discharge 90 % of Zn_2SnO_4 and 10 % of Zn metal phase are simultaneously present. Only the Zn metal phases are observable when Zn_2SnO_4 is discharged down to 0.01 V and charged up to 0.4 V. The Zn-O bond distance at 0.4 V is smaller than the theoretical and the fitted bond distance of Zn_2SnO_4 while the number of oxygen atoms surrounding the Zn atom is identical. The Zn-Zn bond distances of the Zn metal

phase are similar during the initial discharge. On charge the Zn-Zn bond distance has decreased compared to the spinel discharged until 0.01 V. The coordination number of the Zn atom in the Zn metal phase decreases from 5.9 at the discharge (0.4 V) to 1.3 at the charge to (0.4 V).

At 0.4 V during the initial discharge the coordination number of Zn atom in the Zn metal phase is similar to the theoretical coordination number of Zn metal. However, the Zn-Zn bond distance is far from the bond distance existing in Zn metal. The coordination number of the Zn metal phase decreases during the initial discharge from 0.4 V to 0.01 V as expected, as the number of Li atom surrounding the Zn atom increases with Li insertion. During the initial charge (0.4V), surprisingly the coordination number has decreased compared to Zn_2SnO_4 discharged down to 0.01 V. It was expected to have an increase of the coordination number as less Li atoms surround the Zn atom with Li de-insertion.

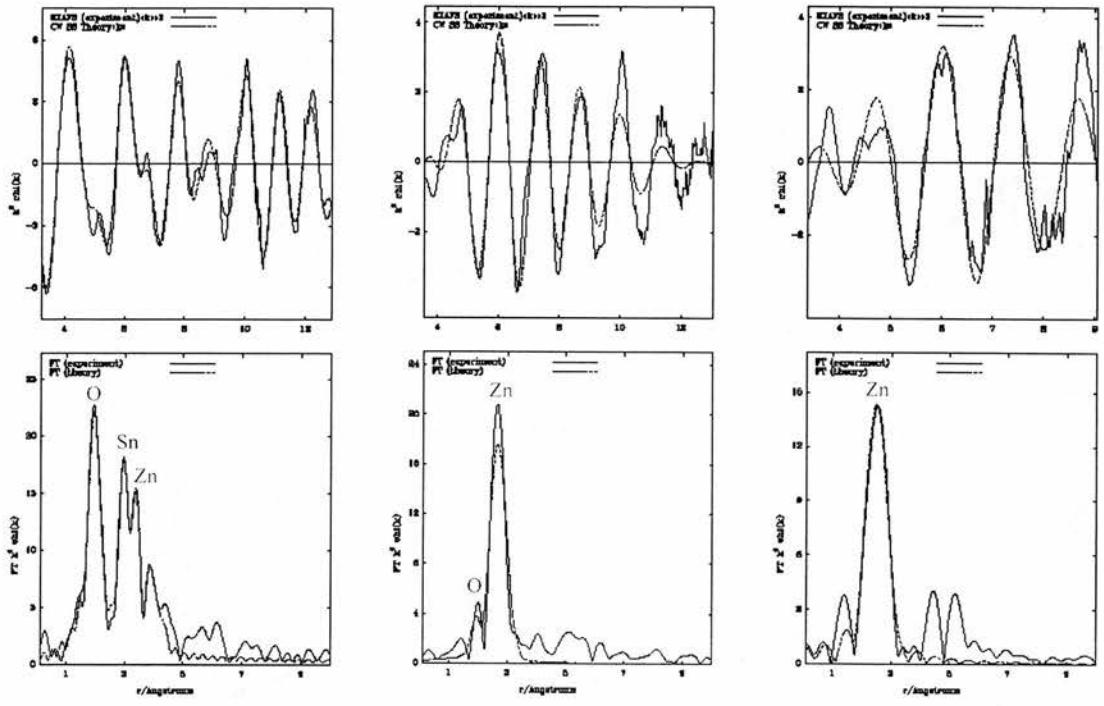

Zn_2SnO_4 electrode | 1st discharge down to 0.4 V | 1st discharge down to 0.01 V

Figure 4.15: *In-situ* Zn EXAFS collected on Zn_2SnO_4 during discharge

Potential position	% Phases (± 10 %)	Atom type	Coordination number ± 0.1	Distance ± 0.003 Å	R factor	Debye-Waller factor ± 0.001
Theoretical[21] Zn_2SnO_4	Zn_2SnO_4	O	3.0	2.041	-	-
		Zn	3.0	3.058	-	-
		Sn	3.0	3.058	-	-
Fitted Zn_2SnO_4 electrode	Zn_2SnO_4	O	3.0	2.099	21.51	0.046
		Zn	3.0	2.974		0.016
		Sn	3.0	3.227		0.014
Theoretical Zn metal[7]	Zn	Zn	6.0	2.665	-	-
LiZn[10]	LiZn	Zn	4.0	2.699	-	-
1st discharge down to 0.4 V (9 Li inserted)	10% Zn_2SnO_4 90% Zn	O	3.0	2.000	35.20	0.010
		Zn	5.9	2.634		0.032
1st discharge down to 0.01 V	100 % Zn	Zn	2.1	2.633	30.69	0.017
1st charge up to 0.4 V	100 % Zn	Zn	1.3	2.622	49.42	0.012

Table 4.5: *In-situ* EXAFS on the Zn edge collected on Zn_2SnO_4 during initial discharge and charge

	Atom type	Coordination number	Distances
Octahedral site	Zn	0	0
	O	6	2.041
	Sn	6	3.058
	Zn	6	3.058
	Sn	12	3.586
	O	6	3.826
Tetrahedral site	Zn	0	0
	O	4	2.098
	Sn	12	3.586
	Zn	12	3.586
	O	12	3.632

Table 4.6: Theoretical bond distances and coordination numbers of Zn_2SnO_4

4.3.1.c Sn EXAFS

Fitting the EXAFS data on Sn edge in Zn_2SnO_4 was more difficult compared to the Zn edge. Figure 4.16 shows the EXAFS of Zn_2SnO_4 electrode before testing, of Zn_2SnO_4 discharged down to 0.4 and 0.3 V. The fit obtained for Zn_2SnO_4 electrode before testing is very good but as soon Li are inserted the intensity of the EXAFS oscillations decrease gradually. When approximately 7 Li are inserted at 0.3 V the oscillations contain so many glitches that it is impossible to fit the data. When Zn_2SnO_4 is discharged further, a similar feature is seen from the data. The more Zn_2SnO_4 is reduced the more the EXAFS data collected on Sn edge becomes unanalysable. Thus instead the absorption near the Sn edge of Zn_2SnO_4 collected during discharge and charge was examined in order to study the mechanism.

The normalised intensity of the absorption is plotted vs. the Sn edge absorption Figure 4.17 and Figure 4.18. The absorption plots presented in Figure 4.17 were collected on the same battery during discharge, as for the plots show Figure 4.18.

The shape of the absorption changes during discharge (Figure 4.17). The plot in dark blue corresponding to the Zn_2SnO_4 electrode has a characteristic peak between 29210 and 29260 eV. The intensity of this characteristic peak decreases gradually with the reduction of Zn_2SnO_4. At 0.3 V the characteristic peak of Zn_2SnO_4 has disappeared, then from 0.3 until 0.02 V a small peak with a different shape appear. This latter peak located between 29220 and 29250 eV is situated above the graph corresponding to the discharge down to 0.3 V. In Figure 4.18 are plotted the Sn absorption collected during

discharge and charge. The same characteristic peak observed Figure 4.17 between 29210 and 29260 eV is observable in Figure 4.18. The plot of the Zn_2SnO_4 electrode and the plot of Zn_2SnO_4 discharged until 0.7 V are similar. The characteristic peak has almost disappeared when Zn_2SnO_4 is discharged until 0.4 V. On charge the characteristic peak of the Zn_2SnO_4 electrode has completely disappeared, and the absorption plots are overlapping for Zn_2SnO_4 charged up to 0.7 V and 1.5 V in the region 29210-29260 eV.

The characteristic peak observed for Zn_2SnO_4 electrode in Figure 4.17 and Figure 4.18 before testing corresponds to the short-range Zn_2SnO_4 structure. This characteristic peak decreases gradually with discharge to disappear at 0.02 V. This means that the short-range order in Zn_2SnO_4 has been completely randomised. The characteristic peak of the Zn_2SnO_4 electrode and Zn_2SnO_4 discharged until 0.7 V, Figure 4.18 overlap because the reduction of Zn_2SnO_4 occurs approximately at 0.5 V and not before as shown in chapter 3. There is no feature of the characteristic peak of Zn_2SnO_4 electrode during charge up to 1.5 V, which means that the Zn_2SnO_4 is not reformed. The plots of Zn_2SnO_4 charged until 0.7 V and Zn_2SnO_4 charged up to 1.5 V overlap in the region 29210-29260 eV because above 0.7 V most of the Li has been de-inserted from Li-Sn alloys leading to Sn metal[22-23-24].

The region 29180-29210 eV of the absorption plots shown in Figure 4.18 was further examined Figure 4.19. The shape of all the plots in this region during discharge and charge are relatively similar, although it was expected to observe different shapes due to the change of oxidation of Sn atom. The curves shift gradually to the right during

discharge compared to the Zn_2SnO_4 electrode plot before testing. From the discharge at 0.01 V to the charge at 1.5 V the Sn absorption plot are overlapping. The shift of the Sn absorption plot from the Zn_2SnO_4 electrode to the Zn_2SnO_4 electrode discharged down to 0.01 V confirms the progressive reduction of Zn_2SnO_4 on Li insertion. On charge the position of the Sn absorption plots is similar to the Sn absorption plot observed at 0.01 V. Thus during charge the oxidation state of Sn remained unchanged.

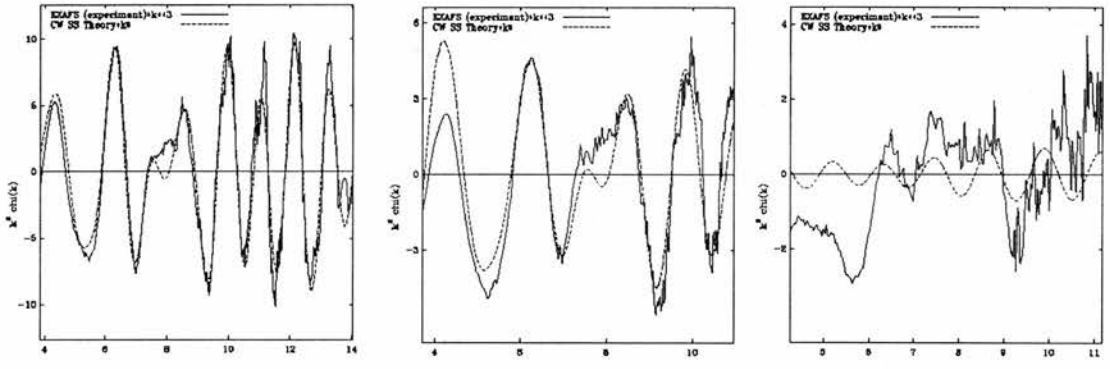

Figure 4.16: *In-situ* Sn EXAFS on Zn_2SnO_4 during discharge

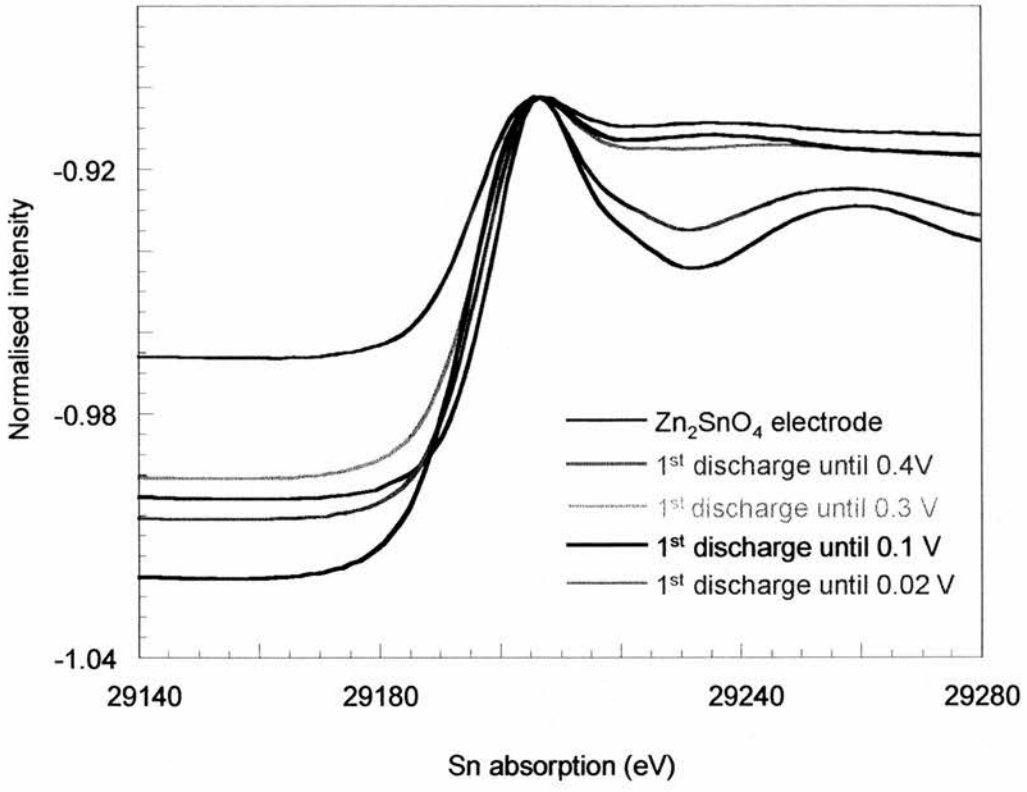

Figure 4.17: *In-situ* Sn edge absorption collected on Zn_2SnO_4 during initial discharge

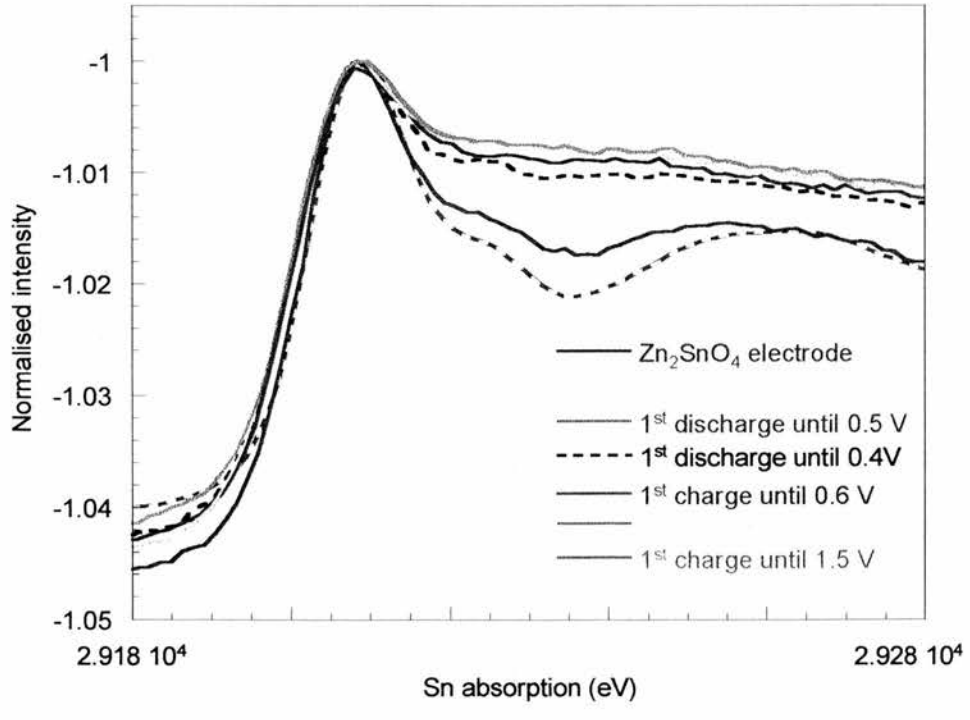

Figure 4.18: *In-situ* Sn edge absorption collected on Zn_2SnO_4 during initial discharge and charge

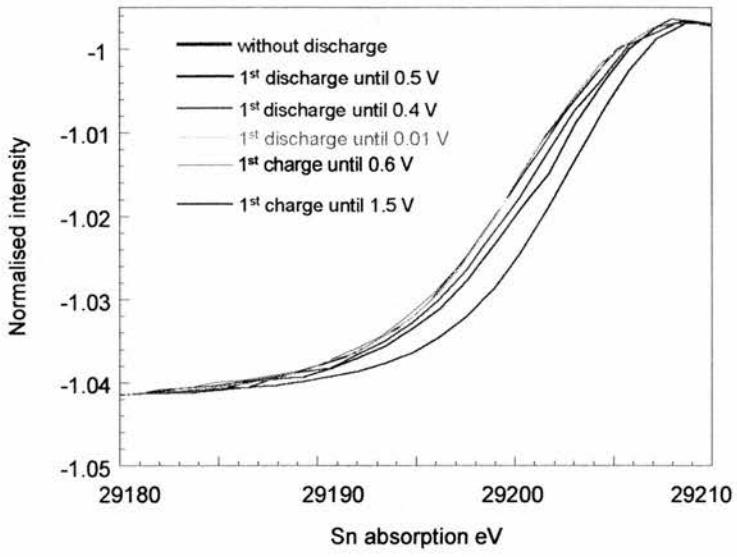

Figure 4.19: *In-situ* absorption near Sn edge collected on Zn_2SnO_4 during initial discharge and charge

4.3.1.d Comparison with ZnO:SnO_2 (2:1)

Zn_2SnO_4 and ZnO:SnO_2 (2:1) compounds have different electrochemical response towards Li. Sn^{4+} and Zn^{2+} are reduced simultaneously in Zn_2SnO_4 whereas in ZnO:SnO_2 (2:1) they are reduced successively. Thus the Sn absorption of Zn_2SnO_4 and ZnO:SnO_2 (2:1) were compared Figure 4.20. Both compounds have the same characteristic peak around 29210 and 29260 eV that corresponds to the Zn_2SnO_4 and SnO_2 structure. During the initial discharge below 0.3 V, Zn_2SnO_4 and ZnO:SnO_2 (2:1) plot show similar features in the region 29210-29260 eV. So the reduction of Zn_2SnO_4 and SnO_2 in the mixture ZnO:SnO_2 (2:1) leads to Sn metal. Below 0.3 V, the Sn absorption plot for the ZnO:SnO_2 (2:1) mixture exhibits two small peaks above 29220 eV whereas the Zn_2SnO_4 absorption plot in this region is completely flat. This indicates probably that the Sn metal formed from Zn_2SnO_4 is more disordered than the ZnO:SnO_2 (2:1) mixture.

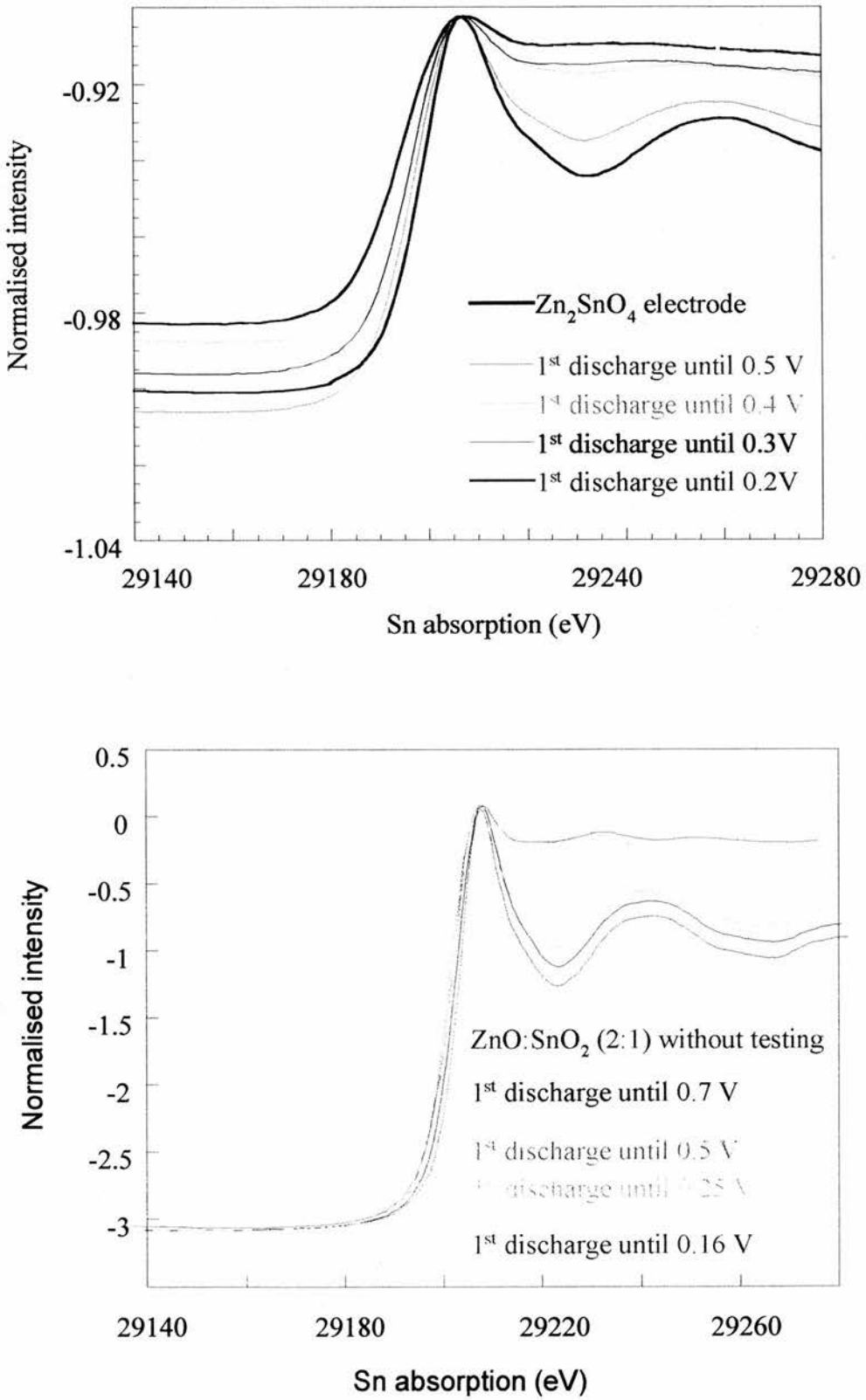

Figure 4.20: *In*-situ Sn edge absorption collected on Zn_2SnO_4 and ZnO:SnO_2 (2:1)

4.3.1.e Conclusion

In-situ EXAFS performed on Zn edge confirms the reduction of Zn_2SnO_4 into Zn metal and the reversible insertion of Li into Zn metal. But in-situ EXAFS performed on Sn edge show that no information can be extracted from the data as soon most of Zn_2SnO_4 is reduced. Earlier in this chapter it was demonstrated that the reduction of ZnO leads to crystalline Zn metal. Therefore the high crystallinity of Zn metal allows the collection of satisfactory Zn EXAFS data on Zn_2SnO_4 and ZnO. Having no Sn EXAFS data on Zn_2SnO_4 implies the reduction of Zn_2SnO_4 leads to amorphous and disordered Sn. It is more useful then to examine the Sn absorption edge. The characteristic peak between 29210 and 29260 eV corresponds to the Zn_2SnO_4 structure. When this characteristic disappears, that means Zn_2SnO_4 has been reduced to Sn metal. After the complete discharge of Zn_2SnO_4 and until the charge up to 1.5 V, the shape of Sn the absorption edge between 29210 and 29260 eV remains unchanged, this implies that the Sn metal has not been re-oxidised. The study of the absorption near Sn edge does not however confirms the reversible alloying formation of Sn metal with Li.

4.3.2 XRD

4.3.2.a Results

Zn_2SnO_4 electrode was discharged down to 0.02 V and charged up to 2 V, and then XRD measurement was performed *ex-situ* at the end of the initial charge (Figure 4.22). The three main peaks corresponding to the Cu grid used as internal standard are

visible. Peaks corresponding to Zn_2SnO_4 spinel and two small peaks corresponding to Zn metal are observable. The residual peaks of Zn_2SnO_4 indicate that Zn_2SnO_4 was not completely reduced even though the battery was discharged until 0.02 V. The appearance of the weak peaks of Zn metal at the end of the initial charge confirms again its high crystallinity. In contrast there is no sign of Sn metal peaks.

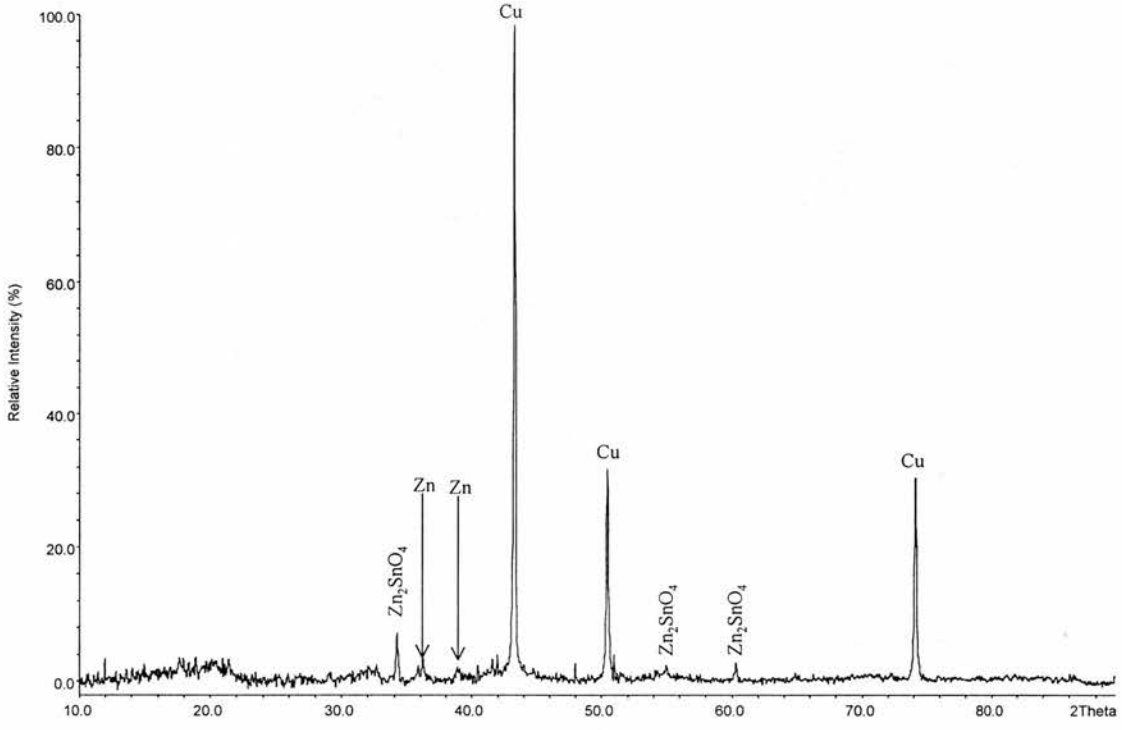

Figure 4.21: *Ex-situ* XRD collected on Zn_2SnO_4 at the end of the initial charge (0.02-2V)

Ex-situ XRD performed on Zn_2SnO_4 cycled 25 and 50 times between 0.2 and 1.5 V are compared to each other, Figure 4.22. Peaks corresponding to the internal standard (Cu grid) and to Zn_2SnO_4 are visible. Sn and Zn metals peaks are as well observable. Zn_2SnO_4 was not completely reduced even the entire reduction should have occurred at the end of the large reduction plateau located electrochemically at about 0.5 V. Zn

metal peaks are observable for both electrodes cycled 25 and 50 times. But Sn metal peaks are only observable for Zn_2SnO_4 cycled 50 times. Thus Sn metal remains amorphous until the 25th cycle and becomes crystalline by the 50th cycle. These observations match with the initial capacity lost (see chapter 3). At the 25th cycle Zn_2SnO_4 has lost nearly 60 % of its initial reversible capacity while at the 50th less than 25% of the initial reversible capacity remains.

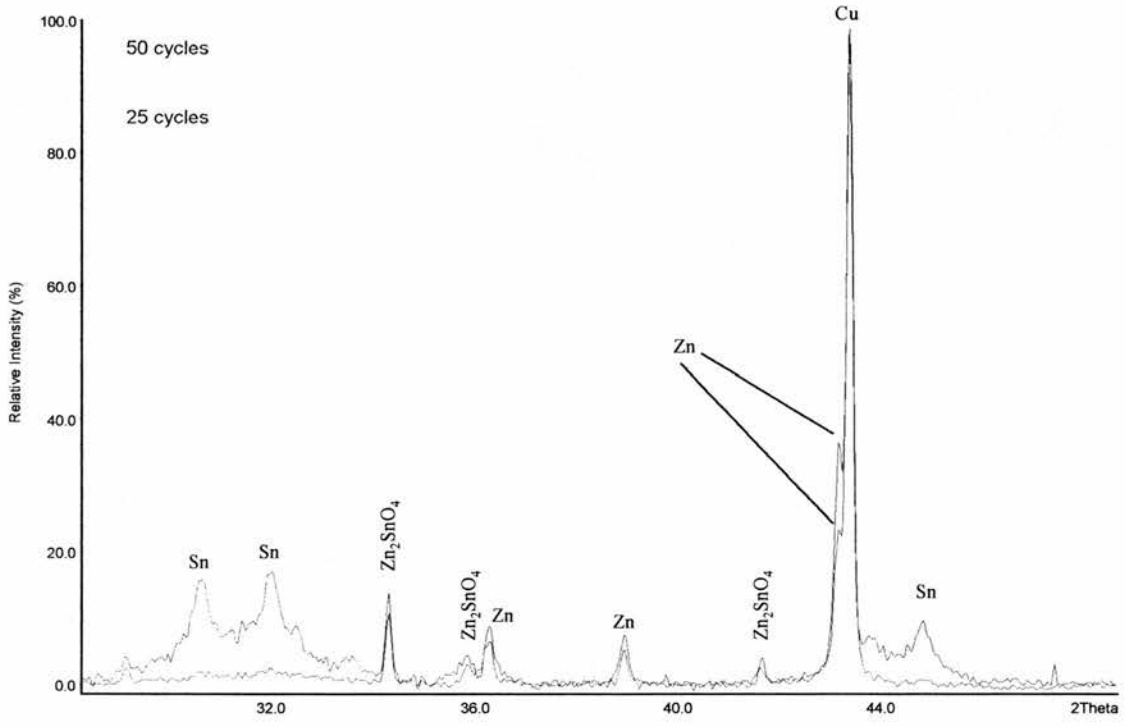

Figure 4.22: *Ex-situ* XRD collected on Zn_2SnO_4 at the end of the charge when cycled between 0.2 and 1.5 V

XRD patterns were collected *ex-situ* on Zn_2SnO_4 cycled between 0.2 and 1.5 V, and Zn_2SnO_4 cycled between 0.2 and 0.8 V. These two XRD patterns are compared with each other Figure 4.23. The residual peak of Zn_2SnO_4 and the Cu grid peak used as an internal standard are present for both Zn_2SnO_4 electrodes. Sn metal and Zn metal

peaks are observable but only for Zn_2SnO_4 cycled 50 times between 0.2 and 1.5 V, although Zn_2SnO_4 cycled between 0.2 and 0.8 V was cycled twice as long. Despite the high crystallinity of Zn metal seen in the previous sections of this chapter, when the range of cycling voltage is well chosen, Zn metal remains amorphous until the 100th cycle. This implies that the crystallinity of Zn metal depends on the starting material. ZnO gives high crystalline Zn metal whatever the window voltage chosen. However the spinel does not give crystalline Zn metal at the end of the 1st cycle if the spinel is cycled between the appropriate window voltage. Within the range of voltage 0.2-0.8 V, Sn metal stays amorphous until the 100th cycle. This result explains why in chapter 3 the best capacity retention is given by Zn_2SnO_4 cycled between 0.2 and 0.8 V.

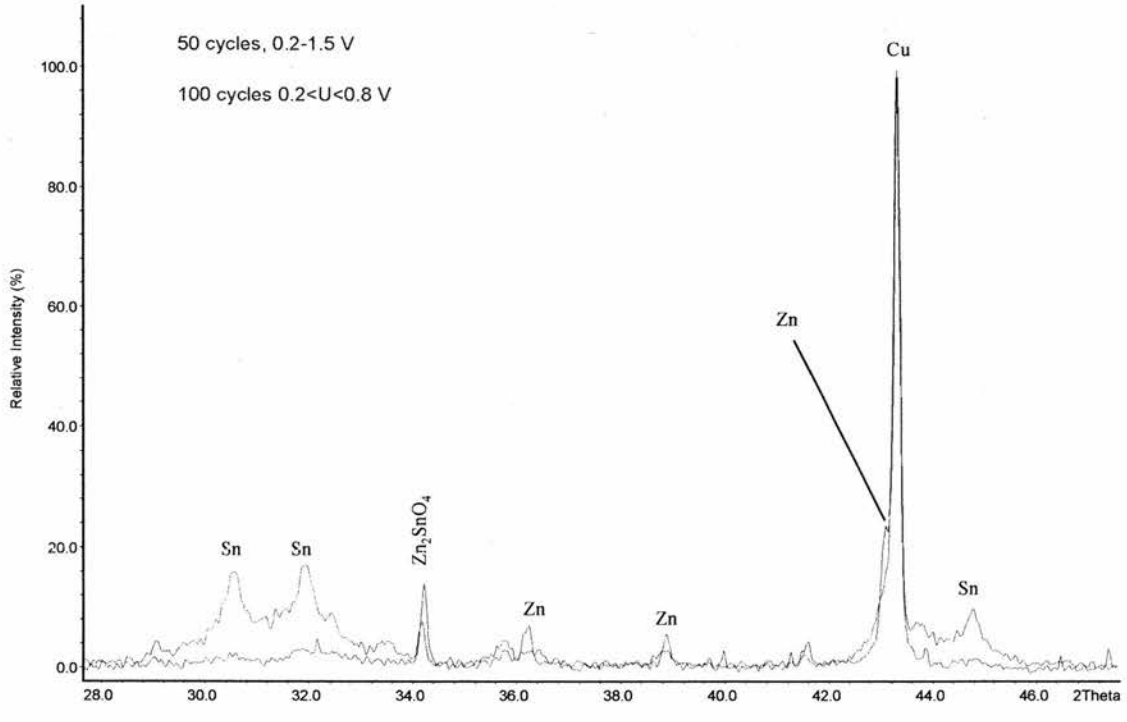

Figure 4.23: *Ex-situ* XRD collected on Zn_2SnO_4 at the end of the charge

4.3.2.b Comparison with $ZnO:SnO_2$ (2:1)

The XRD patterns of Zn_2SnO_4 and $ZnO:SnO_2$ (2:1) cycled between 0.2 and 0.8 V with a current of 0.1 mA were compared Figure 4.24. In the graph peaks corresponding to Cu, Zn metal, Sn metal and Zn_2SnO_4 are observable. The Sn and Zn metals peaks are only present for $ZnO:SnO_2$ (2:1) which was cycled less than Zn_2SnO_4. Within this voltage cycling range Zn_2SnO_4 leads to amorphous Sn and Zn metal whereas $ZnO:SnO_2$ (2:1) leads to crystalline Sn and Zn metals. This implies that the crystallinity of Zn and Sn metals depend on the starting material. These observations correlate with the electrochemical conclusions made in chapter 3. Although both compounds have similar ZnO and SnO_2 content, $ZnO:SnO_2$ (2:1) has poor cycling performance compared to Zn_2SnO_4. Therefore the poor electrochemical performance of $ZnO:SnO_2$ (2:1) is due to the high crystallinity of Sn and Zn metals obtained after the reduction of SnO_2 and ZnO.

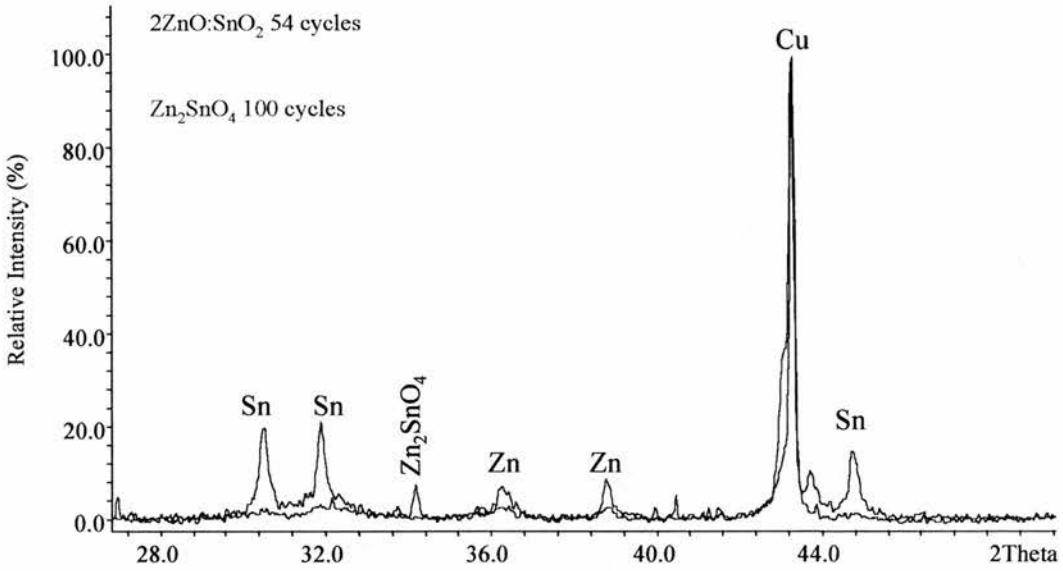

Figure 4.24: *Ex-situ* XRD collected at the end of charge on Zn_2SnO_4 and $ZnO:SnO_2$ (2:1) cycled between 0.2 and 0.8 V

4.3.2.c Conclusion

Ex-situ XRD performed on Zn_2SnO_4 shows that even if the battery is completely discharged, there is some residual spinel. The presence of Sn and Zn metal peaks proves the reduction of Zn_2SnO_4 into Sn metal and Zn metal. The crystallinity observed when reducing ZnO is also observed when reducing Zn_2SnO_4. However Zn crystallinity can be controlled if the voltage cycling range is well chosen. Sn metal is amorphous after the initial discharge but eventually becomes crystalline after several cycles. But Sn metal remains amorphous upon cycling like Zn metal if the cycling range of voltage is well chosen. In chapter 3 it was demonstrated that the best cycling performance is obtained when Zn_2SnO_4 is cycled between 0.2 and 0.8 V. This is because Zn metal and Sn metal are still amorphous at the 100^{th} cycle. Thus the crystallinity of the metals control the cycling performance of Zn_2SnO_4.

4.4 Li_2SnO_3 XRD

4.4.1 Results

The *ex-situ* XRD performed on Li_2SnO_3 cycled 4 times between 0.1 and 2 V is shown Figure 4.25. Cu grid, Sn metal and Li_2SnO_3 peaks are observable. The small peaks of Li_2SnO_3 prove that Li_2SnO_3 was not completely reduced. That was expected as the plateau of reduction of Li_2SnO_3 is around 0.18 V. The reduction of Li_2SnO_3 into Sn metal is confirmed by the presence of Sn metal peaks. These latter peaks are well crystallised after only 4 cycles. Other *ex-situ* XRD carried out on Li_2SnO_3 cycled within a different voltage window also shows well crystallised Sn metal. Electrochemical tests have shown that Li_2SnO_3 is not a promising anode material for Li-ion battery because of the high crystallinity of Sn metal obtained after the Li_2SnO_3 reduction.

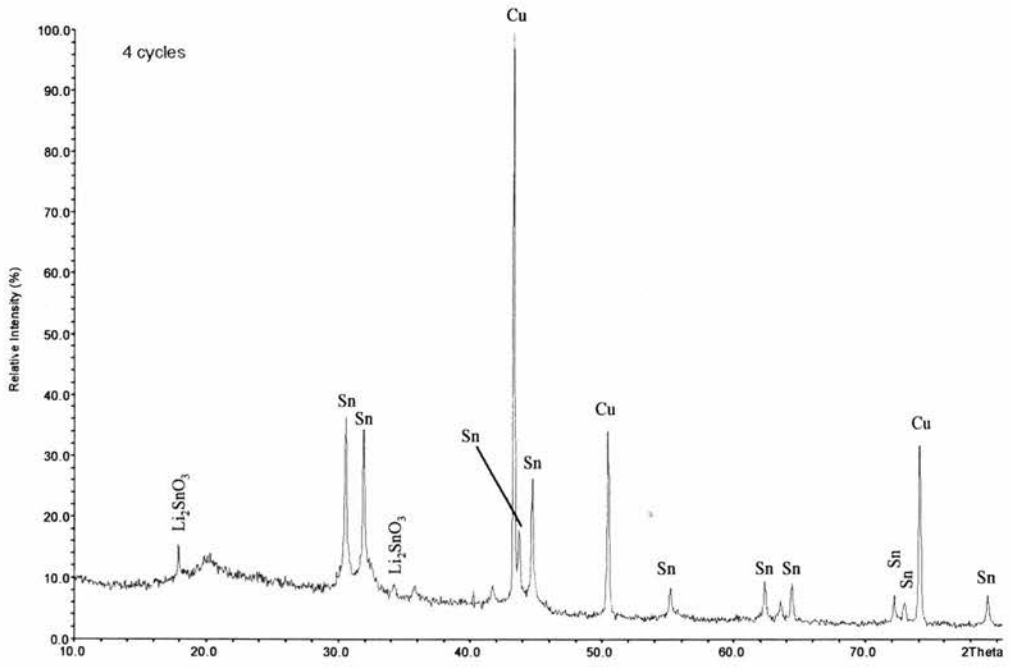

Figure 4.25: *Ex-situ* XRD collected on Li_2SnO_3 at the end of charge when cycled between 0.1 and 2 V

4.4.2 Comparison with SnO_2

In chapter 3 it was shown that SnO_2 exhibits better cycling performance than Li_2SnO_3. Li_2O is believed to absorb the volume changes occurring during the reversible alloying formation of Li-Sn alloys. An improvement of the electrochemical performance of Li_2SnO_3 was expected, as Li_2SnO_3 reduction leads to 3 moles of Li_2O and SnO_2 to 2 moles. *Ex-situ* XRD of Li_2SnO_3 cycled between 0.02 and 0.8 V were compared to the XRD of SnO_2 cycled between 0.2 and 0.8 V, Figure 4.26. Cu peaks corresponding to the internal standard is observable as well as Sn and SnO_2 peaks. The residual peak of SnO_2 means that the reduction was not complete. The peak intensity of Sn metal is identical for both oxides although Li_2SnO_3 was cycled twice as long. This implies that the extra mole of Li_2O present in Li_2SnO_3 electrode seems to restrain better the volume changes occurring during the reversible formation of Li-Sn alloys in comparison to SnO_2. The crystallinity of Sn metal is higher in the case of SnO_2. Therefore the bad cycling performance of Li_2SnO_3 compared to SnO_2 is not due to the crystallinity of Sn metal.

The poor electrochemical performance of Li_2SnO_3 is probably linked to its potential of reduction. Li_2SnO_3 is reduced around 0.18 V and simultaneously various Li-Sn alloys are formed. SnO_2 in the other hand is reduced around 0.95 V and then Li is inserted into Sn metal. The poor electrochemical performance can be caused by the discharge limit voltage, 0.02 V which is very close to Li electrochemical potential, therefore can cause Li electroplating.

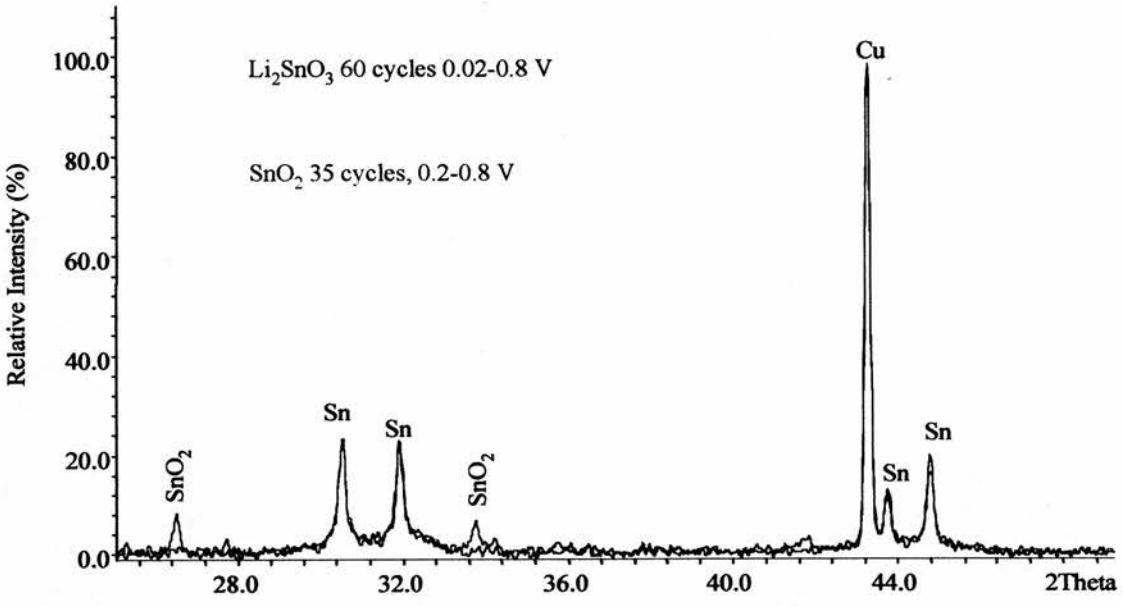

Figure 4.26: Comparison of ex-*situ* XRD of Li_2SnO_3 and SnO_2

4.5 References

1 I. A. Courtney and J. R. Dahn, J. Electrochem. Soc. 144 (6), 2045, (1997)

2 A. N. Dey, J. Electrochem. Soc. 118, 1547 (1971)

3 J. Wang, P. King and R. A. Huggins, Solid State Ionic 20, 185 (1986)

4 Z. Shi, M. Liu, J. L. Gole, Electrochem. Solid State Lett. 3, 312 (2000)

5 T. Fujieda, S. Takahashi, S. Higuchi, J. Power Sources 40, 283 (1992)

6 J. Albertsson, S. C. Abrahams, A. Kvick, Acta Cryst. B 39, 34 (1989)

7 H. E. Swanson, E. Tatge, Annalen der Physik 5, 121 (1953)

8 E. Zintl,G. Brauer, Z. Phys. Chem. 20, 252 (1933)

9 Komovsky, Maximow, Z. kristallogr. 92, 282 (1935)

10 K. Kuriyama, N. Masaki, Acta Crystallogr. B 31, 1793 (1975)

11 U. Muller, Inorganic Structural Chemistry, ed. Wiley

12 S. Grugeon, S. Laruelle, R. Herrera-Urbina, L. Dupont, P. Poizot, J. M. Tarascon J. Electrochem. Soc. 148, A285 (2001)

13 P. Poizot, S. Laruelle, S. Grugeon, L. Dupont, J-M. Tarascon, Nature 407, 496 (2000)

14 T. Brousse, I. Sandu, J. Santos-Pena, M. Danot, R. Retoux, D. M. Schleich, extended abstract 9, Lithium Battery Discussion Materials, May 27-June 1 (2001), France

15 J. Wang, I. D. Raistrick, R. A. Huggins, J. Electrochem. Soc. 133, 457 (1986)

16 J. Wang, P. King and R. A. Huggins, Solid State Ionics 20, 185 (1986)

17 H. Seki, N. Ishizawa, N. Mizutani, M. Kato, J. Ceramic Assoc. Japan 92, 297 (1984)

18 J. A. Lee, G. V. Raynor, Nature 174, 1011 (1954)

19 V. T. Deshpande, D. B. Sirdeshmukh, Acta Crystallographica 15, 294 (1962)

20 D. A. Hansen, L. J. Chang, Acta Crystallographica B, 25, 2392 (1969)

21 J. Choisnet, A. Deschanvres, B. Raveau, Comptes Rendus Hebdomadaires des Seances de l'Academie des Sciences, Serie C, Sciences Chimiques 266, 543(1968)

22 J. Wang, I. D. Raistrick, R. A. Huggins, J. Electrochem. Soc. 133, 457 (1986)

23 R. A. Huggins, Solid State Ionics 11-115, 57 (1998)

24 C. J. Wen, R. A. Huggins, J. Electrochem. Soc. 128, 1181 (1981)

5 Discussion

5.1 ZnO

Electrochemical tests showed that ZnO is reduced at 0.6 V into Zn metal, then Li inserts reversibly into Zn metal. On charging about 50 % of the initial capacity is lost due to the formation of Li_2O during the initial discharge. Two unidentified electrochemical phenomena were found during charge, this implies that ZnO does not follow a similar mechanism to that suggested for tin oxides as additional processes occur beyond reduction to metal and Li alloying with Zn.

EXAFS and XRD measurements confirmed that ZnO is reduced into Zn metal and then Li is inserted reversibly into Zn metal. On charge above 0.6 V, the re-oxidation of a small amount of Zn metal has been observed by EXAFS. The re-oxidation of Zn metal implies the partial destruction of Li_2O, which is believed to be formed irreversibly during the initial discharge. According to EXAFS the zinc oxide formed during charge has a different structure to the starting ZnO material. The re-oxidation of Zn metal was not observed by XRD implying the formation of either an amorphous phase or one with too small particles of zinc oxide. XRD performed on the ZnO electrode during the initial discharge reveals the high crystallinity of Zn metal. The high crystallinity of Zn metal is responsible for the poor electrochemical performance of ZnO whatever the cycling voltage range used. After 5 cycles the ZnO electrode has lost 20 % of its initial reversible capacity and at the 10^{th} cycle there is only 50 % of the reversible capacity left.

5.2 $ZnO:SnO_2$ mixtures

Despite its poor cyclability ZnO was mixed with SnO_2 using 3 molar ratios: 1:2, 1:1 and 2:1 to form the $ZnO:SnO_2$ mixtures. In addition both oxides were ball-milled to provide fine particles. Electrochemical studies demonstrated that SnO_2 and ZnO react independently towards Li insertion. SnO_2 is reduced first into Sn metal at 0.9 V, then ZnO into Zn metal at 0.6 V. Thereafter Li inserts reversibly Sn and Zn metals.

EXAFS combined with XRD verified the reduction of SnO_2 and ZnO into Sn and Zn metal respectively. The independent electrochemical behaviour of both oxides was confirmed by Sn and Zn EXAFS analysis. The re-oxidation of Zn metal was also observed by EXAFS for the $ZnO:SnO_2$ mixture. Sn EXAFS shows that the reduction of SnO_2 in the mixture leads to amorphous Sn metal implying that the amorphous Sn is disordered at short range.

Samples with high SnO_2 content display the best cycling performance while samples with high ZnO content have the worst electrochemical performance for the $ZnO:SnO_2$ mixture. The small particle size of ZnO and SnO_2 influence unevenly the electrochemical behaviour the $ZnO:SnO_2$ mixtures. The capacity retention of $ZnO:SnO_2$ (2:1) and $ZnO:SnO_2$ (1:2) improved with milling. The electrochemical performance of $ZnO:SnO_2$ (2:1) samples shows strong ball-milling dependence whereas the $ZnO:SnO_2$ (1:2) samples have little dependence. The improvement of the capacity retention for the $ZnO:SnO_2$ (2:1) samples is noticeable after only 12 hours ball-milling while the $ZnO:SnO_2$ (1:2) samples needs 40 hours ball-milling. The $ZnO:SnO_2$ (1:1) samples show no improvement of the capacity retention upon milling but the increase of the

capacity fade. XRD performed on the mixtures shows high crystalline Sn and Zn metals after several cycles. Thus the high crystallinity of the metals results in the poor cycling performance of the $ZnO:SnO_2$ mixtures.

5.3 Zn_2SnO_4

Zn_2SnO_4 has the same composition as the $ZnO:SnO_2$ (2:1) mixture but behaves very differently electrochemically towards Li. On Li insertion Zn^{2+} and Sn^{4+} are reduced simultaneously in the Zn_2SnO_4 material while in the $ZnO:SnO_2$ (2:1) mixture each cation is reduced successively. The reduction potential of Zn_2SnO_4 occurs at 0.5 V, this potential is much lower to that of SnO_2 (0.9 V) and close to ZnO (0.6 V) although slightly lower. An electrochemical reaction that occurs at 1.23 V during charge has not been identified. Therefore Zn_2SnO_4 follows partially the suggested model for tin-based oxides.

EXAFS has proved that Zn_2SnO_4 is reduced into Zn and Sn metal, and then these form reversibly Li-Zn and Li-Sn alloys respectively. EXAFS performed during the initial cycle shows that Zn_2SnO_4 leads to amorphous Sn metal and crystalline Zn metal, this was verified by XRD. Although the x-rays studies reveal the crystallinity of Zn metal, when the cycling voltage range is well chosen the crystallinity of Zn metal can be controlled. Consequently Zn_2SnO_4 displays an excellent cycling performance compared to the $ZnO:SnO_2$ (2:1) mixture. Zn_2SnO_4 was synthesised at 1100 °C and 1000 °C; Zn_2SnO_4 (1000 °C) has smaller particle size than Zn_2SnO_4 (1100 °C). Zn_2SnO_4 (1000 °C) exhibits better cycling performance than Zn_2SnO_4 (1100 °C) which correlate with

the particle size. Small particle size is less sensitive to the volume changes occurring during the reversible Li alloying with Zn and Sn metals.

5.4 Li_2SnO_3

Li_2SnO_3 is reduced at 0.18 V into metallic Sn, then various Li-Sn alloys are reversibly formed. The reduction of Li_2SnO_3 and the reversible Li insertion into Sn metal occurs simultaneously. This reduction potential is very close to Li potential. Li_2SnO_3 does not follow as well the proposed mechanism for tin oxides as two electrochemical reactions could not be identified.

Li_2SnO_3 prepared at 650 °C and 1000 °C display relatively close and fast capacity fade although Li_2SnO_3 (650 °C) has smaller particle size. In this case fine particles do not improve significantly the cyclability. Li_2SnO_3 forms during the initial discharge one extra mole of Li_2O compared to SnO_2. Li_2O is thought to minimise the volume expansion occurring during the reversible formation of Li-Sn alloys, therefore Li_2SnO_3 should exhibit better electrochemical performance, as both tin oxides theoretically have equal capacities. Although Sn metal from SnO_2 is more crystalline than Sn metal from Li_2SnO_3, SnO_2 still has better cycling performance compared to Li_2SnO_3. The excess of matrix is not sufficient to improve the performance. The poor electrochemical performance is probably due to the fact that the reduction potential is too close to Li metal.

5.5 Conclusion

For all the materials investigated it has been shown that cycling above 0.8 V and below 0.2 V decreases the electrochemical performance of the electrode. Above 0.8 V it has been revealed the evidence of an additional electrochemical process on charge. This process occurs at potentials just above 1 V and is responsible for the degradation of the electrode. The electrochemical performance of the oxides investigated is lower when the electrode is discharged below 0.2 V. This is because the discharge is too close to Li metal and presumably causes Li electroplating. Thus the optimal cycling window range is 0.2-0.8 V for all the oxides except for Li_2SnO_3 that has a reduction potential around 0.18 V.

The influence of small particle size on the cycling performance depends on the materials. In the ZnO:SnO_2 mixtures the capacity retention has improved for the ratio 2:1 and 1:2, and not for the ratio 1:1. Li_2SnO_3 (650 °C) contains smaller particles than Li_2SnO_3 (1000 °C), however it does not exhibit significant improvement. In contrast Zn_2SnO_4 (1000 °C), which has smaller particle displays better electrochemical performance than Zn_2SnO_4 (1100 °C) that has large particle.

Amongst all the materials studied, Zn_2SnO_4 is the most promising negative electrodes for Li-ion batteries. It exhibits better electrochemical behaviour than SnO_2. That is surprising, as Zn_2SnO_4 contains ZnO, which has shown poor cyclability due the high tendency of crystalline Zn metal to form. Thus the electrochemical performance depends on the atomic arrangement of the starting material. To check the excellent

electrochemical behaviour of Zn_2SnO_4 it would be interesting to test it against a commercial positive electrode such as $LiCoO_2$.